Delft University of Technology

Master Thesis

Design of a reversible growth-from-the-tip device following a complex trajectory

Author: Michiel Doelman
Student number: 4374371

Master of Science
Mechanical Engineering
Track: Biomechanical Design
December 22, 2020

Supervisors: Dr.ir. A. Sakes, ir. F. Trauzettel and Prof.dr.ir. P. Breedveld

Preface

Within my TU Delft career, growth principles of plant roots keep floating to the surface. At the course *Bio Inspired Design* we raised the question: 'Why are all building piles put straight into the soil, while plant roots, which curl and grow perpendicular roots, are master anchorers?'. During my literature study, I dived deeper in all related growth principles of plant roots underground and I discovered the outstanding performance of plant roots in terms of following a complex path with a small diameter. This final work aims to incorporate the relevant working principles into a working device, that can do what plant roots do best; position themselves into any hard-to-reach location.

For me, this biological and technological convention of interests has more often been an historic event. For example, during my time in primary school my leisure time was mostly spend on small technical projects or building dams, huts and seawalls. Moreover, my favorite secondary school courses have always been technological or biological related, especially the course *Nature, Life, Technology*. And still, I'm interested in a wide variety of biological and technical systems, processes and objects.

During this whole project, the Corona virus had its effect on society. I prefer not to complain, because no terrible things have yet occurred to me or close friends and family. However, healthy distraction or small talks with colleagues were hard to find. Despite a relatively lone period, my girlfriend, family and friends luckily helped me through.

Delft, December 2020

Michiel Doelman

Abstract

Background: *Accessing targets through complex trajectories with multiple curves in series, remains challenging today in many application fields, like surgery, the Fukushima disaster, maintenance of complex tube networks, mining and space operations. Current steerable devices require control of an extensive amount of segments, while moving as a whole through the environment. In contrast, growth-from-the-tip devices move only at the tip by creating a solidified support structure, allowing for active curvature creation at any point of the trajectory with limited effect on the environment. However, reversible and accurate growth remain challenging for these type of devices.*

Method: *Competitive design requirements are setup and quantified. Subsequently, a broad concept generation is performed, based on the ACRREX (i.e. Abstracting, Categorizing, Reflecting, Reformulating and Extending) method. After selection of one working principle, a proof-of-principle is designed, prototyped and evaluated. Based on the outcome, a second prototype is created and evaluated again. Evaluation of both prototypes comprise accuracy measurements, based on the ratio of path deviation from a kinematic model and insertion length. Moreover, load bearing capacity of the support structure, forces acting on the environment and overall performance are assessed.*

Results: *The selected concept is based on everting chains, driven by torque at the tip and consisting of two chains with lockable sliding hinged joints. Both prototypes successfully show reversible and steerable growth-from-the-tip, by the fact that counter rotation of the tip gears resulted in a translation of the tip, while differential rotation of the gears resulted in curvature creation. Prototype I (PI) had an accuracy of 4.5% for pure translations and 6.2% to 8.1% for the formation of two sequential (90 degrees) curvatures. Prototype II (PII), which was not fully operational, had a deviation per insertion length of 2.9% for a single curvature and to 10.7% to 19.1% for a combination of translations and curvatures in series.*

Even though the shape-locks of Prototype I had 3 degrees play per joint and a limiting amount of locking positions, the average orthogonal load bearing capacity was high (49N) with an accompanied deformation of maximally 8 degrees. In contrast, the friction-locked drum brakes of Prototype II rotated up to 70 degrees, by both deformation (22%) and slippage (78%) at a load of 20N. A rotation of 25 degrees was reached at an average load of 7.3N. Normal forces acting on the environment during movement were only measured for Prototype I, resulting in direct distortions (78%) of <4N and indirect distortions (22%) of <0.36N. Moreover, both prototypes had comparable elongation rates (PI: 92.9mm/min, PII: 156mm/min), extension rates (PI: 2.6mm/mm, PII: 0.9mm/mm) and widths (PI: 268mm, PII: 270mm). Lastly, a minimal inner curvature of zero and a minimal outer curvature equal to the device's width were realized, due to the presence of sliding hinged joints.

Conclusion and discussion: *Both prototypes performed reversible growth-from-the-tip based on the everting chains principle. Accordingly, the generated kinematic model that links gear rotations to tip rotations and translations seems to be an accurate simplification of the experimental data. In addition, the normal forces acting on the environment were much lower than the load bearing capacity of Prototype I, confirming sufficient support and limited deflection and deformation by the built structure. The everting chain principle has many advantages. First, multiple curves in series can be formed in a reversible manner. Moreover, high load bearing capacity of locked chains results in high accuracy of the system's movement. Furthermore, the system has limited interaction with the environment and no additional system is required to create curvature. Lastly, sliding hinged joints allow for movement along sharp edges. The next generation of everting chain robots should incorporate improved power and load tuning, size reduction and chains that allow for fully self-supporting movements in 3D space.*

Contents

1 Introduction

1.1 Background

1.1.1 Complex trajectories

Despite many high-tech developments in the last decades, physical access of a mechanical device to a certain target remains challenging today. A clear example of the need for such devices comes from the disaster of the Fukushima Daiichi Nuclear power plant. In 2011 three of the six reactors melted down and even now the melted fuel still needs to be cleaned up. In accordance with the Japanese government, it would take 30 to 40 years, tens of billions of dollars and fundamentally different type of robots to access and clean up the melted fuel [1]. The task of gaining access to the fuel is complicated by the exceptionally high radiation levels. Moreover, the space around the target is dark and covered by lots of debris from pipes, machinery and robots that got stuck in earlier missions [1].

Another example of challenging accessibility of a target can be found in Minimally Invasive Surgery (MIS). The human body namely is a complex network of nerves and vessels with many vulnerable obstacles [2]. Accordingly, many surgical targets like the skull base involve small workspaces restricted by critical and difficult-to-visualize structures [3]. Conventional operations comprise open surgery, with considerable quantities of scar tissue, high risk of infection and long recovery time [4, 5, 6]. Therefore, MIS is aimed to reduce surgical invasiveness, morbidity, mortality rate, recovery time and pain experienced by the patient [3, 7, 8]. One of the most common MIS technique is called key-hole surgery (*e.g.* laparoscopy), involving extraluminal (*i.e.* outside hollow organs) workspaces and percutaneous access into the body, most often by long, straight and rigid devices [9, 10, 11], as can be seen in Figure 1.1. In contrast, devices designed for an intraluminal workspace follow natural anatomical pathways entering at natural openings (*e.g.* mouth, nose or anus) to approach the surgical target [11, 5, 9]. Transluminal operations in turn, involve a controlled breach of a luminal barrier, resulting in an intraluminal and extraluminal workspace accessed through natural orifices. Finally, hybrid systems access targets via a combination of the abovementioned routes.

Obviously, a surgical target can be approached via different routes. However, current devices use tissue to passively steer, involving damage and pain for the patient. Devices that actively steer cannot follow all complex paths, as will be treated in the next section. Therefore, an innovative surgical device which is able to follow more complex trajectories, will increase access options, which on its turn serves MIS and thereby the patients' health. In conclusion, a device that can actively bend along more curves in series with respect to current devices, can pursue trajectories of increased complexity.

Other proposed fields of application related to hard-to-reach-targets are complex tube or tunnel networks, earthquake-related save and rescue missions, particular space operations or mining.

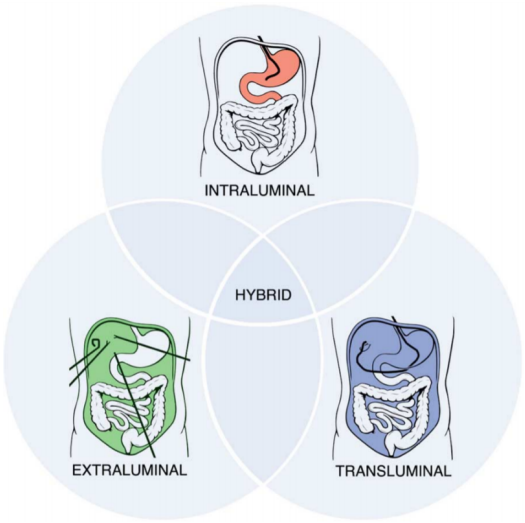

Figure 1.1: **Categorization of Minimally Invasive Surgical (MIS) operations according to the type of body-access, comprising extraluminal, intraluminal and transluminal operations. The reachable workspaces are indicated in green, red and blue. (Figure adapted from Vitiello [10])**

1.1.2 Steerable devices

Multiple attempts have been made to design a mechanical device able to actively move around obstacles, especially within the field of minimally invasive surgery. For example Degani *et al.* [12] created a device able to curve in a three-dimensional space with only six actuators, being both rigid and flexible. Moreover, Ali *et al.* developed a mechanical catheter with multiple steering actions. An overview of potential steering actions is given in Figure 1.2, with 1 Degree Of Freedom (DOF) (Figure 1.2 (a)), 2 DOFs (Figure 1.2 (b)) and 4 DOFs (Figure 1.2 (c)).

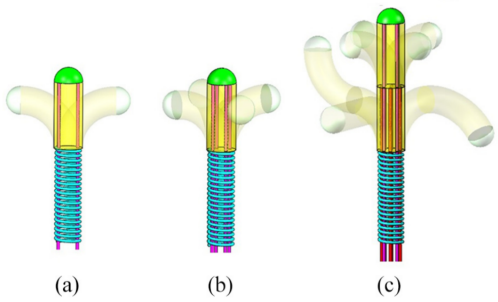

Figure 1.2: **Overview of potential steering actions of surgical catheter, with (a) 1 DOF (b) 2 DOFs and (c) 4 DOFs. (Figure adapted from Ali [13])**

With respect to the type of control, segments can be controlled independently, dependently, via a Follow-The-Leader (FTL) method, or via a master-slave method [9, 7]. At FTL, only the steering action of the front segment is actively controlled, while the other segments passively follow the tip segment [7]. The BioInspired Technology (BITE)-group at TU Delft created such a FTL device, called MemoFlex [2]. The device has 28 DOFs and a small diameter of 5mm. Moreover, Ota *et al.* [14] designed CardioARM (also known as HARP), a FTL device of 300mm in length and diameter of 10mm, with 50 cylindrical links able to move +/− 10 degrees with respect to each-other, resulting in 105 DOFs.

It is worth noting that most of these devices are hyper-redundant, referred as the excessive amount of DOFs with respect to the performed movement of the end-effector [2].

Another interesting surgical device was developed by Dupont *et al.* [15], called Concentric Tube Robots. By the insertion of precurved elastic tubes inside each other, the total system curves towards an energetic stability with minimal potential energy. By an independent control of rotation and translation of each tube, multiple curves and forward movement can be realized, as visualized in Figure 1.3. Apart from many advantages like having a small cross-section of the device, the system is found to be highly sensitive to small loads in certain configurations [15].

It should be noted that the aforementioned steerable devices require complex designs and high control effort. Since steerable devices can only steer, forward motion is induced from the base.

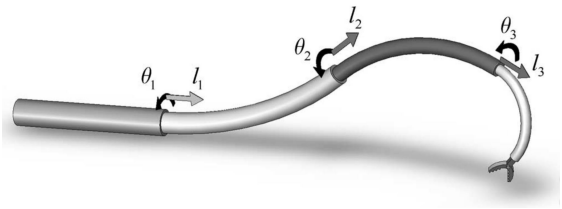

Figure 1.3: **Concentric tube design. Figure adapted from Dupont *et al.* [15]).**

Consequently, segments need to be controlled over the whole length of the device, when moving around an obstacle. As a result, the amount of internal DOFs, the length and the type of control of the device determine the maximum complexity of trajectories that can be followed. In contrast, growth-from-the-tip involves a tip that is pushed forward on top of a solidified support structure. Therefore, growth-from-the-tip does not require an external forward drive and many steerable segments. This comparison is visualized in Figure 1.4.

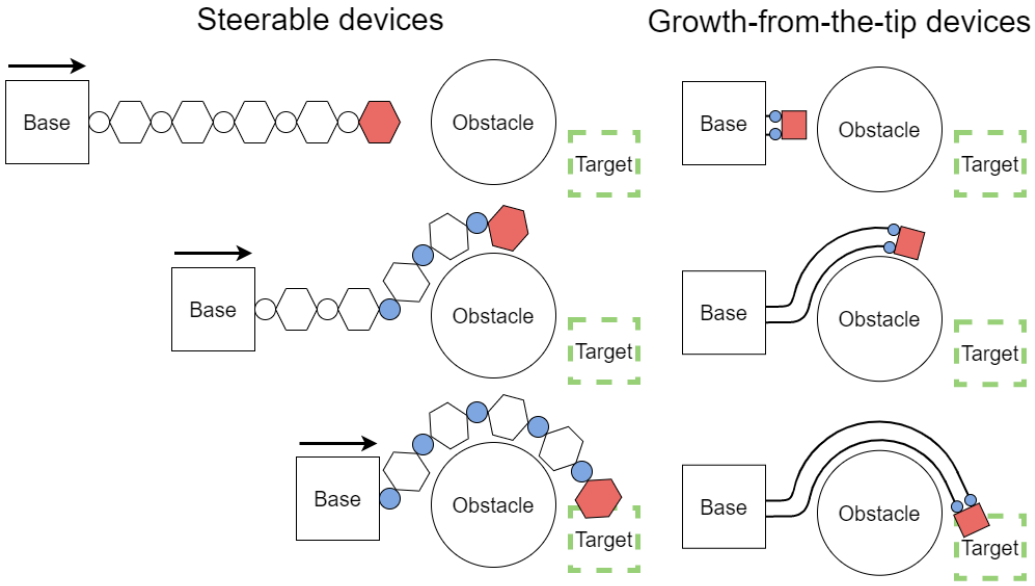

Figure 1.4: **Comparison between steerable and growth-from-the-tip devices circumventing an obstacle and approaching a target. The tip (or leader segment) is indicated in red and each active steering action is indicated in blue.**

1.1.3 Growth from the tip

Growth from the tip is a specific type of movement observed in nature, at for example plant roots, fungal *hyphae* and developing neurons [16, 17]. Root growth can artificially be simplified to an irreversible increase in mass at the tip with changing functionalities and morphology [18], resulting in extension from the tip. The direction of the growth action can passively and actively be controlled [16]. By the kinematic dependency of the body created earlier, a growth-from-the-tip device is a non-holonomic system [19]. In other words, the device's steering actions are inseparable from historic translations and orientations.

Interestingly, growth through the addition of material at the tip, allows for multi-directional tip elongation at any point of a trajectory, without moving the entire body [19], as visualized in Figure 1.4. In fact, growth-from-the-tip mechanisms can extend and curve in any direction infinitely often, provided that sufficient material is supplied. Therefore, growth is fundamentally different than the working mechanisms of current surgical devices, in which forward movement is applied externally and the complexity of movement depends on the internal DOFs of the device. The relative movement of the device with respect to the direct environment creates undesired friction and consequently injury risk or pain for a patient. In contrast, growth-from-the-tip creates a static solidified structure where only the tip moves. However, in some cases the material supply is designed to move as well, especially at large extension ratios with a large material demand. Therefore, an internal material supply, comparable to plant roots, would again result in limited interaction with the environment.

Maneuverability of steerable devices is expressed in internal DOFs, since steering of all segments is performed while moving the whole body. In contrast, a growth-from-the-tip device only moves and steers at the tip. Therefore, more applicable metrics determining maneuverability of growth-from-the-tip devices comprise complexity of the trajectory (*e.g.* type of obstacles, amount of curves and curvature radius) and DOFs of the tip at any point of the trajectory. In essence, the complexity of a path that can be followed is not limited by internal DOFs. Other advantages of growth-from-the-tip comprise reduced shear forces exerted on the environment, high extension ratios (given that sufficient material is supplied) and the creation of increasingly complex movements.

A final actively-steering concept comprises remote-controlled vehicles or robots that require no direct support from their environment. A flying drone for example, uses air to manoeuvre in various directions. However, once a trajectory is tiny, constrained by compliant tissue and (almost) no gas is available, a remote-controlled vehicle needs its surroundings to direct movement. In contrast, a growth-from-the-tip device only requires a distant and supporting base to translate and actively curve at the tip.

1.2 State of the Art

1.2.1 Literature search

To further examine the large potential of growth-from-the-tip devices, a more elaborate literature search was performed on this topic, using te *advanced search* of the Scopus database. The search string is visualized in Figure 1.

	TITLE		**TITLE-ABS-KEY**	
	AND			
OR	grow*	robot*	extend*	mechanic*
		machin*	mov*	biomechanic*
		device	steer*	robot*
		apparatus	obstacle w/1 avoidance	

Table 1: **Visualization of Search string entered in Scopus, using a combination of 'OR' (rows), 'AND' (columns), and 'Within' (W/n) functions, where the term before the 'W/n' function has to be found within a distance of 'n' terms.**

This search resulted in 56 articles. After title and abstract screening, 18 articles were selected based on the presence of some type of growth-from-the-tip behavior. On top of that, 3 articles found by generic searches were included in the final selection, which on its turn, is categorized according to their working principle. Secondary literature was only consulted when detailed information was missing.

The designs found in literature are categorized according to their distinctive growth process at the tip. Even though growth-from-the-tip is accompanied with some type of solidifying process at the tip, the key distinctive feature is whether the input material is transformed or not. The input material is transformed when most of the micro-structure is temporarily or permanently changed, in this case towards a solidified state. Note that temporal changes in micro-structure include elastic deformation and piëzo-electric behavior.

The question arises: "How can a non-transforming material solidify at the tip?". In some way or another, a certain type of solid blocks, referred as modules, are able to relatively move until arriving at the tip. There, the modules have to eliminate their relative movement in order to solidify. If these modules can move freely without relative constraints, these modules are referred as independent. In the case of relative constraints like linkage, these modules are referred as dependent. In accordance with the above motivated categorization, the literature search results are treated in line with the following distinctive principles:

- Transforming through phase change
- Transforming through deformation
- Transforming through another process
- Non-transforming independent modules
- Non-transforming dependent modules

An example of *transforming through phase change* would be additive manufacturing technology, since the micro-structure of the input material is rigoriously changed through phase changes into a solidified structure. In contrast, multiple independent solid modules do not transform, but they can move and lock with respect to one another. It should be noted that no examples of growth-from-the-tip based on another type of transformation were found.

Transforming through phase change

Additive Manufacturing (AM) is predominantly based on the building of solid structures by transforming material through phase changes. More specifically, AM is standardized as: '*The process of joining materials to make objects from 3D model data, usually layer upon layer, as opposed to subtractive manufacturing methodologies, such as traditional machining* ' [20, 21]. Note that *'joining material'* does not necessarily imply transformation of most of the input material, like binder jetting and sheet lamination. Therefore, these specific type of AM techniques

are referred as non-transforming dependent material with additional chemical attachment.

A root growth inspired AM robot deposits material by a rotary Fusion Deposition Modeling (FDM) device, located at the tip, as visualized in Figure 1.5 and described by Sadeghi *et al.* [22, 23, 24] and Del Dottore *et al.* [18, 25]. The robot grows autonomously through layer-by-layer addition of input material (*i.e.* polypropylene (PP) or thermoplastic PLA filament). The system curves by differential material supply per side, realized by variable amount of layers per side or differential layer thicknesses [18]. The stationary zone is a hollow cylindrical structure through which material can be supplied by a spool. The rotary deposition of material through a nozzle pushes the tip forward [22].

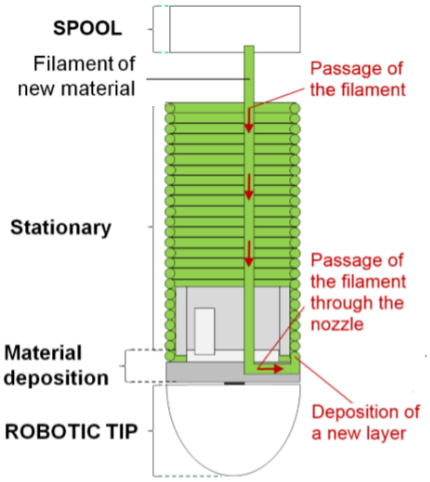

Figure 1.5: **Schematic representation additive manufacturing based growth-from-the-tip involving rotary layer-by-layer Fusion Deposition Modeling (FDM) with polypropylene (PP) or thermoplastic PLA filament. (Figure adapted from Sadeghi [22])**

In contrast with layer-by-layer deposition and in line with the fountain-like material addition performed by plant roots [26], Lunni *et al.* [27] created an extrusion based additive manufacturing technique, where material is supplied through the hallow structure, after which it is melted at the tip and consequently cooled if the tip has moved on to a certain distance. A visualization is given in Figure 1.6.

In conclusion, additive manufacturing technologies offer various advantages, like being able to build new type of geometrically complex structures and materials [28]. However, major challenges are inferior and anisotropic mechanical properties resulting from layer-by-layer printing and anisotropic heat penetration. Moreover, large structures or mass production seem to offer limited applications for additive manufacturing technologies [29]. In addition, 3D printing is known to be a time-consuming process that requires tight control. Lastly, growth actions are difficult to reverse.

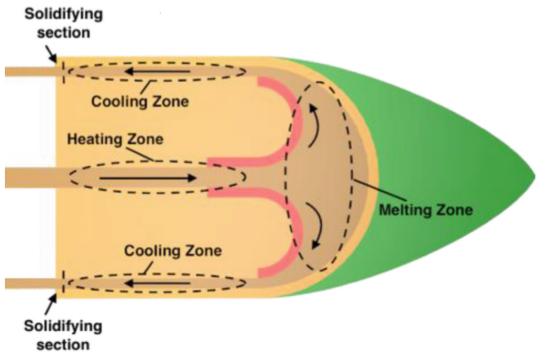

Figure 1.6: **Schematic visualization of growth from the tip with extrusion-based additive manufacturing technique, inspired by root growth. Heating, cooling and melting zones, combined with flow direction are indicated. (Figure adapted from Lunni [27])**

Transforming through deformation

The second growth-from-the-tip principle found in literature is skin eversion, as described by Hawkes *et al.* [16] and Greer *et al.* [30] and visualized in Figure 1.7. In this case, tip elongation is driven by pressurized chambers, which force the skin to evert. The skin supply determines the eventual elongation (per chamber). As a direct consequence of adding material at the tip, movement with respect to the environment only occurs at the tip [18]. Skin eversion is categorized as transforming through deformation. During eversion, the skin is bended and stretched by inflation. This can be debated as the skin being bended in place and solidified by elastic deformation, which is interpreted as a temporal change in micro-structure.

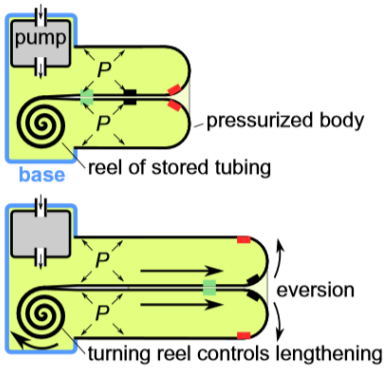

Figure 1.7: **Schematic representation of growth-from-the-tip with everting soft skin, driven by pressurized air chambers. (Figure adapted from Hawkes [16])**

The most predominant advantages of this mechanism are the high elongation rates (*i.e.* up to 10 m/s over short distances) and the large extension ratios ((72m-0.28m)/0.28m = 256). Even though diameters of 1.8mm are achieved, practical diameters range from 2.5cm to 36cm [16].

Literature offers multiple control options for curvature of everting skin mechanisms, comprising differential skin-supply rates [16], small pneumatic chambers along the side of the structure, Series Pneumatic Artificial Muscles (sPAMs) (which contract when inflated) [30] and obstacle-aided bending [31]. Interestingly, SPAMs can decouple steering and extension during movement.

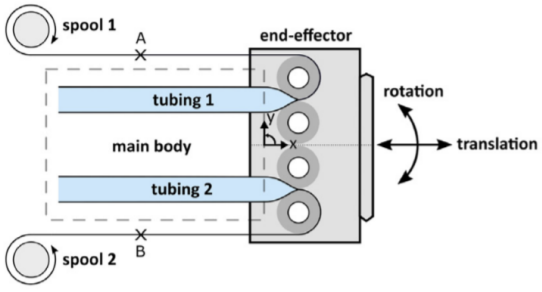

Figure 1.8: **Schematic representation of inflatable soft skin mechanism with externally supplied material from a spool. This configuration consists of a double pinch-roller mechanism with an end-effector able to translate and rotate (2DOFs). (Figure adapted from Baydere [32])**

Another type of inflated-skin-based system that does not use eversion is found. In contrast with the everting turn-inside-out mechanisms, this practically is a turn-outside-in mechanism, as described by Baydere *et al.* [32] and Tutce *et al.* [33]. Moreover, the tip is controlled and chambers can be inflated at different rates, as can be seen in Figure 1.8. Like the skin eversion, propulsion and curvature is generated by the inflation of thin-walled tubes and differential tube supply [33].

One major challenge of soft skin inflation is the sensitivity for environmental contact and disturbances due to their continuum nature, resulting in unpredictable and partly uncontrollable dynamics [30]. Accordingly, the creation of multiple active curves in series easily becomes inaccurate.

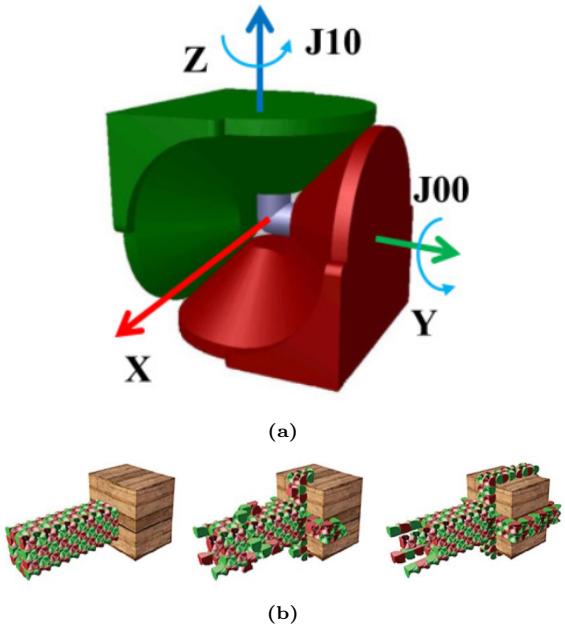

Figure 1.9: **(a) Visualization of single independent robot (Ubot), able to connect, disconnect and rotate with respect to similar modules at the flat sides. Within this configuration, rotation around the Y and Z axis are unconstrained. Subfigure (b) shows collaboration of multiple robots moving around an obstacle. (Figure adapted from Wang [34]) and Bie [35]**

Non-transforming independent modules

In contrast with transforming material, non-

transforming modules can continuously be deposited at the tip, to realize growth-from-the-tip. In the independent module case, tip elongation by the addition of material is performed by multiple independent robots able to change relative position and orientation, as described by Bie *et al.* [35] and Wang *et al.* [34]. Each single module, visualized in Figure 1.9, is an independent robot with battery, sensing, computing, and locomotion. More specifically, it can connect, disconnect and rotate (with 2 DOFs) with respect to other modules in a decentralized manner. A certain dependency is implied because these modules need to connect and disconnect to each-other. One can imagine that fully unconstrained modules are even more independent than the above-mentioned Ubots.

Non-transforming dependent modules

Multiple modules do not have to be independent, if the modules constrain each-other. A centralized material supply already implicates dependency. Moreover, modules linked together are most certainly dependent.

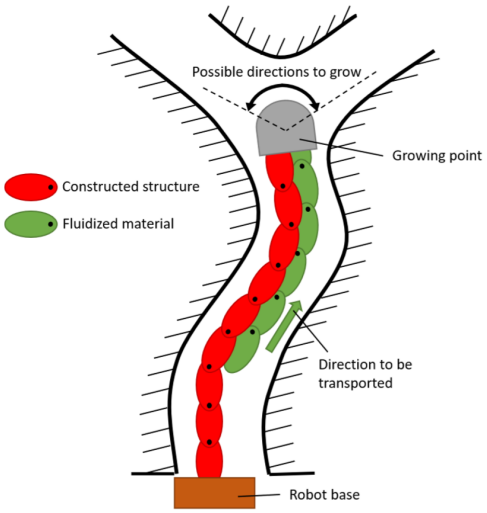

Figure 1.10: **Schematic representation of growth-from-the-tip robot with chain mechanisms, able to rotate and lock with respect to each other. Red chains are locked and green chains are unlocked. (Figure adapted from Yan [36])**

Interestingly, linked modules (*e.g.* chain mechanisms) with locking systems can both be flexible and rigid. In line with this principle, Yan *et al.* [36] prototyped a growth-from-the-tip robot with a chain mechanism able to be both fluid and rigid, as can be seen in Figure 9.1.

According to Yan *et al.* [36], the design can be improved regarding interaction with the environment, strength performance, load bearing capacity and control.

1.2.2 Patent search

Patents in the field of growth-from-the-tip are identified using multiple search strings entered in Escpacenet *Advanced Search*, as visualized in table 2. The focus of this search comprises growing-like robots that add material at a tip. The results are categorized in accordance with their Cooperative Patent Classification (CPC), as can be seen in Appendix A. Categorization helps to find more elaborate results, because, for example, additive manufacturing technology (B33) is one of many shaping techniques (B21-B33). Moreover, growing devices are some type of *travelling land vehicles having other ground-engaging means than wheels or an endless track* (B62D57/00). Interestingly, fluid-actuated devices for displacing a member from one position to another are coded by F15B15/00. As as result, search strings incorporating CPC codes were also constituted and entered, as visualized in table 2.

Verbal search

(ti any "3D printing additive manufacturing" AND ti all "structure*" AND ti any "propuls* grow* move* extend*" AND ctxt any "robot* apparat* device machin*") NOT nftxt = "flower monitor* plant* crystal* seed*"
87 results

Verbal search with time range and CPCs

ti any "3D printing additive manufacturing" AND ti any "grow* move* propag* elongat* extend*" AND desc any "degrees of freedom Multidirectional" AND pd within "2000-2020" AND cl any "B33 B62 B25 F15B15/00"
127 results

Table 2: **Search strings entered in Espacenet advanced search with the most relateable results**

After title and document screening and the addition of other search results, 9 remaining patents are briefly treated below. The removed documents did not contain growth-from-the-tip related systems.

The first patent comprises a growth from the tip device for tubular structures, as can be seen in Figure 1.11. The input material travels through an external hose and multiple nozzles placed in various cross-sectional shapes, where printing is performed. Propulsion and positioning of the printhead is performed by the wheels rolling inside the just-printed tube.

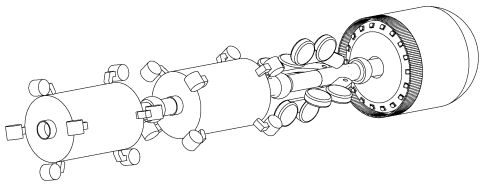

Figure 1.11: **Apparatus for Additive-Manufacturing-based growth of tubular structures, with print-head on - and print direction to the right . Espacenet CPC categories: B05, B29C and B33Y. (Figure adapted from patent US2016031155A1)**

The second selected patent grows in space, micro-gravity or offshore environments by an Extended Structural Additive Manufacturing device (ESAM) and a gripper, connected to the newly printed material. Especially the way an ESAM is connected to the printed structure is worked out. Apart from Figure 1.12, more exemplary connections are attached in Appendix B.

The third patent is already described by Greer *et al.* [30], constituting of series Pneumatic Artificial Muscles (sPAMs) through inflation. The corresponding patent number and CPCs are US2019217908A1 and B62D57 plus F15B15 respectively.

Fourthly, a more general description of a self-growing inverted tube device with steering capabilities, is patented under CN110450149A with CPC B25J9. A corresponding storage device is coded by CN110450138 and again categorized by the CPC B25J9. Moreover, certain control aspects of a self-growing soft robot in general is patented under CN110861078, also categorized by CPC B25J9. Similarly, a soft everting robot with central ejection of a fluid is patented under WO2020060858A1 with CPCs A61B1/00, B25J18 and B62D57/100.

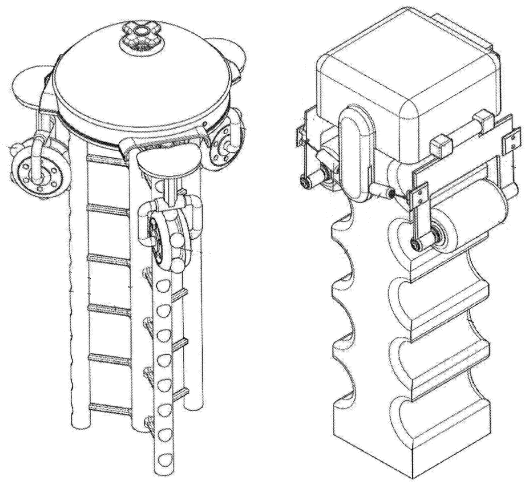

Figure 1.12: **Multiple techniques for in-space additive manufacturing resulting in growth-from-the-tip. Espacenet CPC categories: B22, B23K, B33Y and B64G1 (Figure adapted from patent CN107921564A)**

The eighth selected patent consists of a movable 3D printer connected to a base via a flexible hose, visualized in Figure 1.13. Two rollers propel the 3D printer and material is deposited through a nozzle in a layer-by layer fashion.

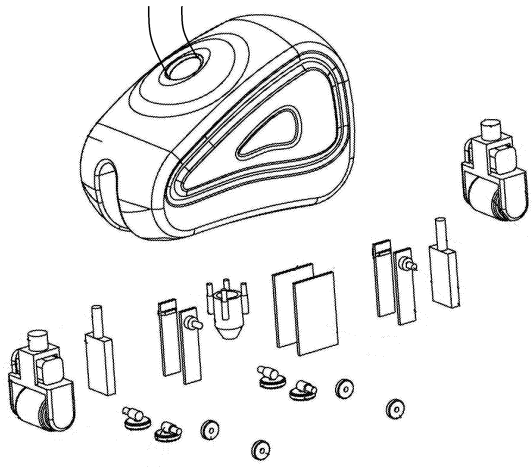

Figure 1.13: **Movable 3D printer connected to a base via a flexible hose Espacenet CPC categories: B29C64 and B33Y (Figure adapted from patent CN106564189A)**

Finally, most type of moving 3D printers can be found in CPC B33Y30/00, like for exam-

ple CN107984758A. It is worth noting that most of these mobile growth-from-the-tip 3D printers are grounded to the surroundings, making them less suitable for difficult-to-reach applications.

An overview of the literature and patent results can be found below. It is worth noting that this categorization is provisional and only meant to clarify the results.

The categorization of concentric tubes is interesting in particular. Namely, material is internally transported to tip, where it moves forward as a whole. This principle can both be interpreted as a moving steerable device at the tip and as a growth-from-the-tip device. Namely, not all steering actions are made at the tip, since the elastic interaction of concentric tubes cause all tubes to deform (to a mutual energetic stability) as material is transported to the tip. In other words, transformation of the input material and curvature creation do not only happen at the tip, in contrast to growth-from-the-tip. Still, material is transported to the tip, where it deforms. Subsequently, the tip is pushed forward on top of this built structure.

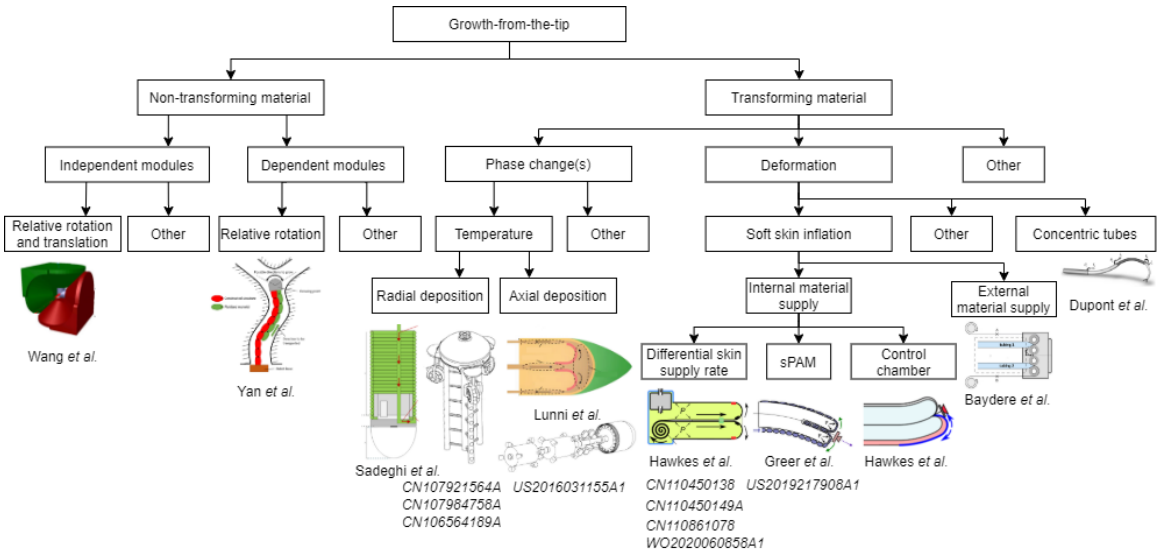

Figure 1.14: **Overview of State of the Art growth-from-the-tip devices. Multiple groups are not further specified and referred as 'other'. Especially these groups can lead to innovation.**

1.3 Problem statement

Apart from the aforementioned opportunities of growth-from-the-tip based systems, some challenging problems arise. The most commonly-known challenges related to growth-from-the-tip are speed and size. In nature, soil penetration by a growing root typically occurs at 0.006 to 0.025 meters per day [37] and the only known root growth inspired 3D printing robot elongates with 3 to 4 millimeters per minute with an average diameter of 46 mm [25, 24], which is too slow and too large for any surgical application.

In addition, the application field of growth-from-the-tip can be enlarged when the movement is reversible. That does not mean there are no potential applications for non-reversible growth-from-the-tip devices, like printing blood vessel stands or the formation of complex reinforcing structures and tunnels. Still, the creation of a lasting support structure which is also withdrawable, is in general more promising.

Moreover, current devices can be improved regarding load bearing capacity and strength performance. Especially soft skin robots are sensitive to external loads and even the seemingly robust robot of Yan *et al.* [36] lacks strength and load bearing capacity. This load bearing capacity is adopted as the main determinant of the device's accuracy, as will later be described.

Finally, most of the current devices in-

teract with the environment by the supply of material, which is not desired in surgical operations.

1.4 Main goal

Some problems primarily determine the working principle of the design, while other problems can mainly be tackled after choosing a working principle. Accordingly, size, speed, load bearing capacity and interaction with the environment are secondary goals of this work, while the innovative working principle is primarily determined by the device's reversibility and the ability to create multiple curvatures in series. Therefore, the main goal of this work is:

Design of a reversible growth-from-the-tip device following a complex trajectory.

Where a complex trajectory is defined as a path with at least 2 curves in series.

It is worth noting that the tracking of a trajectory (with sensing and perception) will not be in scope of this study. This work namely aims to find innovative working mechanisms instead of endoscopic-like systems. On top of that, this work serves exploratory goals for innovative designs, employed by the BioMechanical Engineering (BME) department of TU Delft.

1.5 Structure

In Chapter 2, more specified design requirements are generated to solve the problem stated above. Then, concepts are generated by using the ACR-REX (*i.e.* Abstracting, Categorizing, Reflecting, Reformulating and Extending) method, as described by Breedveld *et al.* [38]. Subsequently, concept selection based on the design criteria leads to the best-fitting concept. In Chapter 3, this first concept is worked out in more detail. Only relevant design choices and the final design are included. Based on experiments, this prototyped proof-of-principle is evaluated in Chapter 4. By the iterative design nature of this work, a second prototype will be constructed in Chapter 5 and evaluated in Chapter 6. Finally, the main findings, limitations and recommendations of this work will be treated in the Discussion.

It is worth noting that this process is not executed chronologically, instead, it is an iterative design process as visualized in Figure 1.15.

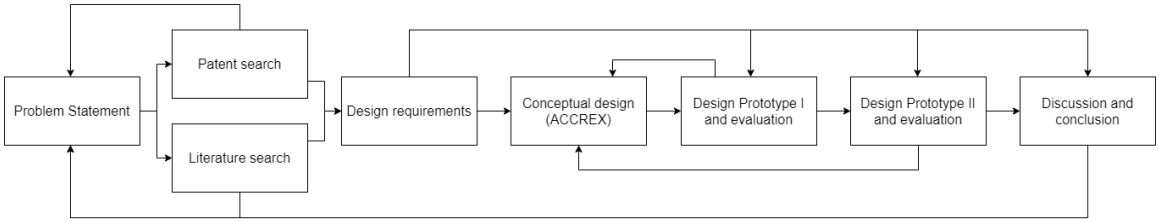

Figure 1.15: **Visualization of iterative process of this work**

2 Conceptualization

Within this chapter, design requirements are formulated and concepts will be generated in accordance with the ACRREX method, as described by Breedveld *et al.* [38]. Subsequently, one concept that performs best on the selection criteria is selected.

2.1 Design requirements

Based on the main goal and the related State of the Art, challenging design requirements are constructed. These are explained and listed below.

First, the validation of accuracy needs some additional explanation. A commonly used expression for accuracy related to path-following, is the ratio between the deviation from a path and insertion length. For example, the maximum deviation divided by insertion length for FTL devices ranges from 2.9 to 36% [39, 2]. Note that accuracy is not only dependent on path length, but also on path shape and velocity of the apparatus. Within this work, accuracy is expressed by the ratio of path deviation and insertion length, accompanied with speed and path shape information.

Then, the other design requirements comprise:

- The device will have active control of all growth actions, in line with Yan *et al.* [36]:
  - Transport 'fluidized' material to the tip
  - Transform material into solid structure from the tip to generate growth.
  - Realize forward movement and steering at the tip
  - Reverse the above-mentioned growth actions
- The device follows a path with at least 2 curves in series in combination with curves of at least 22.5 degrees [7].
- Accuracy is at least 36%, measured in deviation ($d(l)$) from a path divided by path length (l).
- Robustness of solidified material, with perpendicular load bearing capacity of 500g per unit length (as roughly described by Yan *et al.* [36]) with a maximal angular deviation of 25 degrees.
- Diameter (D) (or width in the case of planar movement) of device is in the range of 5mm to 360mm. [16, 2].
- Ratio of minimal curvature radius (r_{min}) and the devices' diameter are maximally 5.8, based on HARP 58mm/10mm = 5.8 [14], *Accura* 19mm/2mm = 8 [7] and *Memoflex* 35mm/5mm = 7 [2].
- Elongation rate is in the range of 1-10 m/s if it is inflatable [16], if not, it should be larger than 3-4 millimeters per minute [24].

When the prototype meets the above mentioned criteria, requirements can be elaborated to the following secondary design requirements.

- Limited interaction with environment, demonstrated by movement around obstacles and through sticky fly paper, nails and glue, as described by Hawkes *et al.* [16]. Or normal and shear forces can be measured.
- Large (theoretical) extension ratio, comparable to ratio of Hawkes *et al.* [16] (72m-0.28m/0.28m).

To visualize the spatial design requirements, Figure 2.1 shows a random path with multiple curves in series of at least 22.5 degrees. The allowed radial deviation ($d(l)$) increases linearly with insertion length (l). Moreover, the tip's Diameter (D), the minimal curvature radius (r_{min}) and the initial length (l_0) are specified.

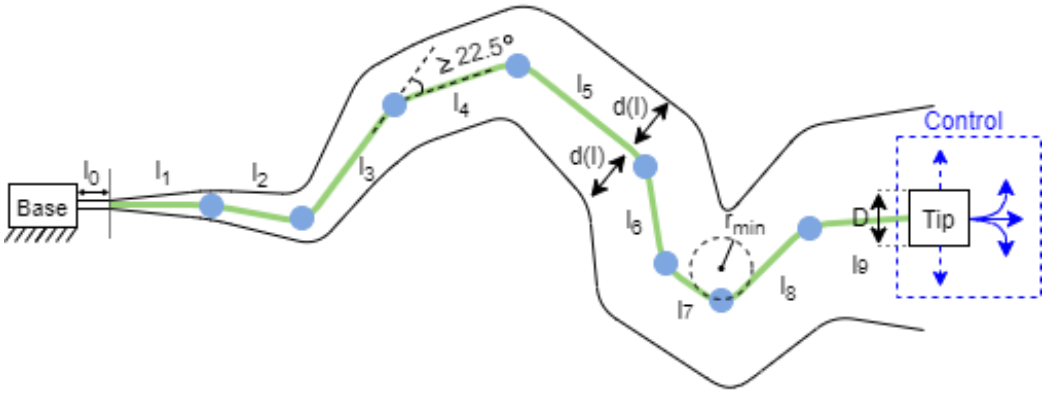

Figure 2.1: **Visualization of a complex trajectory (in 2D) in accordance with design requirements. The device consists of a base, a solidified structure (green) and a growing tip with diameter *D*, which follows a trajectory of length *l* (where l = $\sum l(i)$) with in this case 8 curves (blue dots) of each minimally 22.5 degrees and the smallest achieved curvature radius r_{min} = 19mm. The final length (l_{final}) divided by the initial length (l_0) is defined as the extension ratio. The allowed radial deviation (*d(l)*) increases linearly with *l*. By disregarding rotation around the longitudinal axis and radial translation, the controllable tip has 2 DOFs in 2D space and 3 DOFs in 3D space at any point of the trajectory.**

2.2 Abstraction

Abstraction of the main problem results in multiple sub-problems and sub-solutions. Mutually exclusive and collectively exhaustive categorization will help to find voids in current knowledge. Further reflection, reformulation and extension of the solution space will serve concept generation. Since these steps form an iterative cycle, only the final abstraction, categorization and concepts will be treated.

By the explorative nature of this work, more general concepts related to growth-from-the-tip will be generated. After a rapidly diverging solution space, concept evaluation based on selection criteria, including reversibility, aims to converge to one concept. This final concept will be worked out in Chapter 3.

First, the main research question can be simplified and split up in functional working mechanisms. In essence, growth-from-the-tip implies that some type of material needs to be transported to a tip, where the material is transformed into a solid state. The tip pushes itself forward on top of this built structure. Consequently, the tip can translate and curve in any direction. Apart from this type of movement, the created body and the tip needs to be retracted. The above-mentioned description results in four sub-questions:

- What type of transportable building material can be used?
- What happens to the input material in order to form a steerable, growing and solidified structure?
- How can material be supplied to the tip?
- How can the structure be withdrawn?

2.3 Categorization

By the broad set of growth-from-the-tip systems and in order to prevent a too extensive and confusing overview, the sub-questions are categorized separately. It is worth noting that categorizations mainly serve inspiration for concept generation and can be made with different angles of incidence.

First, the most distinguishable part of the design is the type of input material which should be positioned at the tip. Accordingly, the first sub-question states:

What type of transportable building material can be used?

Growth-from-the-tip building material needs to be transportable and it should be able to solidify. The input material does not have to transform (*e.g.* melt, react or deform) in order to solidify. For example, the chain elements of Yan *et al.* [36]

lock with respect to each other, but do not transform. Since the binary choice to transform or not, largely determines the type of input material, the distinction is incorporated in the building material categorization in Figure 2.2. In addition, non-transforming input material should be structurally solid to form a solidified body without any transformation. In contrast, transforming material can be gaseous, fluid, solid or a combination of phase states.

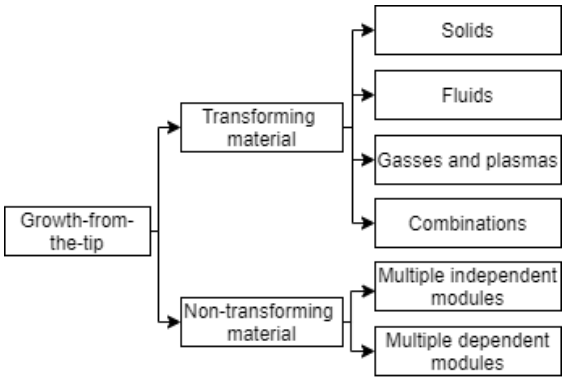

Figure 2.2: **Categorization of growth-from-the-tip building material**

The non-transforming building blocks can be dependent (*e.g.* linked or compacted) and independent, where each block can move freely without constraints imposed by other building blocks. The robots of Wang *et al.* [34] need to link and unlink to each other in order to move with respect to one another. However, these robots have individualistic control and relative movement. Therefore, Ubots can be regarded partly independent. Interestingly, even more independent robots can be generated within a growth-from-the-tip design, like a group of drones. The second most distinctive function is the type of transformation, as stated below.

What happens to the input material in order to form a steerable, growing and solidified structure?

By the distinction made in the previous subquestion, two separate categorizations are made, comprising transforming and non-transforming materials. Without transforming the building blocks, the solid blocks can be solidified with respect to each other by passively and actively induced forces, as categorized in Figure 2.3.

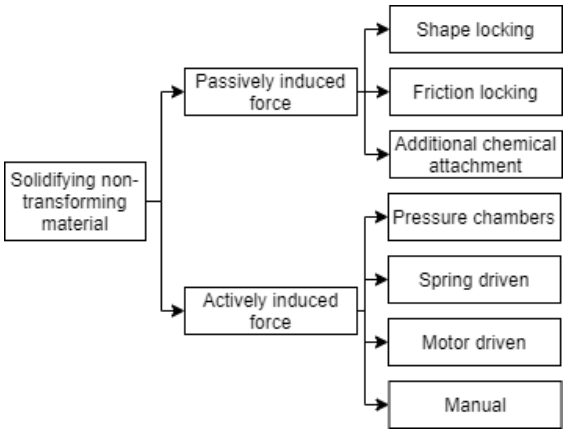

Figure 2.3: **Categorization of non-transforming materials that solidify with respect to each-other.**

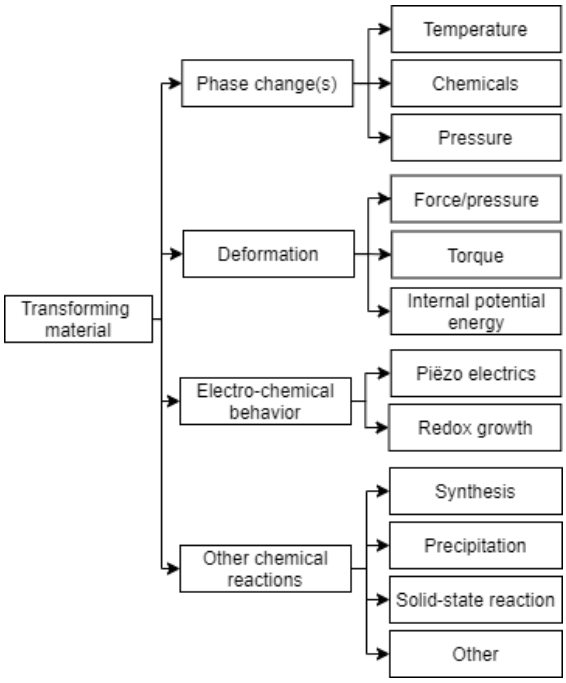

Figure 2.4: **Categorization of transforming materials resulting in solidified material.**

In contrast, the transforming building material can be adapted by phase change(s), deformation, electro-chemical behavior and a wide variety of chemical reactions, as visualized in figure 2.4. Obviously, the type of process towards a solidified structure is almost not bounded. For that

reason, the *Other chemical reaction* box can contain many other solutions.

How will the input material be supplied and positioned?

Apart from the above-mentioned divisions, material can be supplied by one centralized system, or multiple decentralized systems. Decentralized systems range from several local systems that mainly work independently, to material that can fully supply itself, like the Ubots described by Wang *et al.* [34]. An elaborate division can be found for centralized material transports, as can be seen in Figure 2.5.

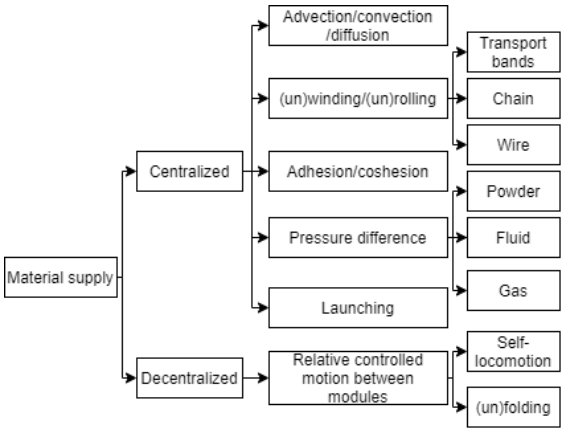

Figure 2.5: **Categorization of material supply mechanisms**

The actual (de)positioning can be done in a centralized or decentralized and continuous or discontinuous fashion, as shown in figure 2.6. Moreover, centralized positioning has directional components (*e.g.* axial, radial and circumferential) and decentralized positioning is dependent on relative degrees of freedom.

How can the structure be withdrawn?

This last question can briefly be answered, since the term withdrawal is more specified than removal. The term 'removal' namely includes structure dissolution or break down by the surroundings. However, this would be out of scope for this study.

In short, a structure can be withdrawn by a reversed growth-from-the-tip process or it can be pulled-back as a whole. The latter involves challenges regarding obstacle avoidance. Namely, if the device is curved around an obstacle and retracted as a whole, the device should at least become flexible to reduce damage. A growth-from-the-tip process can be reversed by an opposing system or by a similar system that is fully reversible.

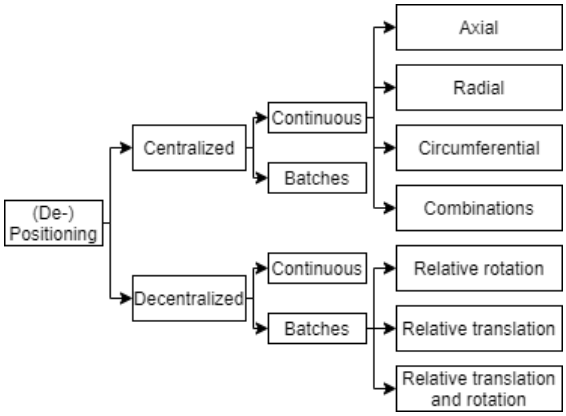

Figure 2.6: **Categorization of (de)positioning of materials**

Finally, it should be noted that rigorously different categorizations can be made with other points of view. Still, the large amount of design options for this categorization is clear, which serves as inspiration for the next section.

2.4 Concept generation

Categorization of sub-functions and design choices naturally lead to a wide variety of concepts. The most distinct concepts will be treated below. Each concept is color-coded with blue representing solidified material (*i.e.* the created support structure) and green the fluidized material (*i.e.* the building material that is being supplied). Note that many details are left-out for simplicity.

The first two concepts use non-transforming materials that solidify by shape locking. The systems incorporated a centralized and continuous material supply. Concept 1 specifically, piles up solid disks while pushing itself forward on top of the built structure by a caterpillar, as shown in figure 2.7.

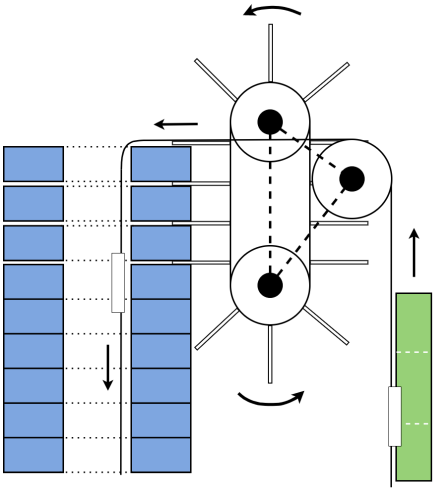

Figure 2.7: **Concept 1 - Longitudinal cross-section of pile-up apparatus with external supply of solid disks with a central hole. Steering is realized by horizontal displacement or the supply of variable disk shapes. The apparatus can be reversed.**

This caterpillar can generate grip by temporarily place arms between disks. This concept can be compared to the building of skyscrapers, which is also a type of growth-from-the-tip. Namely, building material is transported to the tip, where it is transformed. Moreover, the building site moves up with the created structure.

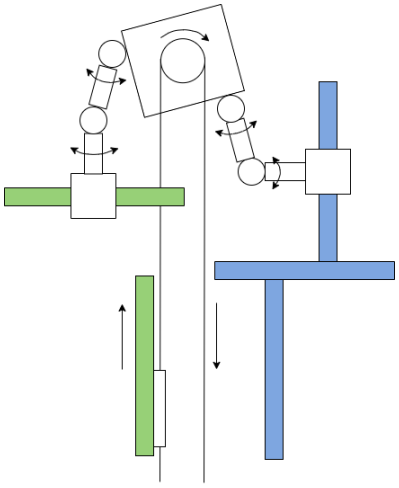

Figure 2.8: **Concept 2 - Side view of independent building robot able to clamp to building blocks and to displace.**

The second concept comprises a building robot that moves around the built structure while it puts building blocks in place. By grabbing and releasing blocks, the robot can move (blocks) around, as indicated in figure 2.8. A continuous material supply is drawn, but the robot would also be able to pick up building blocks by itself. This is different than patent CN107921564A, since no AM technology is used. Depending on the building blocks, steering and reversibility can be incorporated.

The third concept is categorized as a deforming material using shape locking with centralized material supply in batches. By applying current, as indicated in Figure 2.9, an upward Lorentz force occurs, driving the block upwards. Once arrived at the tip, the block extends and becomes a solid and conductive part of the structure. First, the spring is conductive (green), after which it becomes non-conductive, as indicated in red. Steering can be realized by using variable block shapes.

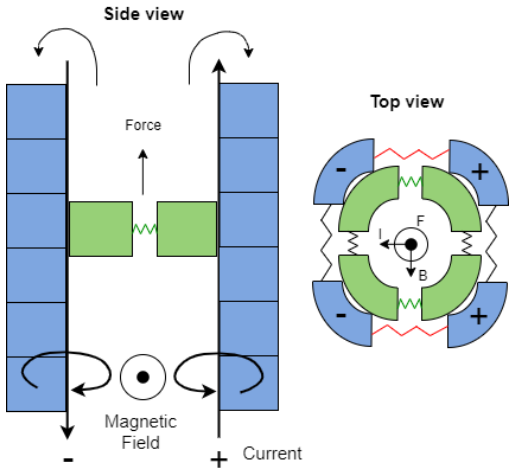

Figure 2.9: **Concept 3 - Side and top view of pile-up apparatus with radially extendable and conductive blocks. The application of current results in an upwards Lorentz force.**

Concept 4 consists of independent modules able to move themselves to the tip, as shown in figure 2.10. The building material itself does not transform but currents and magnetic fields are changing per leg. The solidified blocks are held together by an actively induced magnetic force. Curvature can be generated by using variable building blocks.

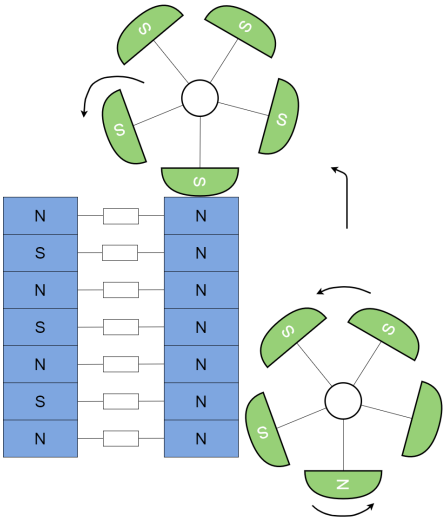

Figure 2.10: **Concept 4 - Longitudinal cross section of multiple independent modules able to change magnetic polarity per leg.**

Concept 5 is a continuous axial additive manufacturing device supplied by material that can be transformed by phase changes or other chemical reactions (*e.g.* PUR and foam). This concept is visualized in figure 2.11.

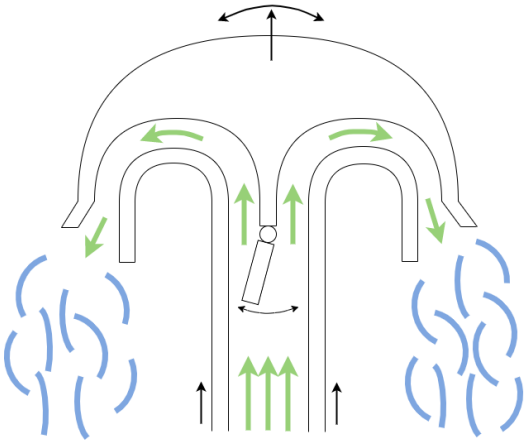

Figure 2.11: **Concept 5 - Longitudinal cross section of a continuous axial additive manufacturing device being supplied with fluidized (*i.e.* fluid or powder) material.**

Differential material supply per side results in rotation of the tip. It is worth noting that only parts of the material supply are drawn. Ideally, the created structure in combination with pressurized material, will guide the material to the tip. Withdrawal can be performed by pulling the tip and sucking the material in and remelting.

In contrast, Concept 6 grows by transforming material electro-chemically, using a cathodic/reduction type of additive manufacturing, as visualized in Figure 2.12. A copper sulfate (CuSO4) solution and a solid copper (Cu) cathode are potential options. Anodes and salt bridges are dispensable and consequently not drawn. Note that this type of growth can potentially be produced on micro-scale. Steering is achieved via differential material supply and withdrawal by adding a stronger cathode at the tip (dotted blue rectangle).

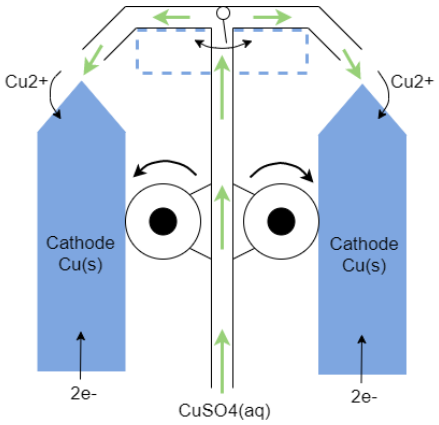

Figure 2.12: **Concept 6 - Longitudinal cross section of a cathodic/reduction type of additive manufacturing.**

Concept 7 constitutes everting chains that can lock with respect to one-another, as shown in Figure 2.13. The concept is categorized as non-transforming and dependent modules with continuous and multiple material supplies. Two supply wheels (indicated with black dots) are connected to the locking system (dotted rectangle). The central material supply with multiple chains results in evertion, reducing interaction with the environment. Steering is achieved by differential chain supply and relative rotation of chain modules. The system is fully reversible by changing the direction of the supply wheels and unlocking the chains.

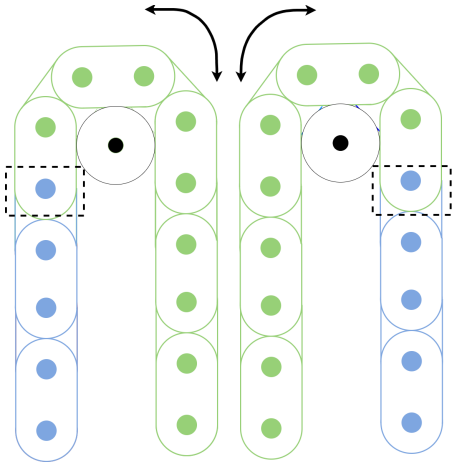

Figure 2.13: **Concept 7 - Side view of everting chains that can lock their relative rotation, as indicated in green.**

Finally, Concept 8 practically is an everting soft continuum device with series Pneumatic Artificial Muscles (sPAMs). The soft skin of the robot continuously deforms until inflated. Therefore, the concept is categorized as transforming by deformation with a continuous and centralized material supply.

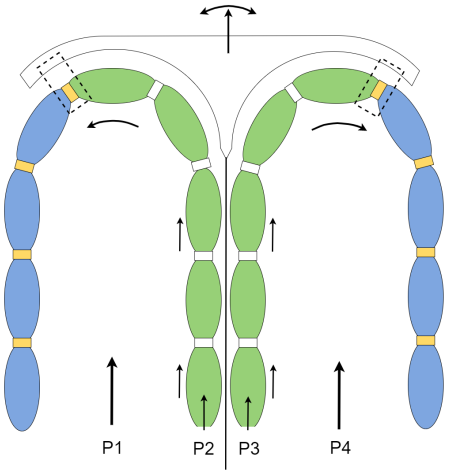

Figure 2.14: **Concept 8 - Longitudinal cross section of everting soft continuum device with series Pneumatic Artificial Muscles (sPAMs).**

The eversion is driven by internal pressure P1 and P4 and the central skin supply, as shown in figure 2.14. The distinctive feature is a controlled sealing per PAM, being supplied in open condition (white rectangles) and being closed (yellow rectangles) at the tip (more specifically, at the dotted rectangle). Each sPAM can be inflated individually at the tip with pressure P2 and P3. The structure can be withdrawn by spools at the base (not drawn).

2.5 Concept selection

In order to select the best fitting design, the selection criteria are in line with the design requirements and preferences, as is listed below.

- Reversibility
- Simplicity of design
- Expected accuracy for a path of multiple curves in series
- Manufacturability
- Robustness of built structure
- Small minimal curvature radius
- Limited interaction with environment
- Large theoretical extension ratio
- Elongation rate
- Down-size-ability

Weight factors are incorporated in accordance with the main goal of this work, as shown in table 3. Namely, reversibility and accuracy are main focus points of this study, while elongation rate and extension ratios are secondary goals. Moreover, manufacturability and simplicity of the design are as well competitive requirements, as realistic time-frames for this work.

Then the main concepts are rated 1 (very poor) to 5 (excellent) with respect to these criteria. The rating is relative to the other concepts, so each criteria delivers at least one concept with rating 1 and at least one with rating 5.

Selection criteria	**WF**	**C1**	**C2**	**C3**	**C4**	**C5**	**C6**	**C7**	**C8**
Reversibility	4	4	4	2	3	1	1	5	4
Simplicity of design	4	2	1	2	2	3	2	5	5
Expected accuracy for a path of multiple curves in series	4	4	5	2	4	1	2	5	3
Manufacturability	3	5	1	2	2	2	2	5	4
Robustness of built structure	3	4	2	3	1	3	2	5	3
Small minimal curvature radius	3	4	5	1	3	3	3	4	4
Limited interaction with environment	2	2	1	3	2	3	4	5	5
Large theoretical extension ratio	1	5	2	4	3	2	1	5	5
Elongation rate	1	4	2	4	3	5	1	5	5
Down-size-ability	1	4	1	4	2	3	5	3	4
Total:		96	71	60	66	60	56	**125**	105

Table 3: **Concept (C) selection with respect to 10 selection criteria and weight factors (WF).**

At first, concepts with partly uncontrolled material transformations and depositions (*e.g.* C3, C5 and C6) score low on reversibility, while solid mechanisms (*e.g.* C1, C2 and C7) can easily be designed for reversed motion. Secondly, the amount of mechanisms, (moving) parts and control systems determine the overall simplicity of the designs. Thirdly, the expected accuracy depends on the type of material transformations and depositions, robustness of the built structure and the controllability of all additional processes. Therefore, solid mechanisms that easily change direction (*e.g.* C2 and C7) perform better on this criterion than hard-to-steer concepts with partly uncontrolled material transformations and depositions (*e.g.* C3, C5 and C6). Moreover, the type of materials, parts, mechanisms and material transformations determine manufacturability. Furthermore, robustness of the built structure, which will be measured by perpendicular load bearing capacity, depends on the type of building blocks, type of transformation and type of adhesion between parts. Next, the minimal curvature radius of these concepts are determined by the minimal width of the structure, the way curvature is created (*e.g.* differential block shapes or variable material supply per side) and the type of material supply. Additionally, the type of material supply (*e.g.* internal and external), material deposition and the type of material transformation results in a certain interaction with the environment. A high score means low effect on the environment. Then, the theoretical extension ratio of growth-from-the-tip concepts is dependent on the type of material supply in combination with robustness of the built structure. Subsequently, elongation rate is related to the speed of material transformation and supply (*e.g.* continuous or in batches). Finally, the ability to be down-sized depends on the complexity and amount of mechanisms, processes and parts.

In conclusion, Concept 7 and 8 score highest on simplicity, interaction with the environment, theoretical extension ratio and elongation rate. Additionally, Concept 7 also performs best on reversibility, manufacturability, robustness and expected accuracy. However, minimum curvature radius and down-size-ability will probably not be optimal. Still, Concept 7 has the highest total score and will be worked out in more detail. If this concept would not work out, Concept 1 and 8 are second best options.

3 Detailed Design

3.1 General abstraction

The chosen concept can be abstracted to multiple parallel chains everting with elements that are sequentially linked. Chain segments have relative DOFs in 'fluid' state until they are locked towards solid state, as described by Yan *et al.* [36]. Note that 'locking' refers to a constraint on relative motion between segments, which can also be accomplished by active devices like springs, actuators or motors. However, each chain segment should incorporate such an active locking mechanism. For simplicity, the proof-of-principle disregards active locking mechanisms. The chains are supplied in 'fluid' condition to the tip, where the transformation into solid structure takes place. The system can always be reversed, by fluidizing the solid chains and by reversing the chain movement.

One innovative feature compared to Yan *et al.*[36], is the eversion of multiple parallel chains. Consequently, interaction with the environment is minimized in a manner similar to everting soft-skin robots as described by Hawkes *et al.* [16] and Greer *et al.* [30]. Namely, the moving material supply is now internal, resulting in limited interaction. Furthermore, strength performance and load bearing capacity of the whole system are improved. If load bearing of the total system is still problematic, longitudinal gradients in density and chain thickness can be incorporated, with the lowest weight at the tip and high load bearing capacities close to the base. The type of segments, locking mechanisms and the tip mechanism are determined in the Sections 3.2, 3.3 and 3.4, respectively. Then, a proof-of-principle is designed in Section 3.5.

3.2 Type of segments

At first, the type of links are predominantly determined by the type of connection between each segment, which in turn can be chosen based on the desired amount of relative DOFs between two bodies. The chosen concept comprises multiple segments linked in series, where the type of connections and the shape of the bodies are to be designed. Figure 3.1 illustrates two randomly shaped segments that need to be linked with relative DOFs until locked (*i.e.* no relative DOFs between the bodies).

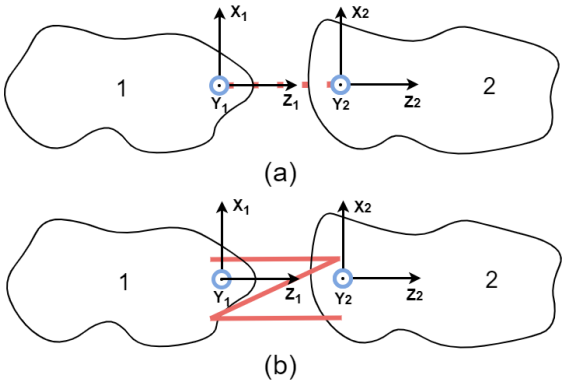

Figure 3.1: **Connection of two randomly shaped segments, with (a) fluidized connection, meaning that there are relative DOFs between body 1 and body 2 and (b) solidified/locked connection, meaning there are no relative DOFs between two segments. The segments Z-direction is always tangent to a line between the two connections of each segment.**

The two bodies visualized in Figure 3.1 can create 'curvature' by deviation in X or Y-direction of one body with respect to the other. Suitable degrees of freedom are rotation around X or Y and translation along X and Y. However, the working principle is about eversion at the tip, meaning that segments are rotated step-by-step by around 180 degrees. Consequently, segments that cannot rotate with respect to one another are not fit for this design. Therefore, segments that create curvature only by pure translations (*e.g.* T_x, T_y or T_{xy}) are disregarded.

Rotations around the Z-axis and Z-Translations can only amplify existing deviation in the X or Y-direction. In other words, Z-translations do not contribute to curvature creation, even though they can attribute to the creation of complex movements. Therefore, Z-rotations and Z-translations are regarded as out of scope.

Moreover, a rotation around Y makes a translation along X superfluous, since both result in a deviation in X-direction. All similar movements resulting in the same deviation will

not be treated. All in all, the leftover and suitable combinations can be found in table 4.

	C1	C2	C3	C4	C5
X	R		R	RT	
Y		R	R		RT

Table 4: **Suitable relative DOFs between segments with Rotations (R) and Translations (T) in 2D space, resulting in 5 Concepts (C).**

The joints are loaded by tension in Z-direction when the joints are unlocked, representing the fluidized configuration of the segments in series. In contrast, the joints are loaded by a combination of compression, torque and shear in the locked configuration. Consequently, the joints described by Jelinek *et al.* [40] serve as a source of inspiration to generate differential type of chain segments.

In order to generate chain segment concepts, categorization is based on 3 main functional properties. The first key parameter is the amount of DOFs per joint. Even though only 2 effective rotational DOFs are required, joints with 1,2 and 3 rotational DOFs are investigated, because constraints can be imposed later on. Secondly, joints are categorized by rolling, sliding, rolling as well as sliding and bending joints [40]. The last key property is about the way in which the joints are constrained in outward Z-direction (due to tension load), comprising solutions with (steering) cables and adapted joint shapes. This functional categorization generates 3*4*2=24 solutions, visualized in figures 3.2 3.3 and 3.4.

For chain segments in series, one chain segment always is part of at least 2 joints. Moreover, each 1 DOF joint comprises a Male (M) and Female (F) (*e.g.* ball and socket) part, except for bending flexure joints. In other words, a chain consists of alternating segments or alternating joint parts with similar segments. For rolling, sliding and sliding rolling joints, this point of view results in 2 configurations: -FM-FM- or -FF-MM-, where each F-M or M-F represents a joint and each FM, MF, FF or MM represents a segment.

The 2DOF joints described by Jelinek *et al.* [40] comprise 3 participating bodies. However, this third body (X) always is the middle part of a joint, resulting in similar alternating solutions (-FM-X-FM- and -FF-X-MM-). For now, a 2DOF joint with 3 participating bodies is represented as M-X-F or F-X-M.

Since these two configurations of alternation, which are not applicable to bending flexure joints, would generate 2*18 + 6 = 42 concepts in total, they are only worked out for 1DOF joints in Figure 3.2 and not fully for joints with 2 or 3 DOFs.

By comparing cable compression to shape compression, cables do not only simplify the required shape of the joints, they have additional functionalities like steering and locking.

Concepts h,i,l and m of Figure 3.2 can rotate when loaded in tension, and they are locked when loaded by compression, due to friction between two separate 'ball' segments. Note that Concepts h-n can translate in Y-direction if not constrained, which would be in line with the 'RT' solutions (C4 and C5) of table 4.

Multi-directional curvature in 3D is not only accomplished by 2 DOFs per joint. Instead, planar joints with no parallel axis of rotation can generate curvature in 3D space per segment. In other words, joints with 2 perpendicular rotations, as described by Jelinek *et al.* [40], typically are 2 planar joints with 1 DOF in series, rotated by 90 degrees.

As a result, the denomination of a joint needs further explanation. Namely, the middle segment in Figure 3.3 (a-d) can be viewed as the third body of a 2DOF joint (F-X-M). Or, one could state that two type of segments are alternating (-FF-MM-), creating 2*1DOF.

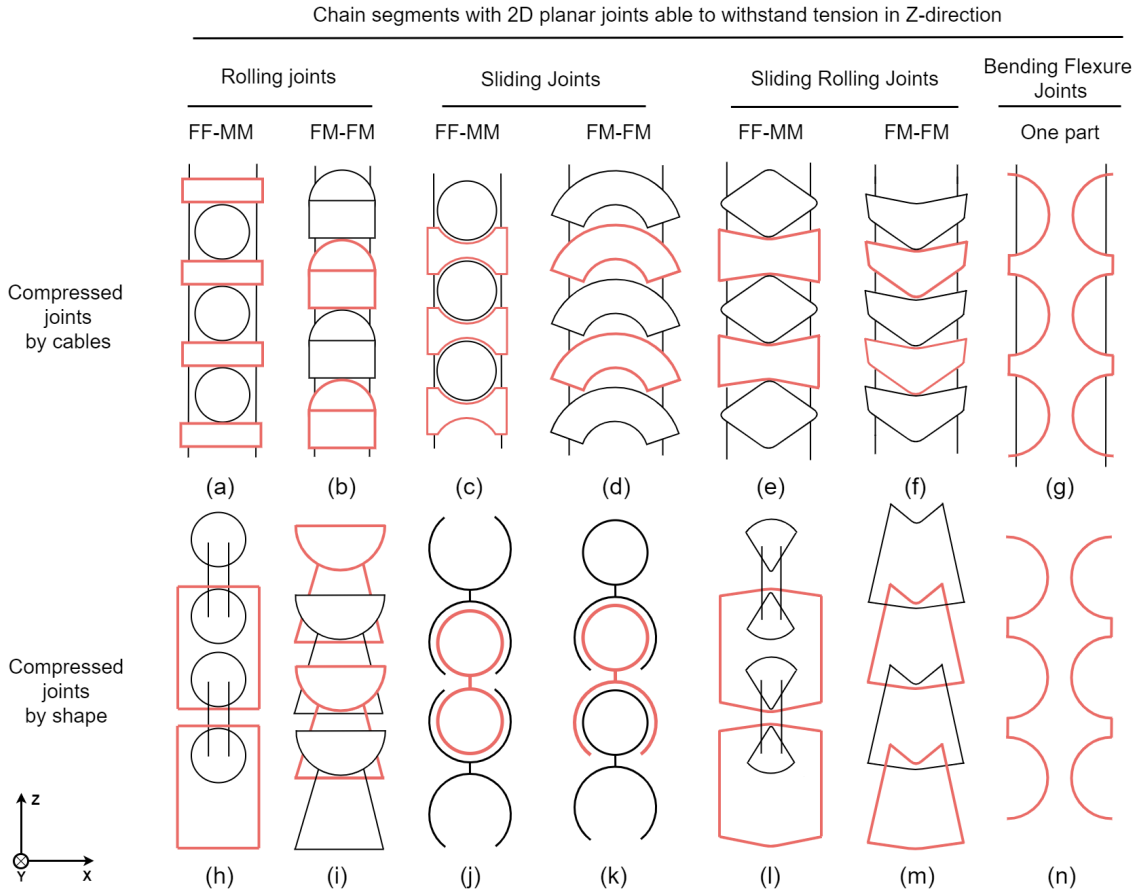

Figure 3.2: **Schematic overview of multiple chain segments in series (alternating black and red) comprising planar joints (2D) with 1 DOF (rotation around Y) in unlocked configuration. The joints are compressed in Z-direction by (steering) cables (a-g) or shape (h-n) and can be divided by Rolling, Sliding, Sliding Rolling and Bending Flexure joints. Further division is made regarding the alternation of joint parts, where each joint (F-M or M-F) consists of a Male (M) and Female (F) part and each segment consists of two joint parts (FM, MF, FF or MM). (Categorization of joints adopted from Jelinek) [40])**

Moreover, this third body 'X' actually has two sides, being a male or female part of a joint. In addition, orientation of each 1DOF joint is important, since it determines the overall (independent) DOFs.

In conclusion, X can consist of male and female joint parts with orientation denoted by a '1' or '2', resulting in the following codes of alternation:

- $M_2F_1 - M_1F_2 - M_2F_1$
- $F_2F_1 - M_1M_2 - F_2F_1$

Note the limited amount of options, enforced by the fact that each 1DOF joint consist of a Male (M) and Female (F) part with similar orientation. In other words, the theory of 2 potential configurations (*i.e.* -FF-MM- and -FM-FM-) for joints of 2DOFs holds, as described earlier. The only difference is the alternating orientation of joints, resulting in different type of segments. For example, $F_1{-}M_1M_2{-}F_2$ typically is a 2DOF joint, consisting of 3 bodies and two perpendicular 1DOF joints.

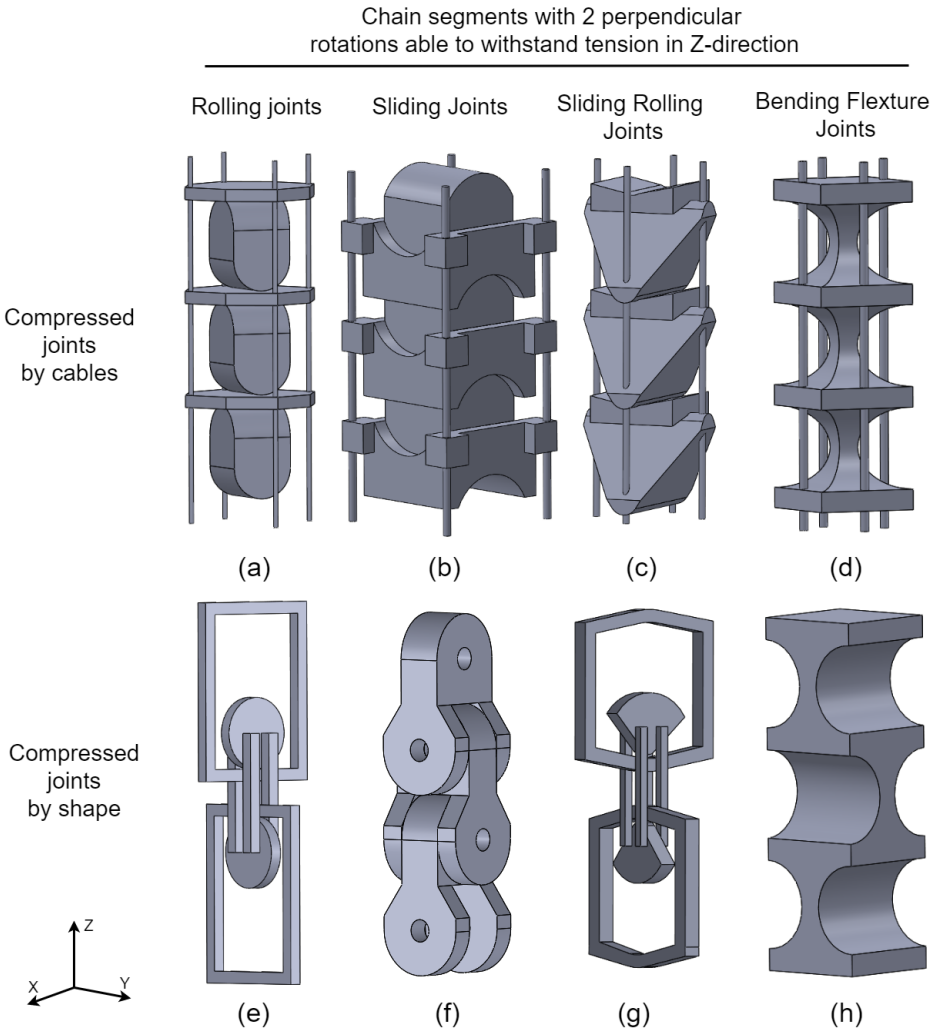

Figure 3.3: **Schematic overview of multiple chain segments in series comprising Rolling, Sliding, Sliding Rolling and Bending Flexure Joints with 2DOFs, compressed by cables (e-h) or shape (a-d). The alternating joint configurations are (a) -M_1M_2-F_2F_1-M_1M_2-, (b) -M_1M_2-F_2F_1-M_1M_2-, (c) -M_1M_2-F_2F_1-M_1M_2-, (e) -F_1F_1-M_1M_2-F_2F_2-, (f) -M_1F_2-M_2F_1-M_1F_2- and (g) -F_1F_1-M_1M_2-F_2F_2-, where in this case, F-MM-F, M-FF-M, M-FM-F or F-MF-M represent a 2 DOF joint. This code is not applicable to (d) and (h), since they consist of one body without Male and Female parts. (Categorization adopted from Jelinek [40])**

.

Logically, one can generate more complex joints with 3 DOFs able to withstand tension. However, as stated earlier, rotation around Z is not primarily at interest, by having no immediate contribution to curvature. However, this third DOF can later be constrained by, for example, the addition of cables. Therefore, these 3DOF type of joints are briefly treated in Figure 3.4. The optional alternating solutions are again -FF-MM- and -FM-FM-, where in this case, F-M and M-F represents a 3DOF joint. Interestingly, these 3DOF joints can be split up in multiple 1DOF joints, similar to the 2DOF joints of Jelinek *et al.* [40]. However, this broader categorization will not be worked out within this study.

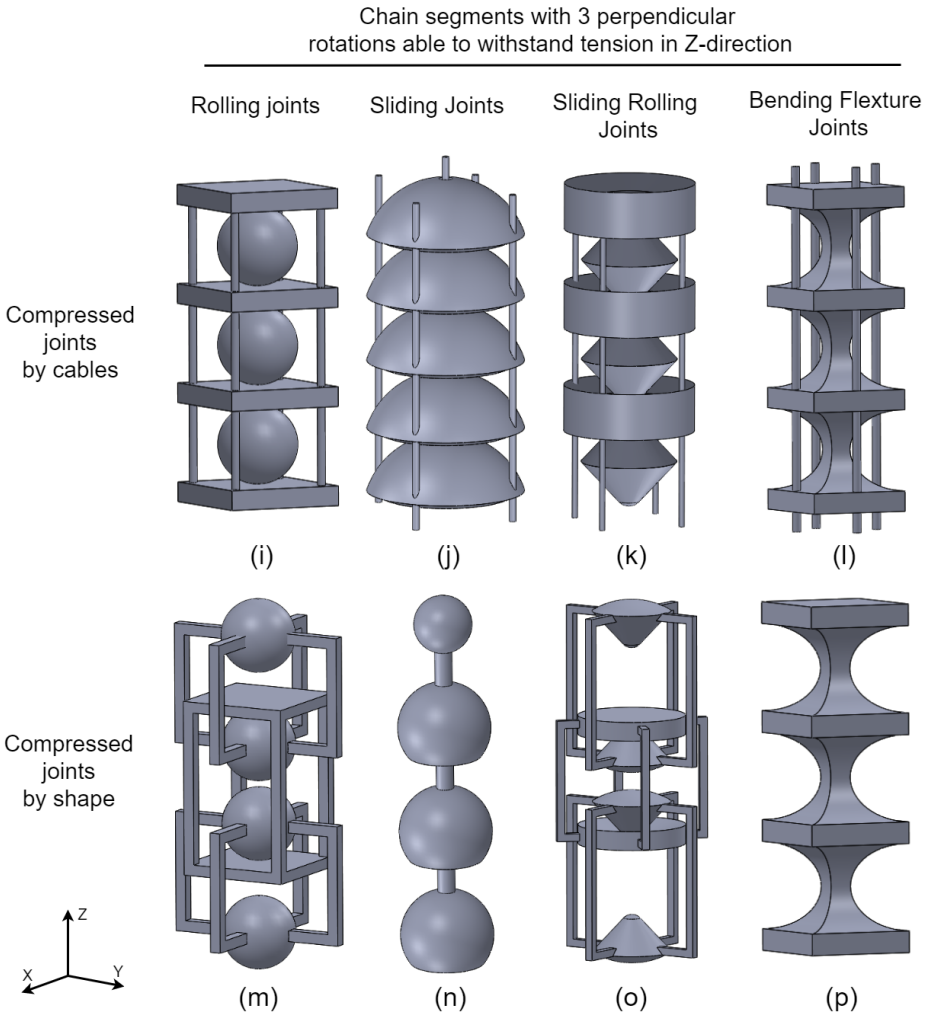

Figure 3.4: **Schematic overview of multiple chain segments in series comprising Rolling, Sliding, Sliding-Rolling and Bending Flexure Joints with 3 DOFs, compressed by cables (e-h) or shape (a-d). The alternating joint configurations are (a) -FF-MM-, (b) -FM-FM-, (c) -FF-MM-, (e) -FF-MM-, (f) -FM-FM- and (g) -FF-MM-. (Joint categorization adopted from Jelinek) [40])**

Due to the large amount of concepts for a subdesign, thorough concept selection is performed. First, the more internal DOFs that need to solidify, the more complex the system becomes. Regarding the main goal of this work, creating a planar (2D) everting growth-from-the-tip device will be sufficient for a proof of principle. Consequently, a qualitative selection is performed on segment concepts with planar joints, as visualized in the Appendix C. The selection comprises the following criteria:

- Feasibility for everting growth process
- Simplicity of the design
- Manufacturability
- Estimated load bearing capacity
- Ability to be downscaled

At first, feasibility for an everting growth process is based on the segment's robustness to differential loads (*e.g.* tension, compression, torque) and the controllability of the segment's motion, which is related to the amount of under constraints. For example, Sliding Rolling Joints (d,e,k,j) score low to this criterion, since the ratio sliding and rolling is unspecified, making the motion of segments less controllable. In contrast, sliding joints, especially constrained by shape,

have 1 point of rotation and are relatively robust to differential loads. Moreover, cables, which can only be loaded in tension, will be less robust to differential loads compared to shape locks.

Secondly, the large amount of required segments and the aim for a simple proof-of-principle require a high level of simplicity, specified in amount of parts per segment and the ease of pure rotation and locking incorporation. In general, the cable designs are more complex compared to shape designs, by allowing rotation but performing compression to hold the segments together, involving many length changes of cables between segments. One exception is the Bending Flexure Joint, which consists of one piece of material, which is automatically held together by shape (and cables).

Thirdly, manufacturability is mainly determined by the type of parts and assembly. For example, Bending Flexure Joints require accurate calculations with internal potential energy when bent, involving complex assembly. In contrast, sliding joints with shape lock can easily and accurately be laser-cut and assembled.

The criterion of load bearing capacity mainly focuses on lateral (X or Y direction) load during tension, compression and rotation. Concepts h,i,l and m have much play and will not likely bear high load if no large compression or tension force is applied. Similarly, cables are perpendicular to the load and can therefore only enlarge the normal force and thereby friction of the joint, involving relatively low load bearing capacity.

Finally, the ability to be down-scaled depends on the smallest dimension of parts and the type of assembly. Typically, Bending Flexure Joints score highest to this criterion, while rolling-sliding joints have relatively complex shapes and additional locking mechanisms.

In conclusion, Sliding Joints held together by shape perform best on these criteria. It is of no surprise that for these reasons caterpillars and bicycle chains that are driven by wheels or gears, use exactly the same type of joints.

3.3 Locking mechanism

Solidification of chain segments with respect to one-another in a reversible manner can be realized by shape, friction or magnetic locking. Rotational DOFs can be constrained by torque equal and opposed to the torque load. Here applies, shape locking occurs through any object exercising a counter torque through normal forces at contact points. In contrast, a counter torque generated by friction locking is exerted by shear forces, which depend on normal forces at contact points. Moreover, a magnetic lock can generate a counter torque without contact or it can generate a normal force as well. These constraining forces and torques can also be actively generated. However, active constraints (*e.g.* motors and actuators) are unnecessarily complex for this application.

Friction, shape and magnetic locking can be applied to different type of joints, as visualized by red arrows in Figure 3.5. However, the driving forces of rolling, sliding, sliding rolling and bending flexure joints differ. First, rolling implies zero slip, driven by a torque or forward force, which has to be countered when being locked. Furthermore, sliding joints have a constant point of rotation, by which it is only driven by a torque around that point. Logically, sliding rolling joints are driven by a combination of these forces and torques. Finally, bending flexure joints effectively rotate by pure torque. These driving forces are represented by blue arrows in Figure 3.5.

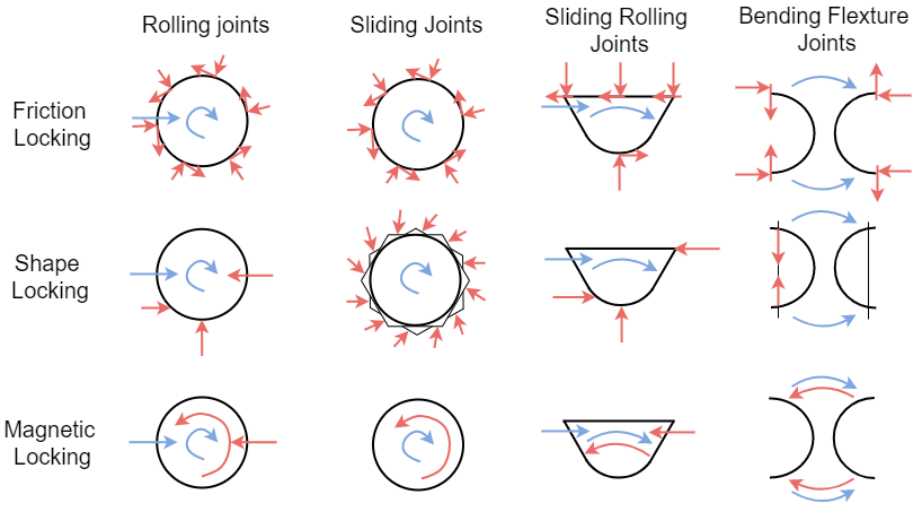

Figure 3.5: **Schematic force diagram of differential locking mechanisms and joints. The blue arrows represent the externally applied forces/torques and the red arrows represent the reaction forces/torques in order to be locked. Friction locking (a,b,c) is realized tangent to the contact area and shape locking (d,e) normal to the contact area.**

For a proof-of-principle, shape locking of the chosen sliding hinged joints will generate high load bearing capacity. In addition, shape locks are easy to manufacture.

3.4 Tip design

Given multiple chains incorporated with locking mechanisms, the tip should execute the following functions:

- Supply building material
- Drive eversion
- Lock chains or activate locking mechanisms
- Create curvature
- Reverse these growth actions

Driving such a system can be done by a forced material supply at the base (Figure 3.6 a), a forward force at the tip (Figure 3.6 b), a torque at the tip (Figure 3.6 c) or a combination of those.

The growth-from-the-tip principle implies a driving force that pushes the tip forward against the structure that it is being built, which in turn is supported by the base. However, the location of the system's drive and its reaction forces can be tuned. For example, a forward force at the tip can be generated by a flexible hose pushed at the base or by an elevated internal pressure. However, as the trajectory becomes more complex, driving such a system from the base will be much harder. Namely, the supplied chain should then also withstand compression forces in unlocked configuration, which would be unnecessarily complex.

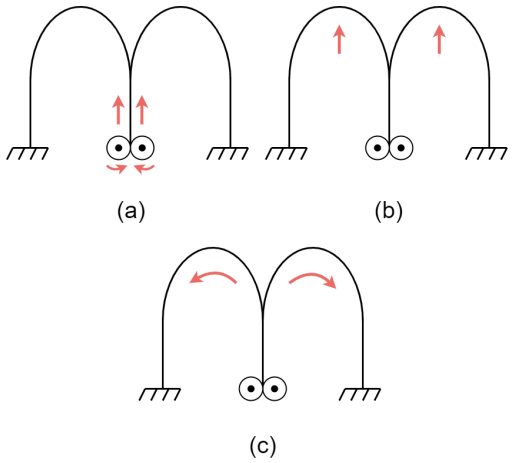

Figure 3.6: **Schematic overview of driving forces that generate eversion, with (a) pushed material supply, (b) pushed tip (by simple push or internal pressure) and (c) applied torque at the tip.**

Therefore, a drive system located at the tip with reaction forces acting on the built structure is

chosen. This tip-located drive can easily be reversed without requiring adaptations. Take for example the inverted tubes of Hawkes *et al.* [16], which are everting plastic bags driven by pressurized air. When the drive is simply reversed by creating under pressure and bringing the material in by tension, the system will probably cringe and deviate over the whole length. That does not mean reversing the system is not possible, but it is more challenging.

In conclusion, torque can easily be delivered by electric motors. Therefore, Concept C of Figure 3.6 is chosen.

Next, curvature creation can be driven by differential material supply, or by an additional torque exerted at the Center Of Rotation (COR). This principle, including reaction forces acting on the built structure, are visualized in Figure 3.7.

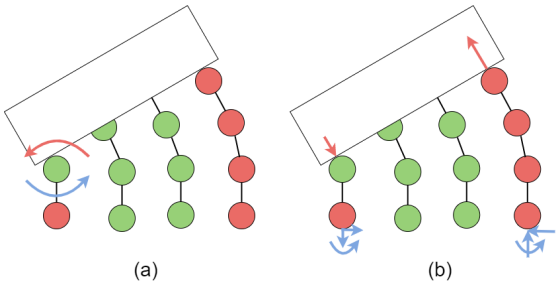

Figure 3.7: **Schematic overview of driving forces that can generate curvature, with (a) pure torque around the center of rotation and (b) a torque generated by differential material supply. Red and blue arrows represent forces acting on the tip and the reaction forces acting on the base of the structure, respectively. Note that some type of motor or actuator is driving the forces acting on the tip and its reaction forces on the structure. The red and green circles represent locked and unlocked joints respectively.**

Since rotation of the tip always requires a differential material output, curvature creation is driven by a differential material output. Given a torque drive located at the tip with planar sliding hinged joints and shape locks, a kinematic model is constituted. This model is based on several assumptions. Namely, the structure of locked chains is assumed to be rigid with zero deformation and deflection due to play. Moreover, the movement realized within one time-step is assumed to either be a pure rotation or a pure translation. In other words, rotations and translations of the tip are split up for simplicity.

Without slip, a rotation of α (radians) by the tip gear with radius (R) results in a translation of length (l) in accordance with:

$$l_L = R * \alpha_L \;\; and \;\; l_R = R * \alpha_R \tag{1}$$

Where the subscript L and R represent the Left and Right gear respectively. The difference in length output determines the angle of the tip. Namely, when the device of diameter D with two chains of width w are supplied with a differential material supply of length difference dl, the resulting angle of the tip (β) is:

$$\tan \beta/2 = \frac{dl}{2(D-w)} \tag{2}$$

where dl is defined as:

$$dl = l_L - l_R \tag{3}$$

It is worth noting that the input gear angle (α) is cumulative, eventually resulting in a cumulative tip angle (β). However, each (β) should be calculated separately, since equation 2 is based on a triangle. In contrast, if dl is constituted by two chain segments, a quadrangle emerges, consisting of two sequential triangles. Subsequently, the difference in output per time-step (ddl) is:

$$ddl = diff(l_L) - diff(l_R) \tag{4}$$

Hereby we can derive whether there is a curve to the right ($ddl(i) > 0$), a curve to the left ($ddl(i) < 0$) or a translation ($ddl(i) == 0$) per time step (i).

In addition, the Center Of Rotation has a constant position during rotation. Consequently, three main rules apply:

Left curvature:

R(i+1,:) = L(i,:) +

[(D-w)*cos($\beta(i+1)$) , $-(D-w) * sin(\beta(i+1))$]; (5)

$$L(i+1,:) = L(i,:); \tag{6}$$

So within this simplification, a curvature to the left involves constant left positions and right positions that rotate around the left coordinate.

Right curvature:

$$L(i+1,:) = R(i,:) +$$

[-(D-w)*cos($\beta(i+1)$) , $(D-w) * sin(\beta(i+1))$](7)

$$R(i+1,:) = R(i,:) \tag{8}$$

Here, the left coordinates can be constructed by rotation around the right coordinates, which remain constant over time.

Translation:

$$R(i+1,:) = R(i,:)+$$

[l*sin($\beta(i+1)$) , $l * cos(\beta(i+1))$]; (9)

$$L(i+1,:) = L(i,:)+$$

[l*sin($\beta(i+1)$) , $l * cos(\beta(i+1))$]; (10)

Finally, translations involve similar displacements per side directed towards the cumulative angle β.

The corresponding MATLAB script is added in Appendix H and a visualization of this simplified displacement can be found in Figure 3.8.

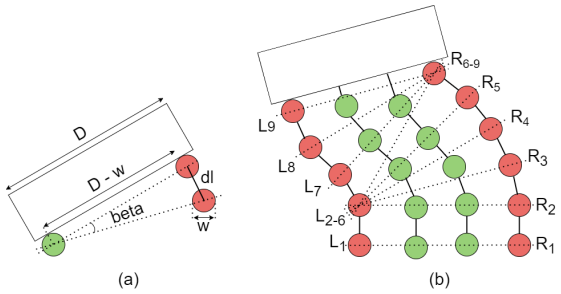

Figure 3.8: **Kinematics of everting chain with (a) a definition of tip diameter *D*, tip rotation *beta*, chain width *w* and length difference in material supply *dl* and (b) forward motion with multiple curves and Right (R) and Left (L) joint positions. The subscripts are related to a sequence in time. In this specific case, the system is translating (1-2) and curving left (3-6) and right (6-9).**

3.5 Prototyping proof of principle

In short, this work aims to present an innovative and everting type of growth-from-the-tip device inspired by Yan *et al.* [36] and Hawkes *et al.* [16]. To be serviceable and competitive with current devices, the device should be able to show reversible growth-from-the-tip with high load bearing capacity and limited interaction with the environment. The concept is a success when reversible growth-from-the-tip including curvature creation is realized. This type of propagation should only be driven by the application of pure torque at the tip in combination with the attachment of locking plates at the outer chain segments. On top of that, the chain should move smoothly through the tip and should not encounter internal obstacles at curves. Finally, shear and normal forces experienced by the environment should be a very small fraction of the applied torque.

To start, many type of driving systems, chain segments and locking systems are applicable. However, by striving for simplicity, a proof of concept can be achieved by planar movement, the removal of redundant components and a drive by hand. As a result, a male and female chain segment with planar sliding hinged joints (1DOF) and shape locking is worked out in Figure 3.9. The male segment has 27 equally distributed teeth per joint, which are used to lock the joint in variable positions. Since the beam of

the male segment will be blocked by the locking plate, around 13 differential locking positions are realized, comprising $360/30 * 13 = 156$ deg. The locking plates can be put in position from the top by hand.

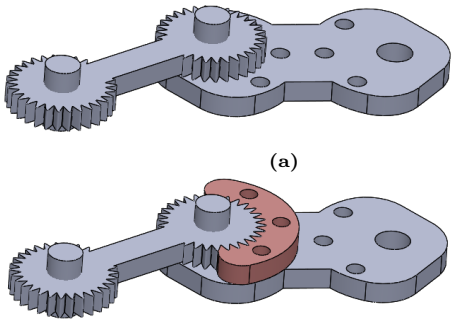

(a)

(b)

Figure 3.9: **Isometric view of chain segments in (a) unlocked configuration and (b) locked configuration by locking plate indicated in red.**

The torque-driven tip will comprise gears grabbing the chain segments and a sliding structure to keep the chain in place, as visualized in Figure 3.10. The distance between two chain axes is 42mm for male and female segments. Since the tip gears have 7 teeth, the circumference of the tip gear is exactly 7 times 42mm. All parts except for axes, are lasercut from 5mm thick PMMA plates. The hollow chain axes have an outer diameter of 7mm and are they are glued in place. The overall width of the device is 268mm.

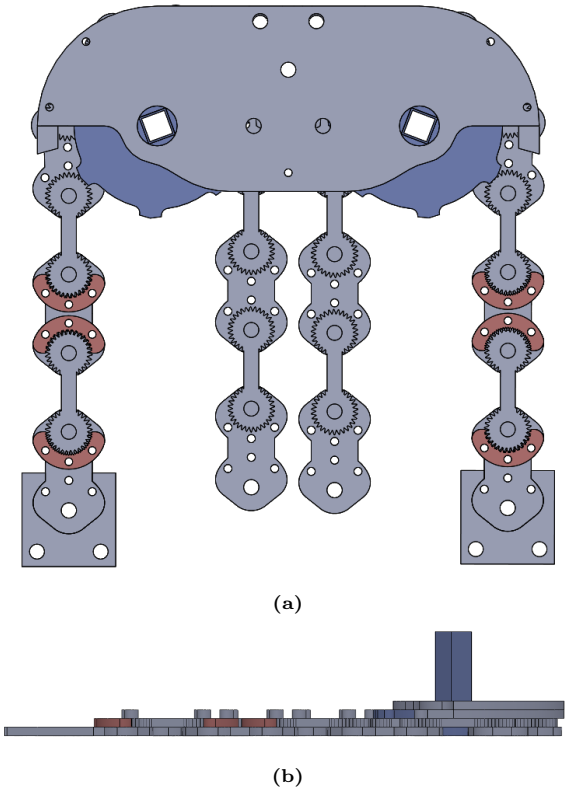

(a)

(b)

Figure 3.10: **Top view (a) and side view (b) of prototype I, color-coded by red and blue, representing locking plates and drive system respectively.**

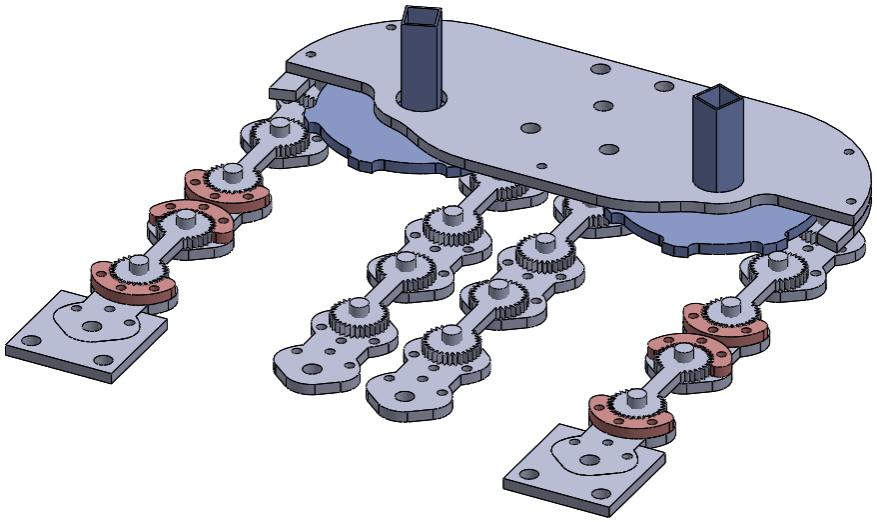

Figure 3.11: **Trimetric view of prototype I, color-coded by red and blue, representing locking plates and drive system respectively.**

4 Evaluation

4.1 Goal

Since Prototype I is a new type of concept, a relatively simple design will be sufficient to assess the working principle. Consequently, secondary design requirements are temporarily regarded out scope.

Given a locked outer chain with zero deformation and displacement, the tip gear should in theory show roll-out behavior. Moreover, two counter rotating roll-out mechanisms should counter undesired orthogonal forces. In addition, differential output material should result in curvature creation. Therefore, the following kinematic relation is key:

Counter rotation of the tip gears in combination with (un)locking outer chains should result in translation of the tip. In addition, differential rotation of the tip gears should result in rotation of the tip.

This relation will be evaluated by tracking movements of the planar device with a top view camera. These general observations and results can be found in the next section. Then, due to the key supporting function of the outer chain, load bearing capacity of locked chains is measured in Section 4.3. Moreover, interaction with the environment will be assessed in Section 4.4.

4.2 General observations and results

At first, Prototype I is evaluated on top of a smooth surface and recorded from the top by a video camera. As designed, the tip gears will be driven and the locking plates will be positioned by hand, while the tip position is tracked by a top view camera.

The everting chain principle is observed to work for translations of 8*42mm = 336mm (see Figure 4.1), single 90 degrees curvatures (see Figure 4.2) and two sequential 90 degrees curvatures.

A measurement of the ratio between tip gear rotation and translation of the tip is performed in Figure 4.3.

Regarding equation 1 (Chapter 3), angular displacement of $\alpha_1 = 38$ and $\alpha_2 = 40$ degrees with a gear radius of R = 46.67mm results in theoretical translations of T1 = 30.95mm and T2 = 32.58mm for the left and right chain respectively. In comparison, the measured translations were both 33.25mm, resulting in a difference of 4.5%.

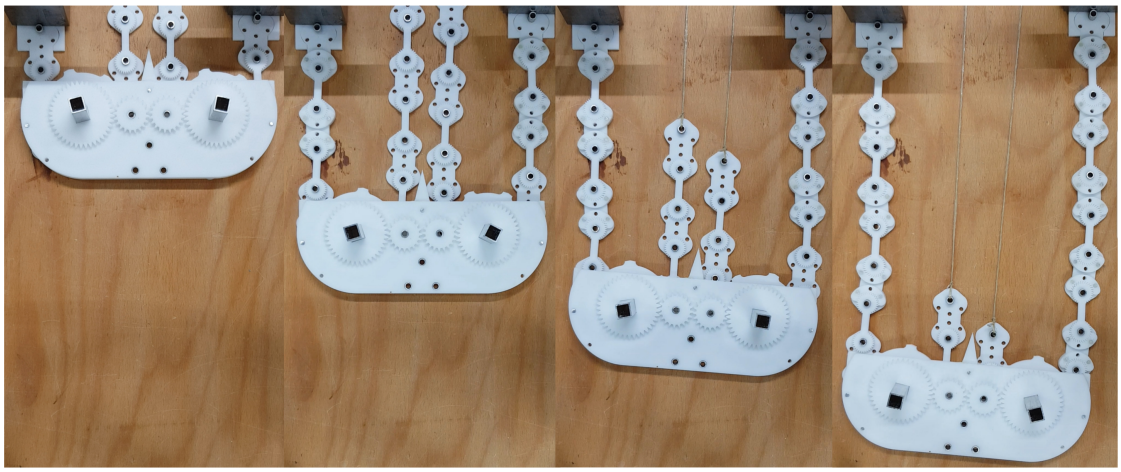

Figure 4.1: **Top view of straight growth-from-the-tip by Prototype I in chronological sequence (a) to (d).**

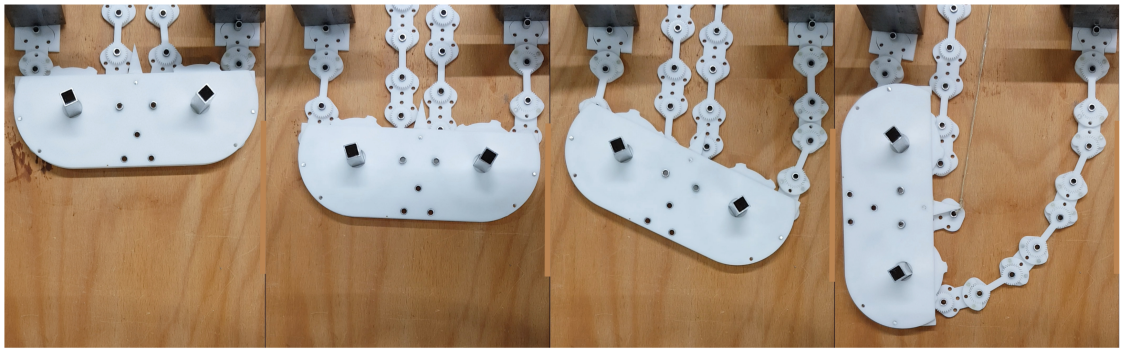

Figure 4.2: **Top view of curved growth-from-the-tip by Prototype I in chronological sequence (a) to (d).**

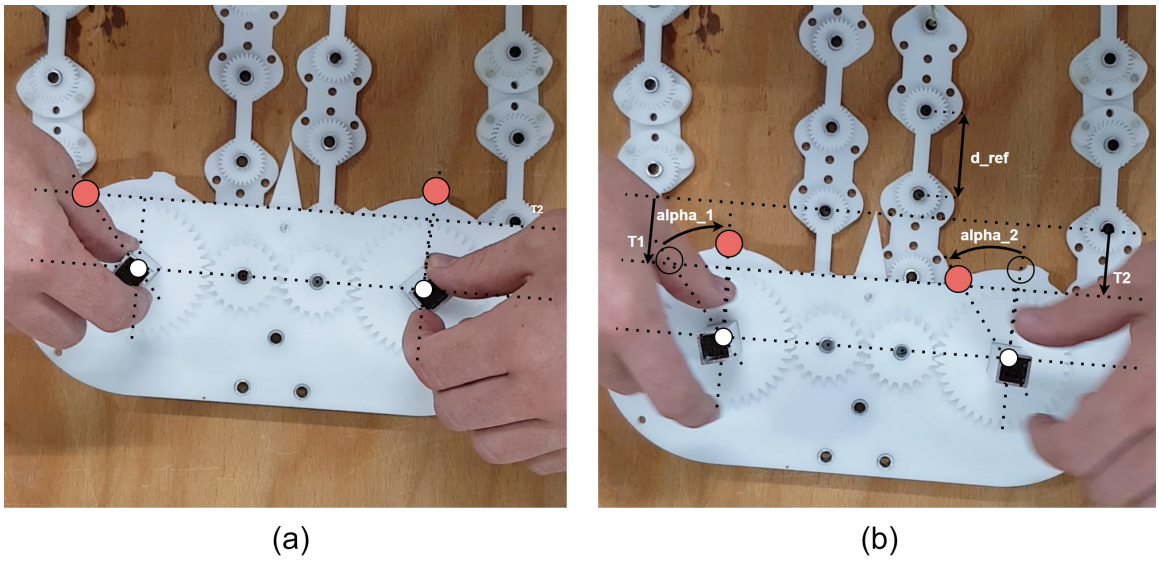

Figure 4.3: **Two sequential snapshots of prototype I from the top during forward and straight motion (a) and just after this motion (b). Rotation $alpha_1$ (= 38 deg.) and $alpha_2$ (= 40 deg.) resulted in Translation *T1* and *T2* respectively. In order to quantify the translations in the photo, we use reference distance d_ref = 42mm, resulting in T1 = T2 = 33.25mm.**

Other general observations are listed below:

- Equal reversed rotation of tip gears results in reversed translation of the tip.
- Differential reversed rotation of tip gears results in rotation of the tip.
- Each locked joint has 3 degrees play due to shape differences as a result of the cutting thickness of the laser cutter.
- Limited amount of locking positions (1 per 12 degrees), resulting in locking plates that are not easily put in place (360/30=12 degrees, max. +-6 degrees movement in order to lock).
- Smooth movement of chain through tip, no slip-stick movement occurs due to friction.

- Inner and outer chains get stuck sometimes with respect to one-another by their shape (can hook in each other). Consequently, the torque applied at the tip can bend the built structure.
- The locking plates can only be attached when the chain has left the tip, resulting in uncontrolled rotation just before locking.
- If the backwards path differs from the forward path, the chain can miss the tip-entrance after which it gets stuck.
- Recorded elongation rate is $(9 * 42mm)/4.07min = 92.9mm/min$, which can be much faster if locking mechanisms would have been automatic.
- Extension ratio: (extend-initial)/initial length = (475-131)/131 = 2.6.

Apart from these general observations, the locations of the chain axes can be compared to a kinematic model, as described in Chapter 3. By using reference distances, figure 4.4 shows the system's configuration after creating two curves of 90 degrees in series (red) with an overlay of the model (green).

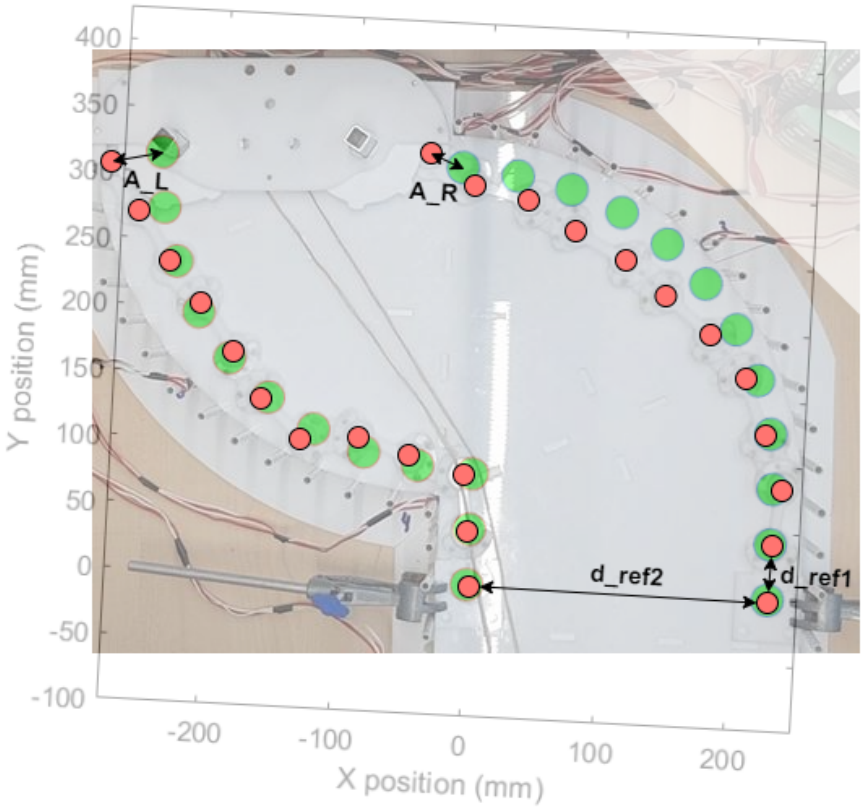

Figure 4.4: **Positions of chain axes of Prototype I as captured during the experiment (red dots) with a kinematic model overlay (green dots), using reference distances d_{ref1} and d_{ref2}. The absolute deviations for the left and right chain are indicated in A_L and A_R, respectively.**

The measured end-point-to-end-point deviation between the experiment and the model is 39mm and 27mm for the left and right chain respectively. With respect to the insertion length, the accuracy is 39/(11*42) = 8.4% and 27/(11*42) = 5.7%. This experiment is performed four times (n=4), resulting in accuracy data represented in table 5. The average deviation per insertion length is 8.1% and 6.2% for the left and right chain.

In addition, the experimental data (red dots) shows straight lines rather than smooth curves, as expected by the kinematic model (green dots).

	E.1	E.2	E.3	E.4
Left chain	8.33%	7.07%	8.37%	8.57%
Right chain	6.06%	7.58%	5.74%	5.45%

Table 5: **Results of 4 Experiments (E.) comprising the ratio of absolute deviation and insertion length per chain.**

4.3 Load bearing capacity

Within this experiment, the maximum load bearing capacity of 6 locked joints is evaluated. Both a male and female segment are placed horizontally with a locking plate attached, as shown in figure 4.5. The load is vertically applied at a distance of 84mm from the clamping and 42mm from the locked joint.

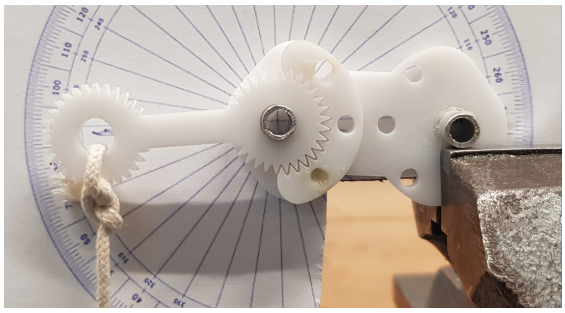

Figure 4.5: **Side view of load bearing measurement setup.**

A 360 degrees protractor is centered at the locked joint and the angular deformation is read-off at the load side. The load is gradually increased from zero to break-point. The results are visualized in figure 4.6.

On average, the samples deformed 1.6 degrees for an increased load of 1kg until the female segment broke. This breaking-point was reached at a deformation of 7 or 8 degrees and a load of 3.95-5.95kg. The resulting average torque load was 4.95kg*9.81m/s^2*0.042= 2.04N*m.

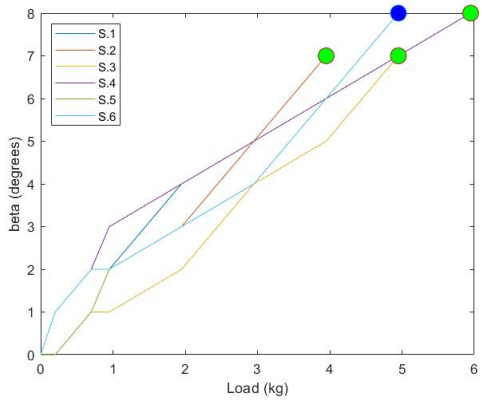

Figure 4.6: **Applied load (kg) with respect to corresponding angular deformation (beta) for 6 Samples (S). The blue and green dots contain 3 and 1 breaking-points respectively.**

4.4 Interaction with environment

Interaction with the environment can be measured in terms of normal and shear forces while moving through a trajectory. Namely, the deformation of force transducers, like hollow tubes, can be measured with strain gauges. By calibrating and calculating this force-deformation relation, forces acting on the environment can be evaluated. It is worth noting that this calibration was linear and performed in one particular direction.

Within this experiment, hollow tubes are placed along a path that comprises two 90 degrees curves in series. Forward and backwards movement along this trajectory will be performed 7 times. A schematic overview of the corresponding measurement can be found in Figure 4.7.

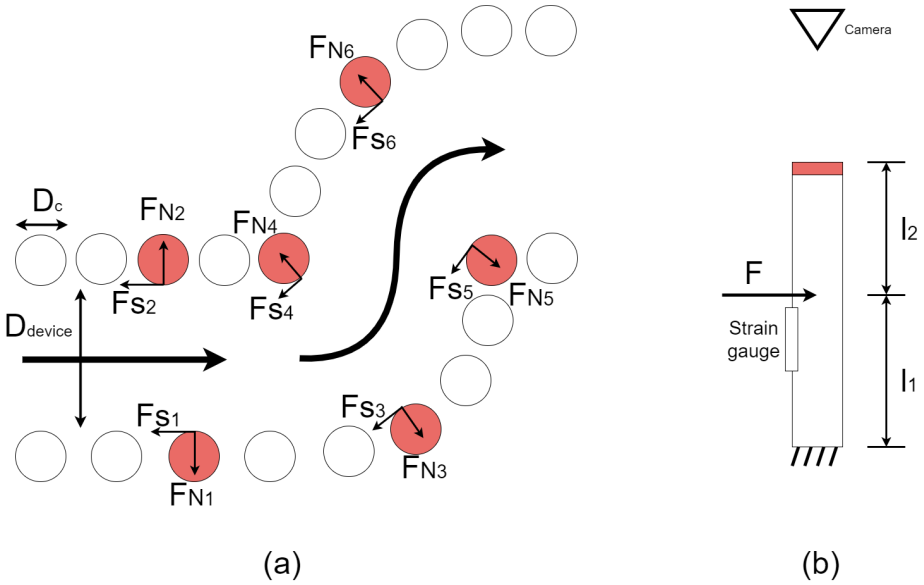

Figure 4.7: **Schematic overview of measurement setup, with (a) top view of measurement setup, including Normal Forces (F_N) and Shear Forces (F_s), Diameter of the device (D_device) and Diameter of the cylinder (D_c) and (b) side view of a cylinder.**

The stress-strain relations of the hollow tubes are briefly summarized below and incorporated in the MATLAB model found in Appendix G.

The hollow tubes are clamped into a ground plate and loaded by a force F at length l_1 from the clamping, as visualized in Figure 4.8.

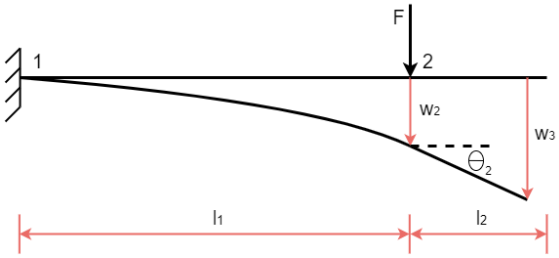

Figure 4.8: **Schematic overview of a beam under load (F), with corresponding delfection (w_2) and deflection angle θ_2. Deflection w_3 is amplified by length l_2.**

A relation between deflection angle θ_2 and this load is given in equation 11.

$$\theta_2 = \frac{Fl_1^2}{2EI} \tag{11}$$

where E the Young's modulus and I the bending moment of Inertia. The bending moment of inertia of a hollow cylinder is in turn:

$$I_x = I_y = \frac{\pi}{4}(R^4 - r^4) \tag{12}$$

,with outer radius R and inner radius r. The vertical deflection at point 2 is approximated by:

$$w_2 = \frac{Fl_1^3}{3EI} \tag{13}$$

and the vertical deflection is just a linear extrapolation of point 2 by using w_2 and θ_2.

$$w_3 = w_2 + l_2 \tan\theta_2 \tag{14}$$

By plotting these equations in Figure 4.9 by MATLAB script 3 in Appendix I, the optimal tube dimensions can be derived iteratively. Both PVC and PMMA are investigated by their low Young's Modulus and price. The eventual tubes are designed according to a minimal outer diameter of 5mm (required for the strain gauges) and a deflection of around 0.01m at a load of 40N.

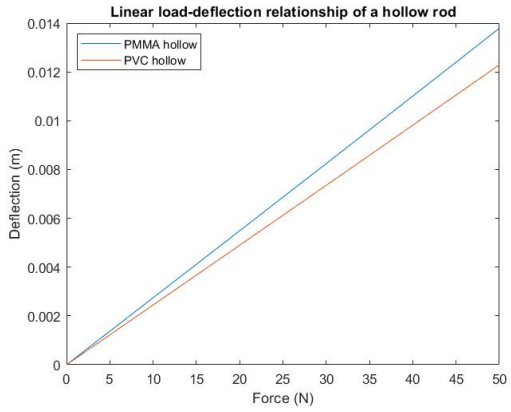

Figure 4.9: **Load-deflection relationship for a hollow rod with Radius (r = 2.5mm, R = 3.5mm) and length (l1 = 40mm, l2 = 60mm) with PVC (E = 3.25GPa) and PMMA (E = 2.9GPa).**

After conducting 7 experiments, one intermediate conclusion can be drawn. The human operator distorts the measurements considerably, by driving the system and attaching the locking plates, which, most often, do not fit unless the chains are slightly rotated. As a result, one experiment (Experiment 6) with the least human interventions will be briefly analyzed. Normal force measurements over time by 4 sensors along the trajectory of Experiment 6 can be found in Appendix D.

In addition, force peaks detected by the strain gauges can be linked to movements on video by time. By assessing movements made on video, the corresponding force peaks can be identified. A classification of the type of distortions in combination with the corresponding relative frequency is stated below. Within this experiment, 32 peaks are visually analyzed, resulting in the following distribution:

- Driving the tip gears
  - Directly (50.0%)
  - Indirectly (via structure, 3.1%)
- Attaching/detaching locking plates
  - Directly (25.0%)
  - Indirectly (via structure, 15.6%)
- Chain got stuck (3.1%)
- Tensed wire touches sensor (3.1%)

It is worth noting that peaks 3-21, 23-25 and 28-31 of sensor 6 are disregarded because no touch is observed via camera. However, the elevated ground plate touches the force transducers, thereby indicating an indirect and undesired load via the measurement setup.

Furthermore, the highest measured distortion is 4N (and 2N for Experiment 6). Interestingly, the 5 indirect distortions are maximally 0.36N. Working with variable and unknown input forces, this value gives at least a sense of the magnitude of normal forces acting on the environment.

Shear forces could have been measured if the force transducers were rotated by 90 degrees. This is not executed due to the intermediate conclusion of this experiment.

5 Improved Design

5.1 General abstraction

Even though Prototype I performed reversible growth-from-the-tip with multiple angles in series, large distortions of the human operator were detected. On top of that, shape locking resulted in a limiting amount of locking positions and relatively large play in locked position. Finally, the shape of the chain segments resulted in an obstructed material supply. Therefore, the second prototype should incorporate the following changes:

- A system drive without physical distortion of a human operator.
- Locking mechanisms without physical distortion of a human operator.
- Friction locking instead of shape locking.
- Low-friction side of the chains that cannot hook into each-other.

Note that the main design requirements remain unchanged. For example, the load bearing capacity of a friction-locked chain still needs to be sufficient.

5.2 Chain design

First, (hinged) sliding joints will be incorporated again, by their practical feasibility, simplicity, manufacturability, load bearing capacity and ability to be down-scaled. In addition, the sliding hinged joints need to incorporate a friction-locking system, that prevents rotation in locked configuration. This locking system is designed according to the following criteria:

- Large rotational friction in locked configuration
- Low rotational friction in unlocked configuration
- Low power required during locking
- Locking mechanism is driven by the main system drive
- Low amount of parts
- Easy to manufacture
- Small-sized

A bi-stable drum brake fits these criteria. An overview of the resulting chain design is visualized in Figure 5.1, with male and female segments. The 3D printed and lasercut version is shown in Figure 5.2.

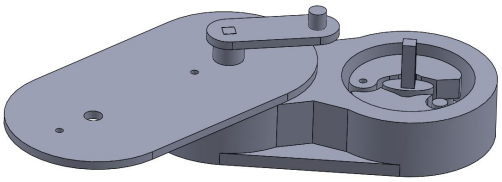

Figure 5.1: **Isometric view of new chain design, incorporating bi-stable drum brakes**

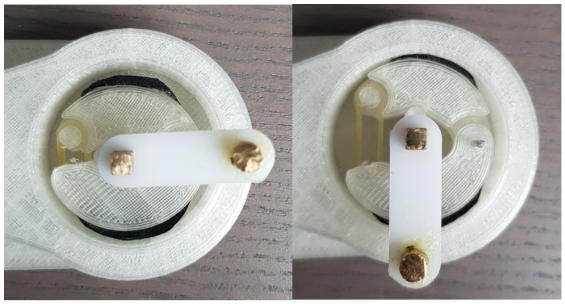

Figure 5.2: **Top view of locking mechanism of prototype II in (a) unlocked and (b) locked configuration. Note that the top plates are removed for visibility.**

Regarding the bi-stable drum brake, the compliant rubber layers contain potential energy when deformed. Deformation is zero in the unlocked configuration and medium in locked configuration. During the 90 degrees rotation of the crank, deformation of the rubber will be larger. Consequently, the locked and unlocked configuration are the two positions of the crank with the lowest potential energy, resulting in bi-stability. This also means that the crank can be accelerated from a high to a low potential energy state, or *vice versa*. The force required to turn the crack 1 degree does not only differ with respect to the

deformation of the rubber and the overall energy state of the crank, dimensional variations also play their part.

5.3 Tip Design

Within this prototype, two electric drives consisting of *NEMA 17* (1.8°, 2-phase, double length (40mm) and maximum input current of 1.5A) stepper motors are incorporated. Consequently, the electric drive delivers exact rotations, required for accurate movements. This electric drive does not only supply the chain and push the tip forward, it is also designed to drive the locking mechanisms. The latter is best visualized in Figure 5.3.

In order to lock the chains, each crank has to rotate by 90 degrees. However, by the presence of male and female segments, multiple crank positions occur. More specifically, a crank is always positioned to the front of the chain axis in unlocked configuration. Consequently, the crank tip is either above (yellow) the male segment or in front (green), as indicated in Figure 5.4. These positions are generated by a MATLAB model that can be found in the Appendix J. When the chain is leaving the tip, the crank needs to rotate 90 degrees in order to lock. This desired position is also different for the front cranks (red) and the rear cranks (purple).

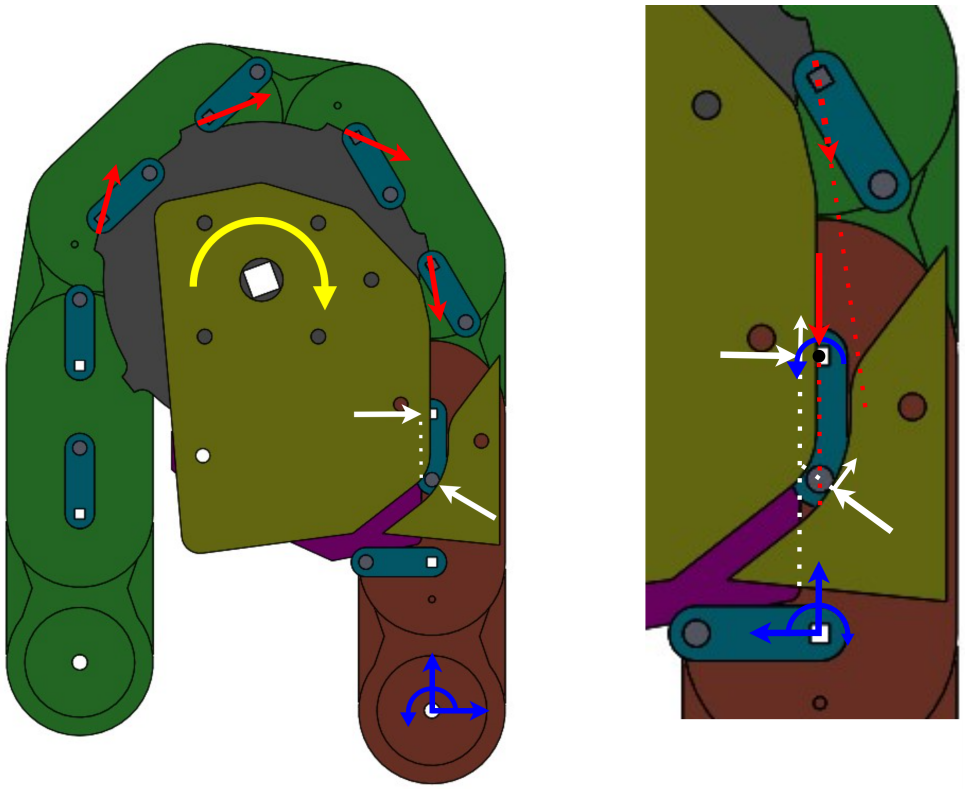

(a) (b)

Figure 5.3: **Top view and schematic representation of mechanical locking system of prototype II, with color-coded arrows: torque generated by stepper motor (yellow), the effective forces on the chain driven by the motor (red), normal and shear forces of tip structure onto chain (white) and forces generated by locking mechanism (blue). Moreover, the unlocked chain segments are indicated in green, while the locked chain segments are indicated in red. Note that the chains are also held in place while rotating with the gear (grey) by a circumferential plate that is not indicated.**

The differential positions of a front and a rear crank require two different tracks to lock. However, if the track is straightened for at least the length of one chain segment, the rear and front crank positions coincide and only 1 path is required to lock.

Accordingly, the lower axis is grabbed by the gear (indicated in grey) and taken over by straight plate indicated in purple in figure 5.3. This straight plate allows for translation in axial direction of the device, while it prevents movement in orthogonal direction. Consequently, undesired moments on the cranks while locking are diminished. The takeover of the chain guide (pink) from the tip gear (grey) is forced by the crank, which is always in front of the chain axis. As a result, the crank translates before the chain axis, thereby pulling the axis in the right direction. Each layer of the tip differs and grabs another point of each crank. Therefore, an isometric view of the design is given in Figure 5.5.

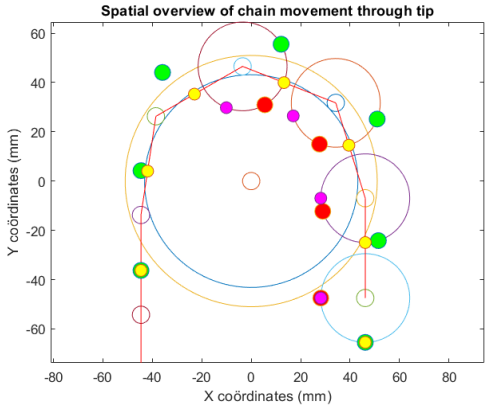

Figure 5.4: **Crank positions while moving around the gear, where the green and yellow dots represent the unlocked configuration of the front and rear cranks respectively. The desired locked configurations are indicated in red and purple for the front and rear cranks respectively. Note that the front and rear cranks coincide when at least 1 chain segment has moved out straight.**

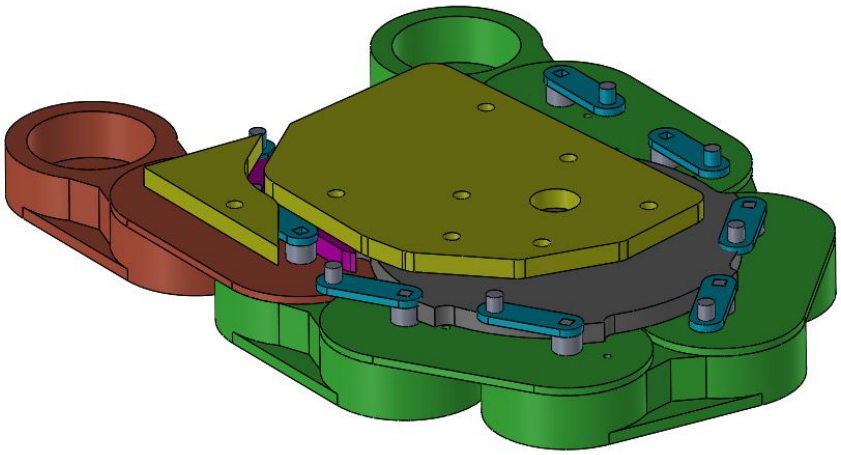

Figure 5.5: **Isometric view of tip design, visualizing forced rotation of the locking crank.**

The two NEMA 17 stepper motors are controlled by *DRV8825* motor drivers and an *Arduino Uno Rev 3* development board. The motor drivers are powered by the 5V pin of the arduino and an adapter with an output of 12V and 1.25A (direct current). A schematic visualization of this electronic setup can be found in appendix E. An overview of the total system including the stepper motors is given in Figure 5.6. After manufacturing, assembly and electronic adjustments, the prototype looked like Figure 5.7.

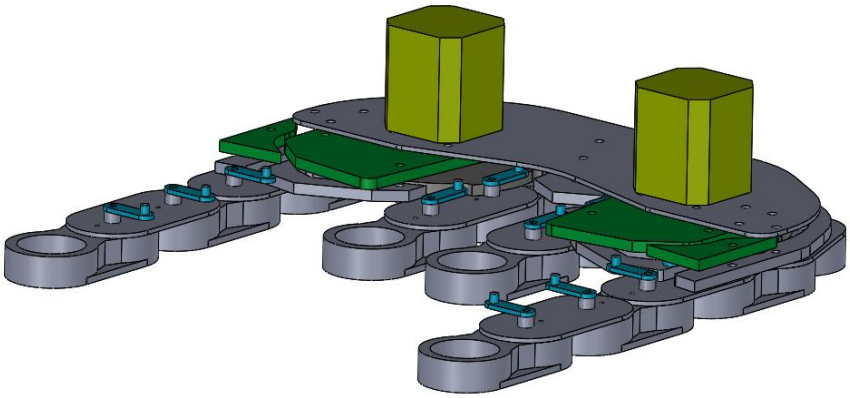

Figure 5.6: **Isometric view of total design, with NEMA 17 stepper motors (yellow), locking cranks (blue) and the crank guide (green).**

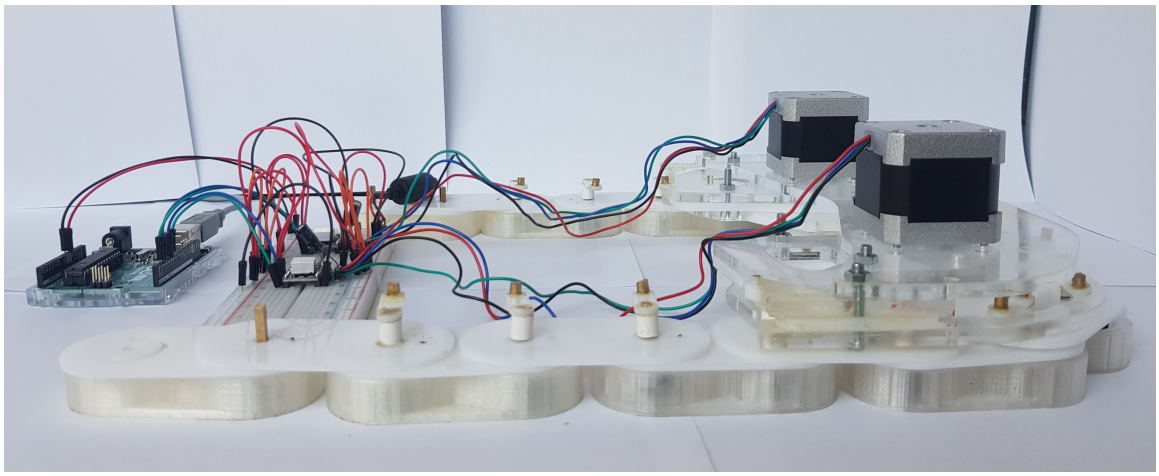

Figure 5.7: **Side view of prototype 2 with stepper motor control.**

6 Second Evaluation

6.1 Movement of total system

As described earlier, the prototype works kinematically when

- The application of equal and sufficiently large counter torque (*i.e.* large enough to rotate the tip gears) results in translation of the tip.
- Differential rotation of the two tip gears results in a curved movement of the tip
- Both functions are fully reversible by only reversing gear rotation.

In addition, forward motion of the tip would also imply that the locking mechanisms generate sufficient support to move the tip forward.

To start validating, a reference measurement is performed, comprising prototype II with non-activated locking mechanisms. The outer chains are not clamped. The corresponding displacements are tracked by video, as visualized in Figure 6.1.

The first obvious result is the fact that the chains buckle. Moreover, the chains run smoothly through the tip and the stepper motors do not slip.

Looking at the displacements between snapshots, the midpoint of the tip moves 18.3mm backwards during t = 0-21 sec, after which it slightly moves forward by 3.1mm during t = 21-74 sec.

An interesting observation that is related to this forward an backward motion, is the following:

- At t = 0 - 21 sec, the amount of input/inner chains > the amount of output/outer chains
- At t = 22, the amount of input/inner chains = the amount of output/outer chains
- At t = 23 - 80 sec, the amount of input/inner chains < the amount of output/outer chains

Combining these results, the tip moves forward when the friction generated by the input material is lower than the friction generated by the output material.

After this experiment, the locking mechanisms within the chain are activated.

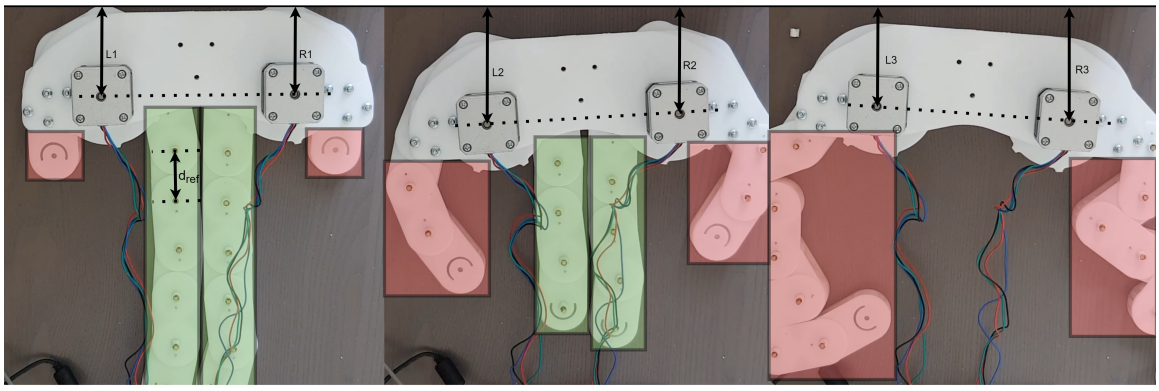

Figure 6.1: **Three sequential snapshots (t = 0 sec, t = 21 sec and t = 74 sec) taken from video comprising a demonstration of prototype II with electric drive and without the locking mechanisms being activated. The reference distance is known (*dref* = 40.5mm), resulting in distances *L1* = 70.9mm, *R1* = 69.3mm, *L2* = 92.7mm, *R2* = 84.1mm, *L3* = 79.4mm and *R3* = 91.1mm. The green and red boxes represent areas where input and output material generates friction, respectively.**

However, the prototype did not run smoothly. By pulling the chain through the tip, several observations were done:

- Handmade cranks had too much friction while moving through the tip
  - By an inaccurate height
  - By superfluous glue
  - By play of the chain axes

Moreover, the detent torque (1.5N*cm) of the NEMA 17 stepper motors was lower than expected, being powered by 0.625A and instead of 1.5A. Consequently, the stepper motors skipped steps and the input rotation (*i.e.* rotation entered in Arduino) was not similar to the output rotation of the tip gears. However, by focusing on the eventual movement made by the prototype, the internal slip of the motor can be regarded out-scope.

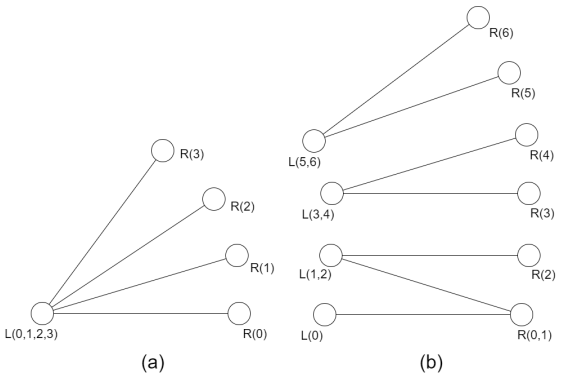

Figure 6.2: **Kinematic simplification of (a) pure leftward curvature and (b) a combination of curvatures and translations made by Prototype II.**

Three cases are treated, namely a pure rotation, a combination of curvatures and translations and reversed movement. The first two movements are kinematically simplified in Figure 6.2. This kinematic simplification is entered in the MATLAB model, resulting in expected locations of the chain axes. By using reference distances, the model output is placed on top of a snapshot of the experiment with a certain transparency. The above-mentioned cases are visualized in Figure 6.3 and 6.4.

Regarding the furthest points, the measured point-to-point distance between the experiment and the model is 4.8mm for the right chain, which is $4.8/(4 * 40.5) = 2.9\%$ deviation with respect to the insertion length. Pure rotation around a Center Of Rotation (COR) with a constant radius (R = 230mm) and a straight distance of 40.5 mm between two points, theoretically results in an angular displacement of 10.4 degrees between these two points. However, in reality the intermediate angles between chain segments differ by 0.2 degrees from this mathematical model. Namely, the total tip rotation was 42.5 deg, which differs $(42.5\,\text{deg} - 10.4\,\text{deg} * 4)/(10.4\,\text{deg} * 4) = 2.2\%$ of the theoretical movement. Note that this curvature experiment is performed just once (n=1). In line with this observation, small deformations of locked chains and a slightly moving COR were detected.

For the second case, the measured point-to-point distance between the experiment and the model is 46.3mm and 13.0mm for the right and left chain respectively. This results in $46.3/(6 * 40.5) = 19.1\%$ and $13.0/(3 * 40.5) = 10.7\%$ deviation per insertion length for the right and left chain respectively. Note that two chain segments buckled due to non-activated locking mechanisms. So if the prototype worked as designed, deviations could have been much lower.

The third case comprised reversed movement of the prototype. At both sides, two sequential locking mechanisms were brought in and unlocked, as visualized in Figure 6.5. When the left side brought in more material, the tip rotated around a right COR and *vice versa.* By converting the measured maximum deformation distance (d_{max}) via a reference distance (d_{ref}), the real d_{max} is 9.1mm.

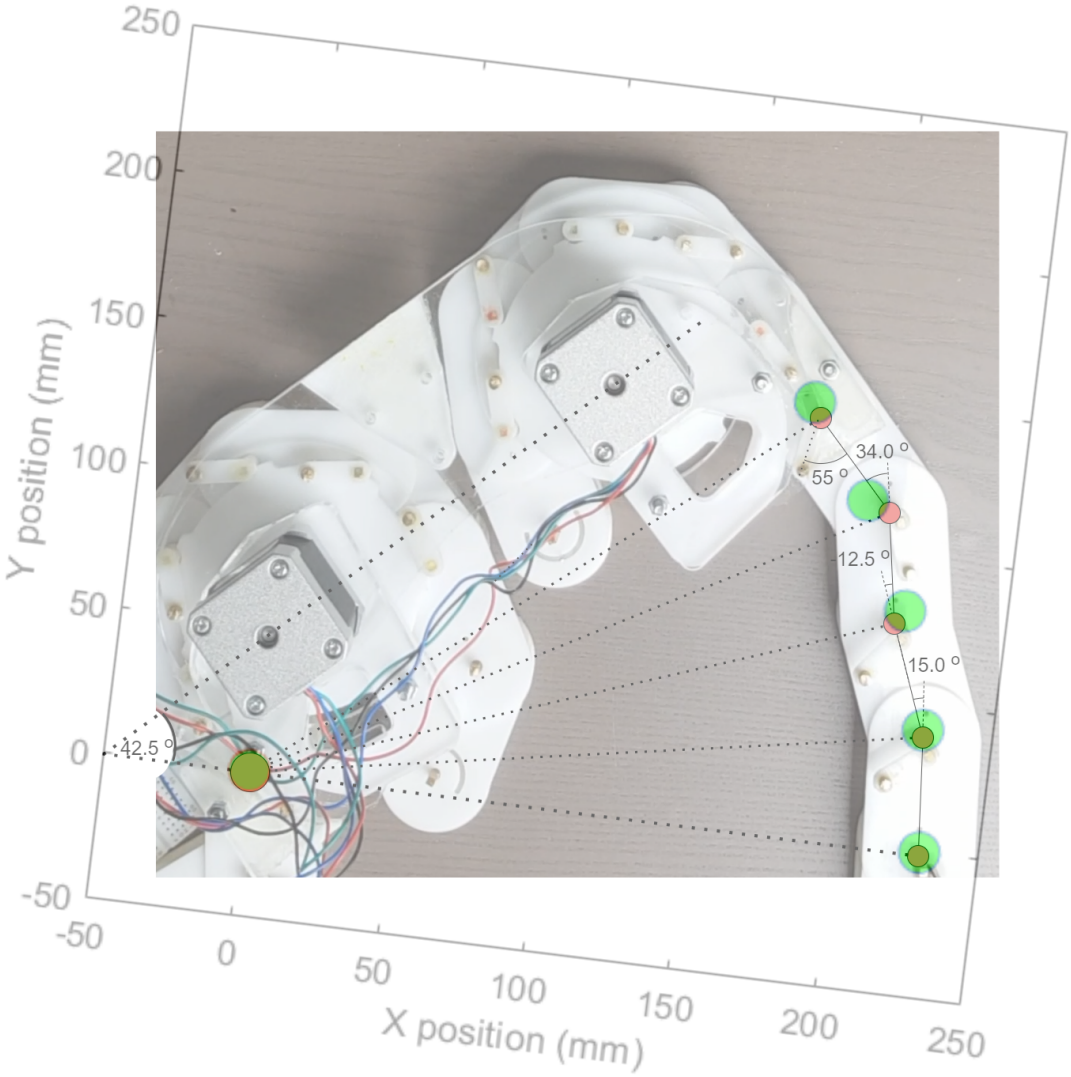

Figure 6.3: **Top view of prototype II performing a curvature to the left. The red dots represent the observed positions of chain axes, while the green dots represent the theoretical positions generated by a simplified MATLAB model.**

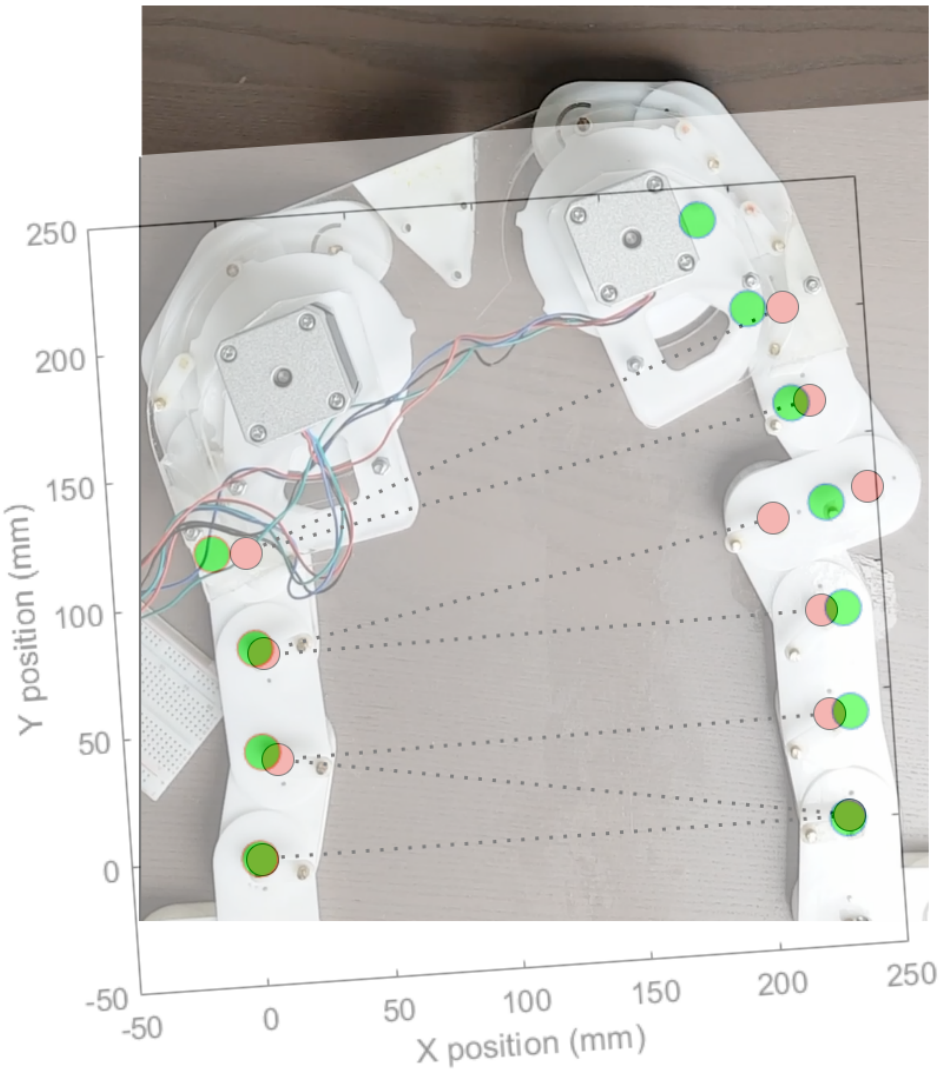

Figure 6.4: **Top view of prototype II performing straight movements and curvatures with an overlay of the MATLAB model. The red dots represent the observed positions of chain axes, while the green dots represent the theoretical positions generated by a simplified MATLAB model. Obviously, the right chain buckles resulting in most of the deviation at the end point.**

Including slippage and buckling, the tip of prototype II moved 182mm forward on average in 130 seconds, leading to an elongation rate of 84.1mm/min. By purely looking at a successful rotation (*i.e.* disregarding undesired slip and buckling), prototype II propagates 1.30mm in 0.5 seconds, resulting in observed intervals with an elongation rate of 156mm/min. It is worth noting that the steppers are programmed with low speed and several delays (2 seconds every rotation of 10 degrees), meaning that the potential elongation rate is even higher.

Last, the initial structure + tip length is 155mm, while the eventual recorded length was 295mm, resulting in an extension ratio of (295-155)/155 = 0.9.

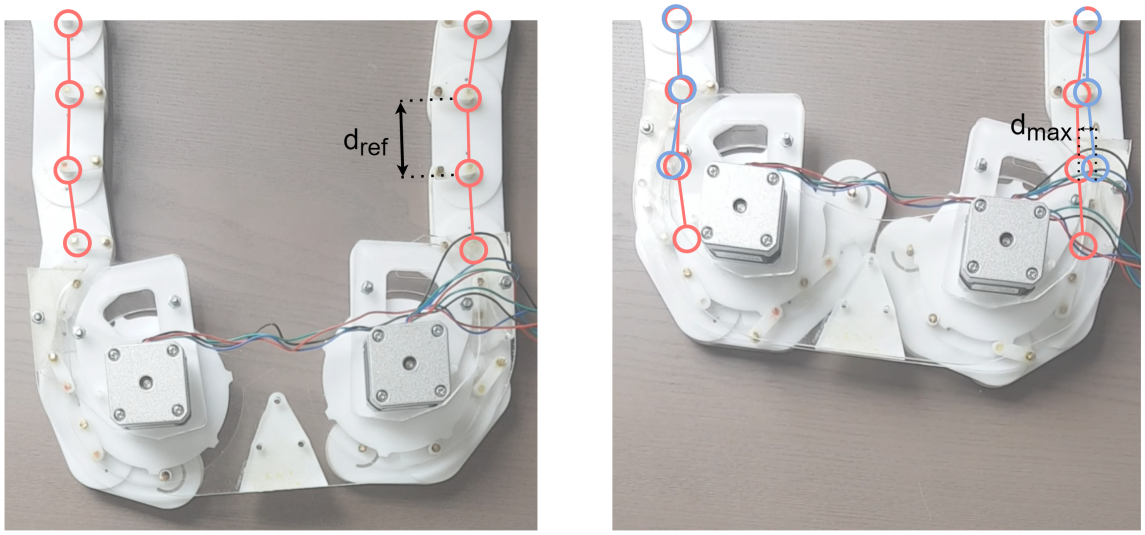

Figure 6.5: **Two snapshots of reversed growth experiment with d_max = 9.1mm and d_ref = 40.5mm.**

6.2 Angular movement of locking crank

In order to quantify the movements and play of the locking mechanism, the angular position of the locking crank is measured by a printed 360 degrees protractor. By measuring 15 different locking mechanisms, the average rotation to lock is 91.7 degrees. The crank in locked and unlocked position has 6.5 and 6.8 degrees play on average, respectively. The peak potential energy, which is an unstable equilibrium point, is measured at 61 to 68 degrees. The measurement results can be found in Appendix F.

6.3 Load bearing capacity of locked chain

This experiment aims to quantify the torque generated by the friction lock (T_{lock}) and the angular displacement (β) of multiple locking mechanisms. By imposing weight in several steps and by applying some compensation factors, the input force (F_{load}) is known. The angular displacement (β) is detected by a camera from above and read-off afterwards. The angle between x-axis and the wire connecting the imposed load with the chain axis with length (l_{wire}) is defined as α.

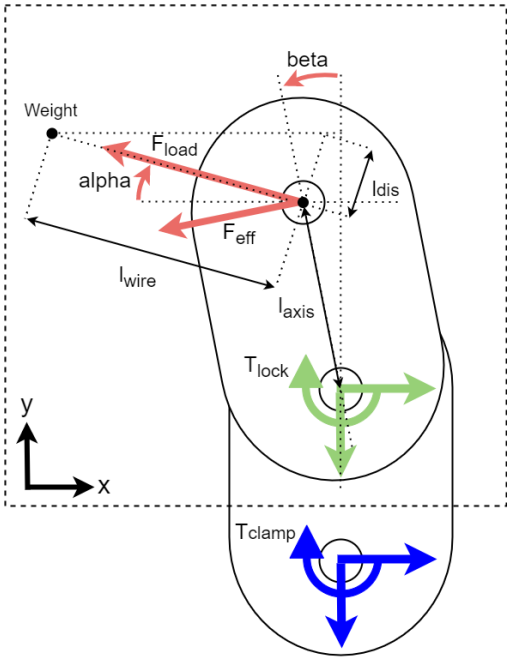

Figure 6.6: **Schematic overview of load bearing measurement setup, with the imposed load (F_{load}), efficient load (F_{eff}), wire length (l_{wire}), perpendicular displacement (l_{dis}), an axis-to-axis distance of (l_{axis}), angle between x-axis and wire (α) and an angular displacement during deformation or rotation (β). Finally, the resulting locking torque (T_{lock}) and clamping torque (T_{clamp}) can be calculated.**

At first, the imposed load is not exactly perpendicular to the axial orientation of the chain. Consequently, a simple correction will compensate this effect:

$$F_{eff} = F_{load} * \cos(\alpha + \beta) \tag{15}$$

It is worth noting that l_{wire} is relatively large with respect to the maximum perpendicular displacement due to deformation and rotation of the locked mechanism ($l_{wire} >> dl_{dis}$). Therefore, α is assumed to be constant during deformation. Consequently, a load-deformation diagram in chronological sequence can be generated in MATLAB (Appendix K), as visualized in Figure 6.7.

As expected, the angular deviation is caused by both deformation of rubber and undesired slippage resulting in 'plastic' rotation. Slipping can best be seen by the horizontal lines in Figure 6.7. Moreover, the fact that full unloading does not result in zero angular displacements tells us that indeed, irreversible rotation has taken place. If we accept an angular displacement of 25 degrees, the maximum perpendicular (*i.e.* effective) load varies from 1.6 to 17.0 Newton and on average 7.3N.

Quantifying the ratio of angular displacement due to slip and both slip and deformation can be done by dividing the angular displacement due to unloading (from 2050 to 0 grams) by the total displacement due to loading. On average, the irreversible slip contribution was 78% after bearing a load of 2050 grams.

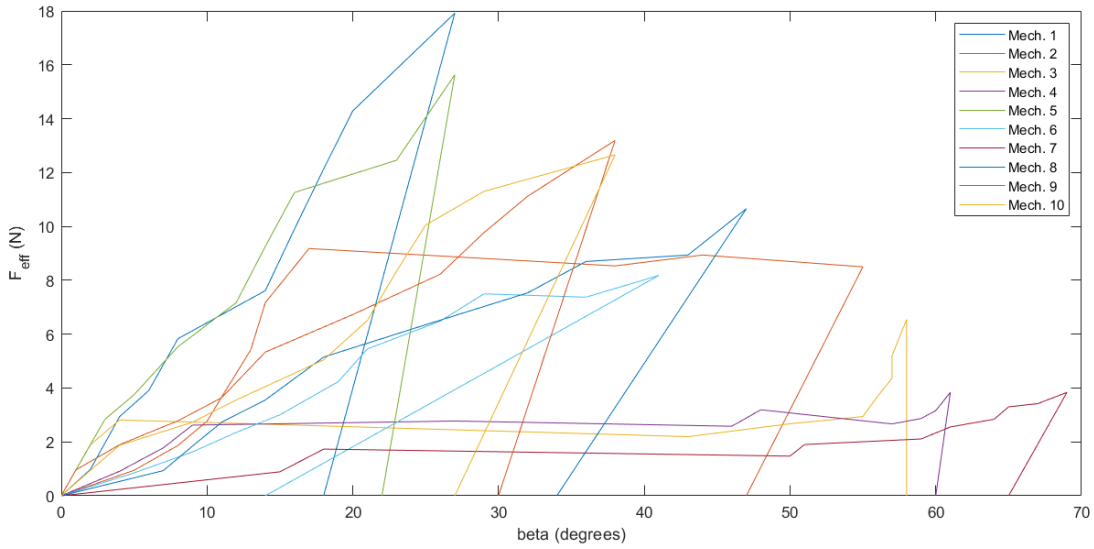

Figure 6.7: **The effective load (F_{load}) over angular deviation (β) in chronological order (in positive x direction) of 10 locking mechanisms.**

7 Discussion

7.1 Main findings

In this thesis, growth-from-the-tip is simplified to three main functions, as described by Yan *et al.* [36], namely: 1. Some sort of fluidized material is transported to the tip, 2. The input material is transformed at the tip into a solidified support structure and 3. The tip pushes itself forward on top of this structure. This generalization involves a broad set of growth-from-the-tip concepts.

The everting chain principle is selected after a thorough evaluation of 8 concepts. The evaluation focused on reversibility and the ability to create multiple active curves in series. Additional advantages for this concept comprise limited interaction with the environment, curvature around sharp edges, high load bearing capacity and no additional system is required to create curvature.

To validate the evering chain principle, the rotations made by the tip gears and the positions and (re)orientations of the tip are tracked by camera and compared to a kinematic model. The everting chains prototype is judged to work when equal counter rotation (*i.e.* inside-out or outside-in) of the tip gears results in a translation of the tip, while differential rotation results in rotation of the tip. Both prototypes perform this principle.

7.1.1 Prototype I

Prototype I was able to perform two 90 degrees curvatures in series with deviations per insertion length of 8.4% and 6.2% for the left and right chain respectively. As a result, prototype I meets the accuracy design requirement. Deviations from the modelled path are measured by absolute point-to-point distances instead of perpendicular distances to a path. Namely perpendicular deviation also results in an axial deviation, since less material is available to move forward.

For straight movements the supporting outer structure was not observed to deform considerably. However, at double curvature, the outer chains seemed to be straightened. Since the width of the device is constant, this deformation and displacement (due to 3 degrees play per joint) took place after locking. This deviation explains the difference between the path of the device and the predicted path, as visualized by the green and red dots in figure 4.4. This deviation probably originates from unintentional forces exerted by the human operator, slip-stick behavior of the material supply and an expected load generated by the moving tip.

In conclusion, the tip gears show unrolling-on-a-surface-without-slip behavior when the built structure sufficiently supports the exerted load. This load is induced by friction between the ground, the moving tip and the moving material supply.

Even though prototype I was a successful proof-of-principle, some important lessons needed to be incorporated in a second design. Namely, the most predominant design issue of prototype I was the limited amount of locking positions (1 per 12 degrees) due to discrete shape locking. Consequently, ejected chains needed to be rotated by maximally plus or minus 6 degrees in order to lock, which dramatically affects the measurements. This deviation per joint of maximally 6 degrees is accompanied by a play of 3 degrees and further uncontrolled rotation due to the late timing of the locking plate attachment. More specifically, the locking plates cannot be attached immediately after leaving the tip, resulting in uncontrolled rotation just before locking and consequently path deviation.

Moreover, torque generated by the human operator will always involve other unknown forces acting on the system. However, during a double curvature of 90 degrees, a maximum normal force of 4N was measured, which is low for the intervening human operator. Regarding 32 distortions of at least 0.25N, 75% are labeled to be a direct consequence of the attachment of locking plates (25.0%) and driving the system (50.0%). However, the most interesting distortions occur via the built structure (18.7%), with maximum forces less than 0.36N within this experiment. Even though the input forces are unknown, the outer structure seems to have a damping effect on the distortions.

Finally, the inner and outer chains get

stuck sometimes with respect to one-another by their shape (can hook in each other). As a result, the torque applied at the tip sometimes bends the built structure. A partial solution comprised the exertion of a small tension force ($< 0.6N$) on the material drain, that prevented the inner chains to buckle in the case of reversed growth.

Regarding the secondary design requirements and prototype I, the average load bearing capacity ($48.6N$), the recorded elongation rate (92.9mm/min) and the device's width (w=268mm) fit the design requirements. Therefore, prototype II does not incorporate relevant changes based on these design requirements.

7.1.2 Prototype II

As a result, Prototype II incorporated an electric drive, an automatic locking system, bistable drum brakes instead of shape locks and smoothed chain sides. Consequently, Prototype II showed the reversible unroll principle successfully by showing forward and backwards translation, curvature and a combination of translations and curvatures, with path deviations that fit the design requirements. However, the prototype had difficulties to be operational consistently, which will later be discussed.

Moreover, a reference measurement of prototype II, executed without clamping and activated locking mechanisms, shows the fundamentals of this everting chain driven by torque principle. Namely, when the tip was pulling more input material than it was pushing output material, the tip even moved backwards by 18.3mm. In other words, if input material that is pulled upon, generates sufficient friction to overcome the friction between the tip and the ground plus the friction between the output chain and the ground, the tip pulls itself backwards. At the moment there was more output material than input material, the tip slightly moved forward by 3.1mm.

Load bearing capacity measurements showed that the shape-locked joints of prototype I deformed 4.5 degrees at an exerted load of 54N. In contrast, the friction-locked drum brakes of prototype II rotated by both deformation (22%) and slippage (78%) at a load of 20N. A rotation of 25 degrees was reached at an average load of 7.3N.

It is worth noting that while designing and prototyping, a certain trade-off emerged between load bearing capacity and the power required to lock these chains. Regarding the bistable drum brake, two stable equilibrium points of minimal potential energy occur. An unstable equilibrium point of maximum potential energy can be found between 61 and 68 degrees, in accordance with *The angular movement of locking crank* experiment. Given a certain distance between the brakes and the drum, the thickness and the type of material of the compliant layer determine the stress-strain relations of the material and thereby the heights of these energetic equilibria. Due to the low-torque drive and high-friction cranks the load bearing capacity is lowered by minimizing the layer-thickness of the rubber and by lubricating inside the locking mechanism. Therefore, the load bearing capacity can easily be increased (while keeping in mind the power-to-lock trade-off).

Still, the built structure bears the load induced by the steppers, that pushes against it to move forward. This observation is in line with the maximum force (1.5N*cm/4.67cm = 0.32N exerted tangential to the tip gear) exerted by the steppers in combination with the load-deflection experiments (max. deflection of 5 degrees at 0.32N in perpendicular direction).

Another advantage of bi-stability within the drum brakes, is the fact that no exact rotation is required to change the state (*i.e.* locked or unlocked) of the mechanism. Instead, moving slightly over the tipping point at on average 68 degrees, will be sufficient.

Finally, prototype I and II with a width of 268mm and 270mm respectively, were both able to move around sharp edges at any point of the trajectory. This is the direct consequence of a sliding hinged joint being the Center Of Rotation of the whole tip. One should only take into account that some material will be on the inner side of the COR, by initiating the sharp-edge curvature 20mm (*i.e.* half the width of a chain segment) later.

Everting-chain-based growth-from-the-tip fits a wide variety of application fields due to its maneuverability, accuracy, load bearing capacity and limited interaction with the environment. However, surgical targets will be challenging due

to the large size of these prototypes. Space operations predominantly benefit from maneuverability in zero gravity conditions, while interaction with the environment is not directly required. Moreover, the device can potentially aid search and rescue missions by improved accessibility, however it will probably not be fit to take large objects out.

7.2 Limitations

7.2.1 Limitations of prototype II

Since most limitations of prototype I are tackled in the design of prototype II, only the limitations of prototype II are treated here.

At first, Prototype II did not run reliably since the motors often skip steps. This is the result of the exerted torque and the applied load not being matched sufficiently. Namely, the stepper motors deliver less than 1.5N*cm detent torque each, resulting in a tangential force of less than 1.5N*cm/4.67cm = 0.32N. The low exerted torque is the result of the type of stepper, the absence of a gearbox and a marginal power supply (12V and 1.25A for two steppers).

The effective torque to rotate the crank is even further reduced by the spatial force-to-torque conversion and the presence of friction between the crank and the crank guide. On top of the given loads, the electric drive needs to overcome friction of the moving material supply and tip. Energetically, the load side comprises all moving objects having friction with another surface and kinematic energy, in combination with storage of potential energy in the locking mechanisms. Major friction contributors were the handmade cranks while moving through the tip, due to large height deviations and a redundant amount of glue.

Since the stepper skipped steps (resulting in differential input and output rotations of the gears), accuracy measurements of a predetermined path would not be viable. Therefore, the path generated by the kinematic model is based on the amount of output material and an estimation of the rotations made without deformation and buckling. In other words, accuracy is measured by focusing on the working part of the prototype, resulting in too optimistic results. On the other hand, to make Prototype II fully work, only small fixes that do not considerably affect the working princple are required. Other differences between the kinematic model and the experiment may be due to an inaccurate overlay of the model on the video snapshot and inaccurate measurement of the positional differences.

Moreover, the kinematic model is based on disjunctive rotations and translations. In other words, simultaneous rotation and translation are split-up in separate translations and rotations. Kinematically, this simplification can be relatively accurate, since the Center Of Rotation (COR) can only be an unlocked joint. When the tip also translates, the joint becomes locked while moving through the tip, meaning that a next unlocked joint becomes the new COR. This phenomenon results in predetermined CORs with equal intermediate distances (of 40.5mm). However, since the locking mechanisms deform and slip, the real COR of the tip will be harder to model. On the other hand, if a certain deformation for a certain path is accounted for, the desired trajectory can be recalibrated.

7.2.2 Limitations of measurement setups

A first limitation is the low amount of trials of several experiments, like the translational accuracy measurements of Prototype I and the movement of prototype II with non-activated locking mechanisms. This makes quantified data about time and position marginal. However, the experiments are conducted to get a qualitative sense of what happens, rather than substantiate specific performance criteria. In addition, prototype II did not allow for more accuracy measurements due to extensive slip of the stepper motors.

Secondly, segments of Prototype II were positioned horizontally while the load was applied vertically, involving a loaded wire moving over a rounded edge. Consequently, static friction reduces the effective load exerted on the chain segments. By simplifying this problem to a flat belt moving over a rough curved surface as described by Hibbeler *et al.* [41], the effective load can be measured. The effective force required to move the belt is:

$$F_{load} = F_{eff} * e^{\mu\beta} \tag{16}$$

Adopting a coefficient of friction of $\mu = 0.75$, an angle of belt contact of 90 deg, a F_{load2} of 1.6-17.0N results in an effective force (F_{eff}) of 0.49-5.23N.

Even though this estimated effective load is less than 1/3rd of the inserted load, some locking mechanisms of prototype II still meet the design requirement of 500g (=4.9N), as described by Yan *et al.* [36]. Moreover, the total load bearing capacity of the everting chain principle is double the load bearing capacity of the prototype of Yan *et al.*, by the presence of two chains instead of one. A simplification to future load bearing capacity measurements is to perform them vertically, to reduce the amount of correction factors.

Regarding the *Interaction with environment* experiment, some limitations to the measurement setup arise. Apart from the undesired interventions of the human operator, as stated earlier, the deforming hollow tubes are designed for a load of 0-50N, while the actual maximum load was 4N. Consequently, the deformation of the force transducers was not observed accurately by camera. Moreover, the calibrated strain gauges probably are not accurate under loads of 0.1N. Therefore, only peak forces of 0.25N were analyzed. Furthermore, measuring the power to lock in combination with estimations of friction coefficients will give a more accurate view on the force-field during motion. In conclusion, it would have been easier to express interaction with the environment in terms of the amount of surfaces that move with respect to the environment. Another option would be tracking movement through constrained environments, like sticky fly paper, nails or glue, as described by Hawkes *et al.* [16].

The extension ratio's of prototype I and II were 2.6 and 0.9 respectively. Limiting factors to this extension ratio predominantly were the amount of available chains, which can easily be elevated. For prototype I, the material supply gets stuck with the outer structure as multiple curves in series are made. Even though this phenomenon is not observed at prototype II, the material supply can eventually get stuck by having to much friction with the outer structure.

Finally, it should be noted that the elongation rates of both prototypes are not yet optimized. The main limiting factor for the elongation rate of Prototype I was the attachment of locking plates by the human operator. Prototype II would realize higher elongation rates if the drive would not involve slip-stick behavior.

7.3 Recommendations

7.3.1 Improvements of prototype II

First, the tuning of the delivered power of the motors to the motor load should be improved. The most easy adaptation is an elevated power supply from 7.5W (= 0.625A*12V) to 18W (=1.5A*12V) per stepper motor. Moreover, several NEMA 17 gearboxes are available with reduction ratios up to 46 with a power efficiency of 83%, resulting in a potential detent torque of $1.5 * 46 * 0.83 = 57N * cm$.

Regarding the motor load, 3D printed locking cranks will require no glue and have more accurate dimensions, resulting in less friction while moving through the tip.

Apart from the performance of the system's drive, prototype II can be down-sized in multiple ways. At first, the type of joints, the joint-to-joint distance and the type of locking mechanisms predominantly determine the overall width of the device. A reduction in size of a chains' width has large influence on the overall width, due to the presence of 4 parallel chains.

Regarding the tip gears, the circumference is designed to be exactly the length of 7 joint-to-joint distances. Both this number and the joint-to-joint distances can be reduced. For example, a drum brake can be cut in half and being oriented vertically, which would reduce overall chain width by 50%. To reduce parts within the drum brake, an elastic band around the brakes could function both as a high-friction material and inwards spring.

Moreover, the everting chains can have a certain overlay, instead of being positioned next to each other. On top of that, given that sufficient power will be delivered, only one electric drive should be necessary.

Finally, the reference measurement without clamping and activated locking mechanisms could have resulted in successful growth-from-the-tip, when the chains were clamped and the

unlocked chains piled up in a zig-zag manner. Namely, the chain segments being positioned in their maximum rotated configuration, they can support the tip as well. This redundancy of locking mechanisms would significantly simplify the designs.

7.3.2 Self-supporting planar movement

Firstly, planar movement based on everting chains requires joints with 1 DOF perpendicular to the planar movement and 0 DOF in locked and unlocked configuration, respectively. Regarding the gravity-related load exerted on a sliding hinged joint, as indicated by red arrows in Figure 7.1, a vertical clamp force will prevent vertical translation and a vertical pressure (indicated in blue) over a certain width, reduces bending moments on the axes. This classical chain problem is often solved with rivets or bolts and nuts.

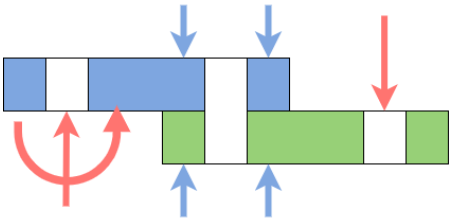

Figure 7.1: **Schematic representation of male and female segment connected by an axis (white box) and loaded by clamping and gravity related forces and moments (red arrows)**

Another recommendation would be variable chain material, axes thicknesses and chain size as the tip moves forward. More specifically, the segments closest to the clamping need to bear the highest forces and moments, due to increasing weight of the chain and distance of the tip, as the tip moves forward. Therefore, the first chain segments can have improved material properties, increased size and weight with respect to the subsequent segments, as visualized in Figure 7.2.

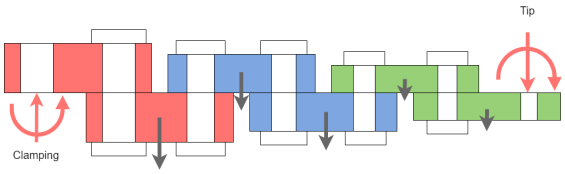

Figure 7.2: **Schematic representation of multiple chain segments in series, with differential material properties (different colors) and variable size.**

The variable dimensions of chains do not have to be a problem for the tip gear when the chains are grabbed on the same height.

7.3.3 3D movements

While the current prototype makes planar movement, the next generation can make 3D curves by relatively small adaptations.

To start, the chain should again be designed with some basic rules:

- Joint should be able to withstand tension
- Joint should friction lock in a robust manner
- Chain needs to be grasped by a gear at the tip
- Chain should be constructed of a low amount of (moving) parts

As a result, a ball socket joint is proposed, incorporated with a compliant and high-friction sheet that deforms under pressure, as indicated in green in figure 7.3. The sheets deforms until they fully touch the socket, resulting in a locked joints. The sheet should be compliant in diverging direction and stiff in circumferential direction in order to lock sufficiently.

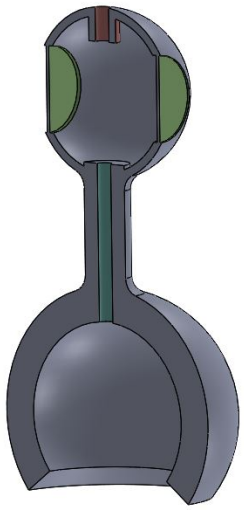

Figure 7.3: **Intersected view of a single chain segment based on ball-socket joints. The joints are locked by outwards deformation of the compliant sheet (green). Once fully deformed, the pressure relieve valve (red) and a connecting tube (blue) let through the pressurized air flow to the next segment.**

Once the sheets are maximally deformed at a certain pressure, the pressure relieve valve (red) and the hollow tube (blue) passively let through air to the next joint, as shown in figure 7.4. This would only work when the deformable sheet is designed in such a way, that it makes the joint air-tight in locked configuration.

Then, a simple (de-)activation system should be designed for the pressure relieve valves. Namely, the joints should (un)lock when the outer chain leaves or enters the tip. This could be a simple mechanical switch that seals the hollow tubes, or pressure relieve valves that are tuned to higher release pressures.

Interestingly, the power-to-lock is generated at the base resulting in more simplified chain segments and larger locking pressures. On top of that, since the internal pressure can be regulated, the friction generated by this lock is also controllable. As a result, the material supply can also lock softly to reduce deviation caused by gravity.

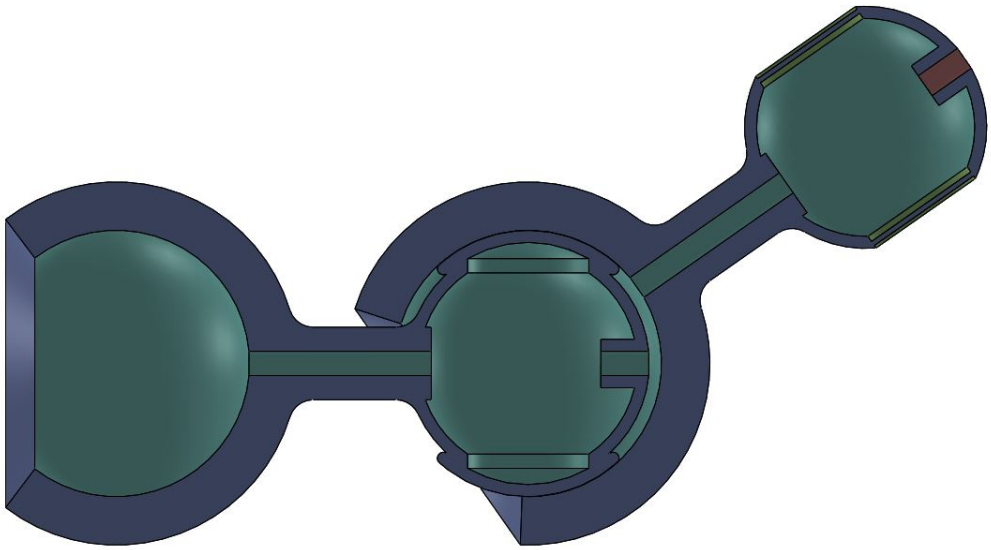

Figure 7.4: **Intersected view of two sequential segments. At the left ball, the compliant sheet (green) is deformed, resulting in an airflow (light blue) to the next ball, originating from the base. There, the pressure is not yet sufficient to deform the sheets and to open the pressure relieve valve.**

A rough design of 3 everting chains is shown in figure 7.5. It should be noted that one, two or more everting chains would also work. However, lowering the amount of chains would affect interaction with the environment (due to moving chains) and load bearing capacity. On the other

hand, increasing the amount of chains would increase complexity, size and control effort of the system.

The tip gears contain hollowed out bulbs and a small central circumference that can grab the ball-socket joints. To further reduce size, it may be possible to create a tip structure that acts as a stator and the gears that act as rotors, together forming three electric motors.

It is worth noting that many details are left-out in this design. For example, a system that (de-)activates the pressure relieve valves are not shown. Moreover, these partly-hinged ball socket joints have 3DOFs but limited rotational range due to shape. In addition, the chain segments will probably hook into each other due to their shape. This problem can be solved by creating male and female segments, instead of one segment with a male and female side. Subsequently, the female (sockets) segments can be flattened without affecting the rotational range. On top of that, assembly of a partly hinged ball-socket joint is challenging. One leak-free solution would be complaint balls and sockets that can be pushed in place.

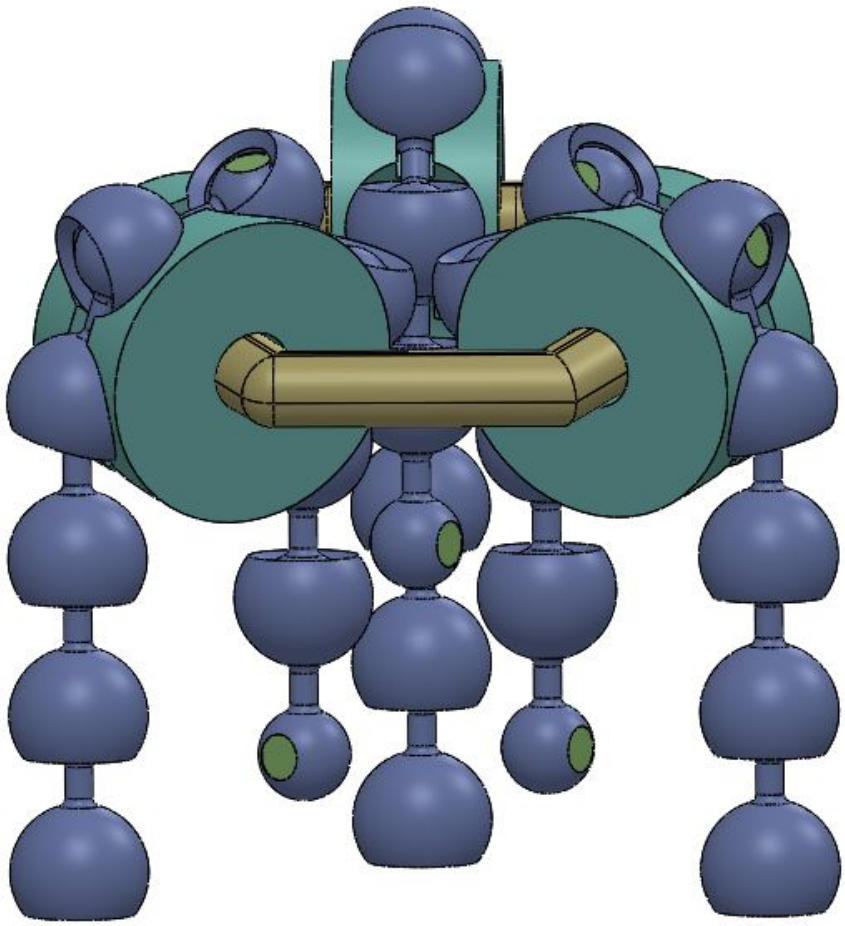

Figure 7.5: **Rough everting chains design able to make 3D movements, with deformable sheets (green), ball socket joints (purple), tip gears (blue) and tip structure (yellow).**

8 Conclusion

This explorative work is aimed to design and prototype a reversible growth-from-the-tip device able to make multiple active curves in series at any point of the trajectory. An innovative principle, based on everting chains, is worked out and prototyped twice in an iterative design loop. Both prototypes successfully performed growth-from-the-tip predominantly in line with a kinematic model, that assumes zero deformation and deflection. Accordingly, the tip gears showed rolling-out behavior with high accuracy along the path.

Growth-from-the-tip in general enables access to small, constrained, and any other hard-to-reach location. A fundamental advantage of both designs is the relatively high load bearing capacity of the support structure, which results in more accurate and fully self-supporting movements along a complex trajectory. On top of that, this chain-based device can (actively) turn around sharp edges. Moreover, the everting principle has the key advantage of having little interaction with the environment, due to self-support and the low amount of moving surfaces with respect to the environment. Finally, relatively high elongation rates and large extension ratios can theoretically be achieved. The everting chain principle is shortly extrapolated to a 3D design, based on ball-socket joints that are inflated from the base in order to lock.

Potential applications are related to gaining access to any hard-to-reach location, consisting of tiny spaces, long, sensitive, high-friction and deforming trajectories with multiple curves in series. Examples are earthquake-related save and rescue missions, access to the Fukushima reactor, surgical targets, complex tube networks, mining, digging, building tunnels or (space) operations with zero gravity.

Still, the explorative nature of this work involves many challenges that need to be tackled in future work, like designing a device that makes 3D curvatures, making the device self-supportive in a 3D space and radically down-sizing the device, if applied to surgery.

Acknowledgements

This work could not have been completed without the help of others. First, I would like to thank Aimée Sakes, since we had a very constructive and educational collaboration. She did not only plow through my internship report of 131 pages, she also guided me towards proper scientific work and she also inspired me by asking very accurate and critical questions. Furthermore, Fabian Trauzettel helped me the last months of my thesis, with very much enthusiasm, effort and good ideas. Moreover, the meetings with Paul Breedveld directed me to the core of what I was doing, even though that meant that interrupting was one of the core things that he was doing. This to-the-point style was very educational for me. I am also grateful to Volkert van der Wijk for participating in the exam committee.

Then, the prototypes were built with the provisions of the TU Delft. Jos van Driel helped me with the measurement setups and the other employees of student workplace really invested to deliver the laser-cut and 3D-printed parts in a short time-frame.

In addition, I would like to thank my parents and my parents in law, who always supported me and gave healthy distraction in these though times. On top of that, my brother gave additional feedback to finalize this work.

Finally, I would like to express my special thanks to Margot, because she supported me closely, very often, in many ways.

References

[1] M. Fackler, "Six years after fukushima, robots finally find reactors' melted uranium fuel," *The New York Times*, 2017.

[2] P. W. Henselmans, G. Smit, and P. Breedveld, "Mechanical follow-the-leader motion of a hyper-redundant surgical instrument: Proof-of-concept prototype and first tests," *Proceedings of the Institution of Mechanical Engineers, Part H: Journal of Engineering in Medicine*, vol. 233, no. 11, pp. 1141–1150, 2019.

[3] J. Rosen, L. N. Sekhar, D. Glozman, M. Miyasaka, J. Dosher, B. Dellon, K. S. Moe, A. Kim, L. J. Kim, T. Lendvay *et al.*, "Roboscope: A flexible and bendable surgical robot for single portal minimally invasive surgery," in *2017 IEEE International Conference on Robotics and Automation (ICRA)*. IEEE, 2017, pp. 2364–2370.

[4] F. Jelínek, R. Pessers, and P. Breedveld, "Dragonflex smart steerable laparoscopic instrument," *Journal of medical devices*, vol. 8, no. 1, 2014.

[5] P. W. Henselmans, S. Gottenbos, G. Smit, and P. Breedveld, "The memo slide: An explorative study into a novel mechanical follow-the-leader mechanism," *Proceedings of the Institution of Mechanical Engineers, Part H: Journal of Engineering in Medicine*, vol. 231, no. 12, pp. 1213–1223, 2017.

[6] G. Gerboni, P. W. Henselmans, E. A. Arkenbout, W. R. van Furth, and P. Breedveld, "Helixflex: bioinspired maneuverable instrument for skull base surgery," *Bioinspiration & biomimetics*, vol. 10, no. 6, p. 066013, 2015.

[7] A. Sakes, A. Ali, J. Janjic, and P. Breedveld, "Novel miniature tip design for enhancing dexterity in minimally invasive surgery," *Journal of Medical Devices*, vol. 12, no. 3, 2018.

[8] A. Arora, Y. Ambe, T. H. Kim, R. Ariizumi, and F. Matsuno, "Development of a maneuverable flexible manipulator for minimally invasive surgery with varied stiffness," *Artificial Life and Robotics*, vol. 19, no. 4, pp. 340–346, 2014.

[9] C. Fan, D. Dodou, and P. Breedveld, "Review of manual control methods for handheld maneuverable instruments," *Minimally Invasive Therapy & Allied Technologies*, vol. 22, no. 3, pp. 127–135, 2013.

[10] V. Vitiello, S.-L. Lee, T. P. Cundy, and G.-Z. Yang, "Emerging robotic platforms for minimally invasive surgery," *IEEE reviews in biomedical engineering*, vol. 6, pp. 111–126, 2012.

[11] H. M. Le, T. N. Do, and S. J. Phee, "A survey on actuators-driven surgical robots," *Sensors and Actuators A: Physical*, vol. 247, pp. 323–354, 2016.

[12] A. Degani, H. Choset, A. Wolf, and M. A. Zenati, "Highly articulated robotic probe for minimally invasive surgery," in *Proceedings 2006 IEEE International Conference on Robotics and Automation, 2006. ICRA 2006.* IEEE, 2006, pp. 4167–4172.

[13] A. Ali, A. Sakes, E. A. Arkenbout, P. Henselmans, R. van Starkenburg, T. Szili-Torok, and P. Breedveld, "Catheter steering in interventional cardiology: Mechanical analysis and novel solution," *Proceedings of the Institution of Mechanical Engineers, Part H: Journal of Engineering in Medicine*, vol. 233, no. 12, pp. 1207–1218, 2019.

[14] T. Ota, A. Degani, D. Schwartzman, B. Zubiate, J. McGarvey, H. Choset, and M. A. Zenati, "A highly articulated robotic surgical system for minimally invasive surgery," *The Annals of thoracic surgery*, vol. 87, no. 4, pp. 1253–1256, 2009.

[15] P. E. Dupont, J. Lock, B. Itkowitz, and E. Butler, "Design and control of concentric-tube robots," *IEEE Transactions on Robotics*, vol. 26, no. 2, pp. 209–225, 2009.

[16] E. W. Hawkes, L. H. Blumenschein, J. D. Greer, and A. M. Okamura, "A soft robot that navigates its environment through growth," *Science Robotics*, vol. 2, no. 8, p. eaan3028, 2017.

[17] M. T. Doelman, "A mechanical overview on growth principles of plant roots underground," *TUDelft, Delft, Netherlands*, May 2020.

[18] E. Del Dottore, A. Mondini, A. Sadeghi, and B. Mazzolai, "A plant-inspired kinematic model for growing robots," in *2018 IEEE International Conference on Soft Robotics (RoboSoft)*. IEEE, 2018, pp. 20–24.

[19] E. Del Dottore, "Characterization of the growing from the tip as robot locomotion strategy. front. robot. ai 6: 45. doi: 10.3389/frobt. 2019.00045 characterization of the growing from the tip as robot locomotion strategy emanuela del dottore*, alessio mondini, ali sadeghi and barbara mazzolai*," *Center for Micro-BioRobotics, Istituto Italiano di Tecnologia, Pontedera, Italy*, 2019.

[20] A. Standard *et al.*, "Standard terminology for additive manufacturing technologies," *ASTM International F2792-12a*, 2012.

[21] K. Oettmeier and E. Hofmann, "Additive manufacturing technology adoption: an empirical analysis of general and supply chain-related determinants," *Journal of Business Economics*, vol. 87, no. 1, pp. 97–124, 2017.

[22] A. Sadeghi, A. Tonazzini, L. Popova, and B. Mazzolai, "A novel growing device inspired by plant root soil penetration behaviors," *PloS one*, vol. 9, no. 2, 2014.

[23] A. Sadeghi, A. Mondini, and B. Mazzolai, "Toward self-growing soft robots inspired by plant roots and based on additive manufacturing technologies," *Soft robotics*, vol. 4, no. 3, pp. 211–223, 2017.

[24] A. Sadeghi, E. Del Dottore, A. Mondini, and B. Mazzolai, "Passive morphological adaptation for obstacle avoidance in a self-growing robot produced by additive manufacturing," *Soft Robotics*, vol. 7, no. 1, pp. 85–94, 2020.

[25] E. Del Dottore, A. Sadeghi, A. Mondini, and B. Mazzolai, "Continuous growth in plant-inspired robots through 3d additive manufacturing," in *2018 IEEE International Conference on Robotics and Automation (ICRA)*. IEEE, 2018, pp. 1–7.

[26] R. P. Kumpf and M. K. Nowack, "The root cap: a short story of life and death," *Journal of experimental botany*, vol. 66, no. 19, pp. 5651–5662, 2015.

[27] D. Lunni, E. Del Dottore, A. Sadeghi, M. Cianchetti, E. Sinibaldi, and B. Mazzolai, "Investigation of tip extrusion as an additive manufacturing strategy for growing robots," in *Conference on Biomimetic and Biohybrid Systems*. Springer, 2018, pp. 288–299.

[28] B. Durakovic, "Design for additive manufacturing: Benefits, trends and challenges," *Periodicals of Engineering and Natural Sciences*, vol. 6, no. 2, pp. 179–191, 2018.

[29] T. D. Ngo, A. Kashani, G. Imbalzano, K. T. Nguyen, and D. Hui, "Additive manufacturing (3d printing): A review of materials, methods, applications and challenges," *Composites Part B: Engineering*, vol. 143, pp. 172–196, 2018.

[30] J. D. Greer, T. K. Morimoto, A. M. Okamura, and E. W. Hawkes, "A soft, steerable continuum robot that grows via tip extension," *Soft robotics*, vol. 6, no. 1, pp. 95–108, 2019.

[31] J. D. Greer, L. H. Blumenschein, A. M. Okamura, and E. W. Hawkes, "Obstacle-aided navigation of a soft growing robot," in *2018 IEEE International Conference on Robotics and Automation (ICRA)*. IEEE, 2018, pp. 1–8.

[32] B. A. Baydere, S. K. Talas, and E. Samur, "A novel highly-extensible 2-dof pneumatic actuator for soft robotic applications," *Sensors and Actuators A: Physical*, vol. 281, pp. 84–94, 2018.

[33] C. Tutcu, B. A. Baydere, S. K. Talas, and E. Samur, "Quasi-static modeling of a novel growing soft-continuum robot," *The International Journal of Robotics Research*, p. 0278364919893438, 2019.

[34] X. Wang, H. Jin, Y. Zhu, B. Chen, D. Bie, Y. Zhang, and J. Zhao, "Serpenoid polygonal rolling for chain-type modular robots: A study of modeling, pattern switching and application," *Robotics and Computer-Integrated Manufacturing*, vol. 39, pp. 56–67, 2016.

[35] D. Bie, I. Sajid, J. Han, J. Zhao, and Y. Zhu, "Natural growth-inspired distributed self-reconfiguration of ubot robots," *Complexity*, vol. 2019, 2019.

[36] T. Yan, S. Teshigawara, and H. H. Asada, "Design of a growing robot inspired by plant growth," in *2019 IEEE/RSJ International Conference on Intelligent Robots and Systems (IROS)*. IEEE, 2019, pp. 8006–8011.

[37] S. Ruiz, D. Or, and S. J. Schymanski, "Soil penetration by earthworms and plant roots—mechanical energetics of bioturbation of compacted soils," *PLoS One*, vol. 10, no. 6, 2015.

[38] P. Breedveld, J. L. Herder, and T. Tomiyama, "Teaching creativity in mechanical design," in *4th World Conference on Design Research (IASDR2011), Delft, The Netherlands, Oct*, 2011.

[39] Z. Zhang, J. Dequidt, J. Back, H. Liu, and C. Duriez, "Motion control of cable-driven continuum catheter robot through contacts," *IEEE Robotics and Automation Letters*, vol. 4, no. 2, pp. 1852–1859, 2019.

[40] F. Jelínek, E. A. Arkenbout, P. W. Henselmans, R. Pessers, and P. Breedveld, "Classification of joints used in steerable instruments for minimally invasive surgery—a review of the state of the art," *Journal of Medical Devices*, vol. 9, no. 1, 2015.

[41] R. Hibbeler, "Engineering mechanics-statics," *Published by Prentice Hall, Singapore, 12th edition, ISBN-13: 978-981-06-8134-0*, 2010.

9 Appendix

A

CPC classification			CPC name	Result number
	A61		Medical or veterinary science; hygiene	
		A61B1/00	Instruments for performing medical examinations of the interior of cavities or tubes of the body by visual or photographical inspection, e.g. endoscopes	5
B21-B33			Shaping	
	B05		Spraying or atomising in general; applying liquids or other fluent materials to surfaces, in general	1
	B22		Casting; powder metallurgy	2
	B23		Machine tools; Metal-working not otherwise provided for	2
	B25J		Hand tools; portable power-driven tools; manipulators	4,5,8,9
	B29		Working of plastics; working of substances in a plastic state in general	1,6
	B33		Additive manufacturing technology	
		B33Y10/00	Processes of additive manufacturing	1
		B33Y30/00	Apparatus for additive manufacturing; Details thereof or accessories therefor	1,2,6,7
B60-B68			Transporting	
	B62		Land vehicles for travelling otherwise than on rails	
		B62D57/000	Vehicles characterized by having other propulsion or other ground- engaging means than wheels or endless track, alone or in addition to wheels or endless track	3,5
	B64		Aircraft; aviation; cosmonautics	
		B64G1/00	Cosmonautic vehicles	2
		F15B15/00	Fluid-actuated devices for displacing a member from one position to another; Gearing associated therewith	3

Figure 9.1: **CPC categorization of patent search results on Espacenet, regarding growing robots through the addition of material at the tip, with result numbers: 1) US2016031155A1, 2) CN107921564A, 3) US2019217908A1, 4) CN110450149A, 5) WO2020060858A1, 6) CN106564189A, 7) CN107984758A, 8) CN110861078 and 9) CN110450138.**

B

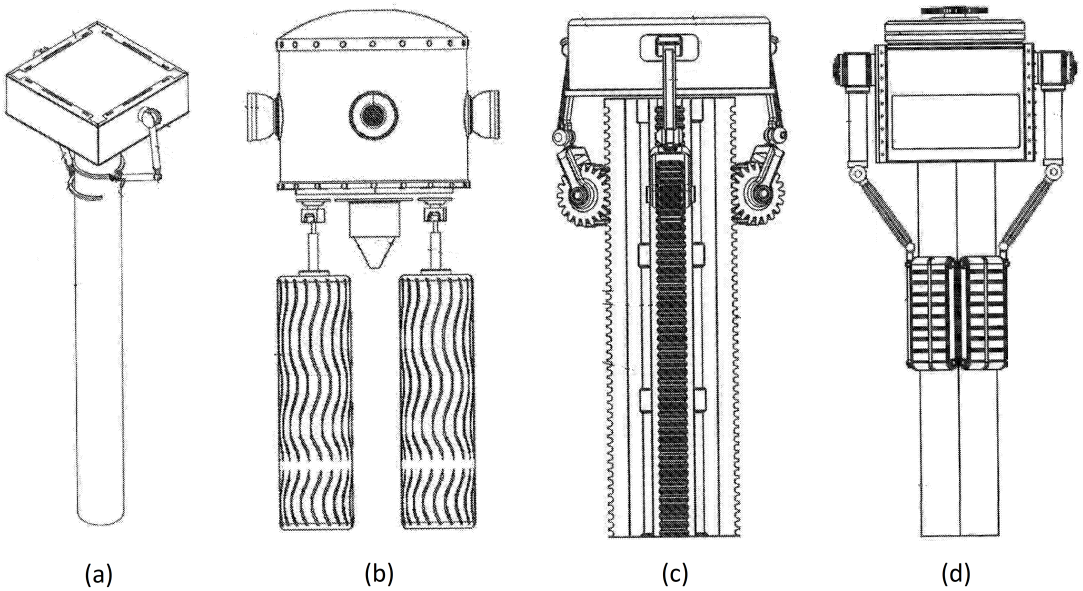

Figure 9.2: **Patent result 2 - Multiple techniques for in-space manufacturing with growing technique through additive manufacturing, with (a) annular tube clamp, (b) rectangular clamp with rollers, (c) gearing and (d) rectengular grippers. Espacenet CPC categories: B22, B23K, B33Y and B64G1 (Figure adapted from patent CN107921564A)**

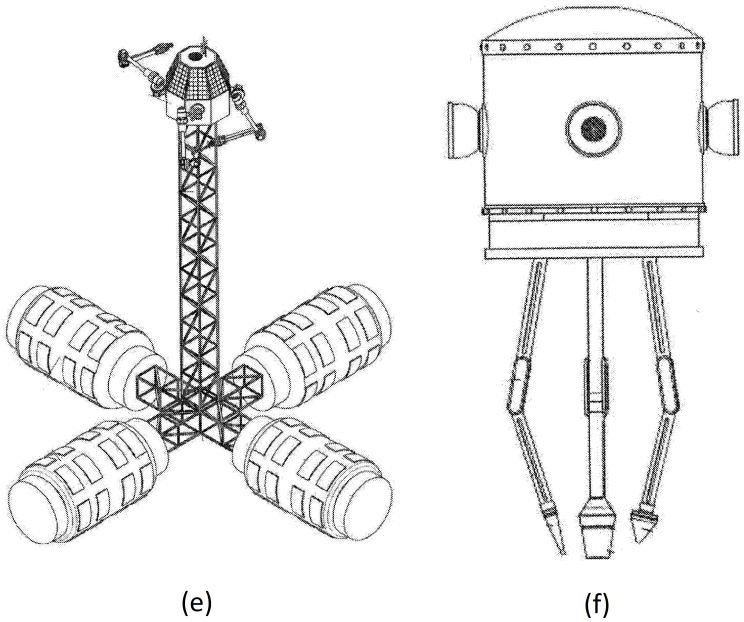

Figure 9.3: **Patent result 2 - Multiple techniques for in-space manufacturing with growing technique through additive manufacturing, with (e) grippers to any type of structure and (f) multi-functional tools. Espacenet CPC categories: B22, B23K, B33Y and B64G1 (Figure adapted from patent CN107921564A)**

C

Segment selection

		Cables						
		Rolling		Sliding		Sliding Rolling		Bending
		FF-MM	FM-FM	FF-MM	FM-FM	FF-MM	FM-FM	One part
		A	B	C	D	E	F	G
	Weight							
Feasibility for everting growth process	4	3	3	4	4	1	1	3
Simplicity of the design	3	3	3	3	3	2	2	5
Manufacturability	3	3	3	3	3	3	3	1
Estimated load bearing capacity	1	2	2	3	3	2	2	2
Ability to be downscaled	1	3	3	3	3	1	1	5
	Total:	**35**	**35**	**40**	**40**	**22**	**22**	**37**

		Shape						
		Rolling		Sliding		Sliding Rolling		Bending
		FF-MM	FM-FM	FF-MM	FM-FM	FF-MM	FM-FM	One part
		H	I	J	K	L	M	N
	Weight							
Feasibility for everting growth process	4	3	3	5	5	3	1	2
Simplicity of the design	3	3	3	5	5	1	1	5
Manufacturability	3	2	3	5	5	2	4	1
Estimated load bearing capacity	1	1	1	5	5	1	1	2
Ability to be downscaled	1	2	2	4	4	1	1	5
	Total:	**30**	**33**	**59**	**59**	**23**	**21**	**33**

Figure 9.4: **Segment selection with criteria and weight factors**

D

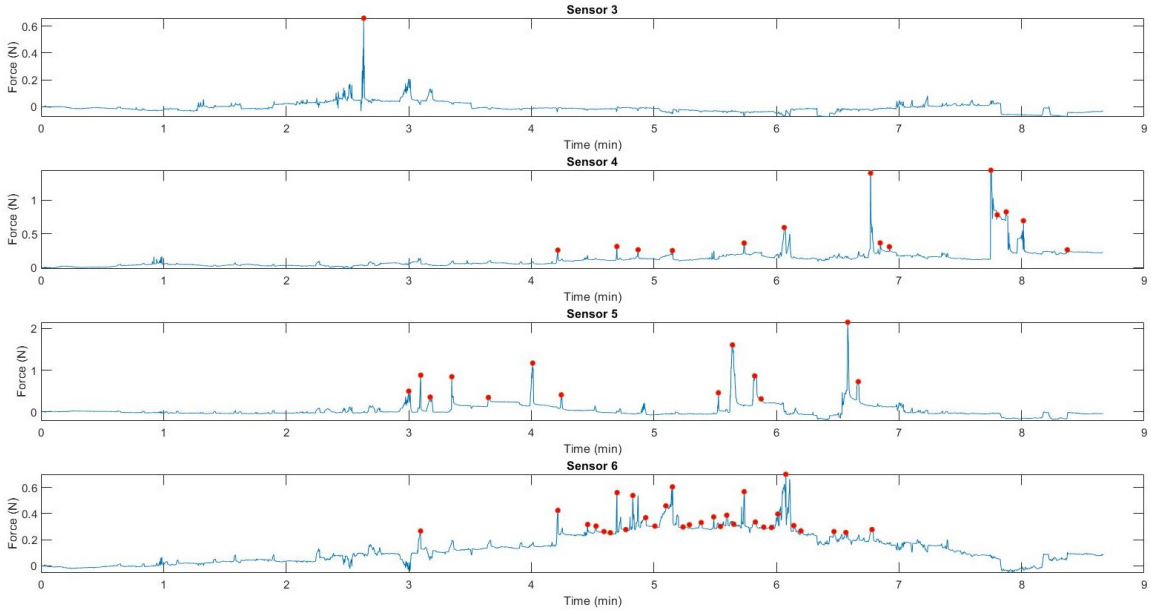

Figure 9.5: **Normal-force measurements over time of 4 sensors in Experiment 6 (out of 7). Sensor 3 to 6 correspond to the numbering at Figure 4.7. The red dots are aimed to represent relevant contact with the device, found by a *findpeaks* function in MATLAB with Minimal Peak Height of 0.25 N and a Mininmal Peak Distance of 3 seconds.**

E

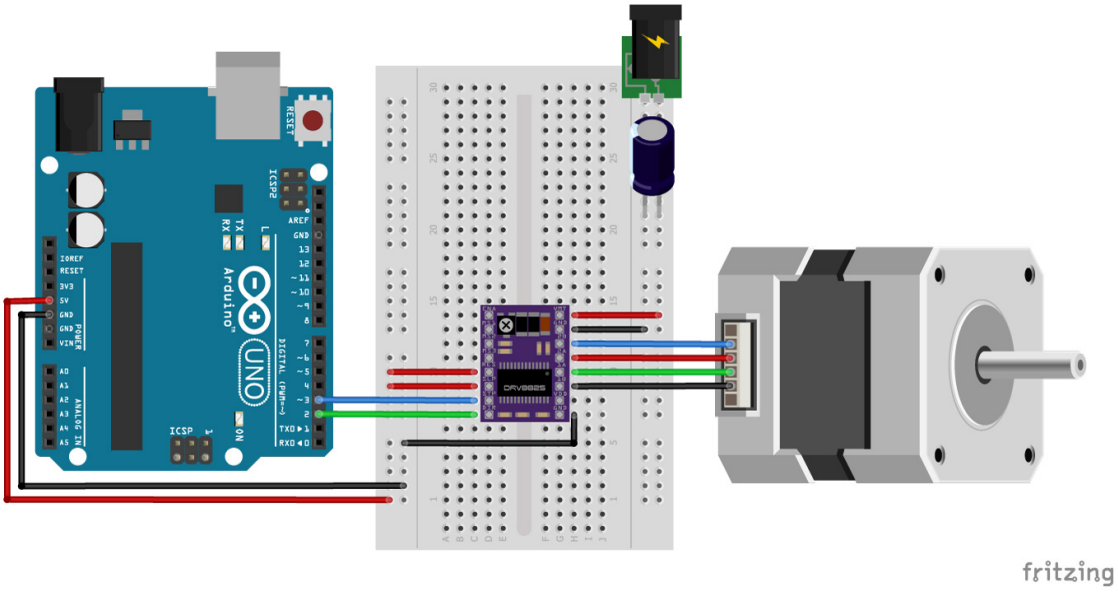

Figure 9.6: **Electronic (single) setup using a Arduino Uno Rev 3 development board, two DRV8825 stepper drivers, two NEMA 17 (1.8** deg **2-phase of double length (40mm) and 1.5A input) stepper motors, two 100μF capacitors and a adapter with an output of 12V and 1.25A (direct current).**

https://www.makerguides.com/drv8825-stepper-motor-driver-arduino-tutorial/

F

Mechanism Number	Min. Start Angle (degrees)	Max. Start Angle (degrees)	Play (degrees)	Average Start (degrees)	Peak Potential Energy (degrees)	Peak Potential Energy minus Start (degrees)	Min. Locked Angle (degrees)	Max. Locked Angle (degrees)	Play (degrees)	Average Lock (degrees)	Average Rotation (degrees)
1	-2	4	6	1	68	67	96	100	4	98	97
2	-1	7	8	3	64	61	90	98	8	94	91
3	-2	6	8	2	68	66	90	100	10	95	93
4	-2	2	4	0	61	61	84	92	8	88	88
5	-3	4	7	0.5	68	67.5	90	96	6	93	92.5
6	-1	6	7	2.5	68	65.5	91	99	8	95	92.5
7	-4	4	8	0	67	67	91	98	7	94.5	94.5
8	-2	3	5	0.5	66	65.5	86	94	8	90	89.5
9	-3	3	6	0	65	65	89	92	3	90.5	90.5
10	-2	4	6	1	66	65	90	97	7	93.5	92.5
11	-2	6	8	2	70	68	89	94	5	91.5	89.5
12	-2	5	7	1.5	66	64.5	88	96	8	92	90.5
13	-1	6	7	2.5	69	66.5	92	98	6	95	92.5
14	-2	3	5	0.5	68	67.5	90	93	3	91.5	91
15	-3	7	10	2	70	68	90	96	6	93	91
Average	-2.133	4.667	**6.800**	**1.267**	**66.933**	**65.667**	89.733	96.200	**6.467**	**92.967**	**91.700**

Table 6: **Angular measurements of crank attached to locking mechanism**

G

MATLAB script 1 - Load-deformation relation

% Load-deflection calculations

% Made by Michiel Doelman

% 27-07-2020

clear all clc

%% Parameters $l_1 = 0.04; \%[m]$

$l_2 = 0.06; \%[m]$

F = 0.1:0.1:50; %[N]

%% Youngs' Modulus

$E_P MMA = 2.9 * 10^9;$

$E_T eflon = 0.5 * 10^9;$

$E_P VC = 3.25 * 10^9; \%2.4 - 4.1$

$E_A BS = 2.25 * 10^9; \%1.4 - 3.1$

% Solid Rod

$R_r od = 0.005; \%[m]$

% hollow Rod

$R_r od_1 = 0.0025;$

$R_r od_2 = 0.0035;$

% Solid BEAM

b = 0.02; %[m] (rekstrookje minstens 0.004m)

h = 0.006; %[m]

%% Area moment of inertia of cross section

$I_r od = pi/4 * R_r od^4;$

$I_h ollow_r od = pi * ((2 * R_r od_2)^4 - (2 * R_r od_1)^4)/64;$

$I_B eam = (1/12) * b * h^3;$

%% Calculations hollow rod

$theta_{2T}2 = F * (l_1)^(2)/(2 * E_T eflon * I_h ollow_r od);$

$theta_{2P}2 = F * (l_1)^(2)/(2 * E_P MMA * I_h ollow_r od);$

$theta_{2P}VC2 = F * (l_1)^(2)/(2 * E_P VC * I_h ollow_r od);$

$w_{2T}2 = F * (l_1)^(3)/(3 * E_T eflon * I_h ollow_r od);$

$w_{2P}2 = F * (l_1)^(3)/(3 * E_P MMA * I_h ollow_r od);$

$w_{2P}VC2 = F * (l_1)^(3)/(3 * E_P VC * I_h ollow_r od);$

$w_{3T}2 = w_{2T}2 + l_2 * tan(theta_{2T}2);$

$w_{3P}2 = w_{2P}2 + l_2 * tan(theta_{2P}2);$

$w_{3P}VC2 = w_{2P}VC2 + l_2 * tan(theta_{2P}VC2);$

%% Figures

figure plot(F,$w_{3P}2$)

hold on

plot(F,$w_{3P}VC2$)

xlabel('Force (N)')

ylabel('Deflection (m)')

title('Linear load-deflection relationship of a hollow rod')

legend('PMMA hollow','PVC hollow','Location','northwest')

H

MATLAB script 2 - Kinematic model of growth-from-the-tip device

% Made by Michiel Doelman from TU Delft

clc

clear all

D = 268; %mm – Prototype I = 268mm — Prototype II = 270mm

l = 42; %mm – Prototype I = 42mm — Prototype II = 40.5mm

w = 40; %mm

$R_gear = 48.4; \%mm - -Prototype I = 48.40mm - - - Prototype II = 46.67mm$

x = 360/7; %Rotation of 1 chain segment

%Cumulative input angles

% Double curvature prototype I

$alpha_L = [0, x, 2*x, 2*x, 2*x, 2*x, 2*x, 2*x, 2*x, 2*x, 2*x, 3*x, 4*x, 5*x, 6*x, 7*x, 8*x, 9*x, 10*x, 11*x].*2*pi/360;$

$alpha_R = [0, x, 2*x, 3*x, 4*x, 5*x, 6*x, 7*x, 8*x, 9*x, 10*x, 11*x, 11*x, 11*x, 11*x, 11*x, 11*x, 11*x, 11*x, 11*x].*2*pi/360;$

% Double curvature

$\%alpha_L = [0, x, x, x, x, x, x, 2*x, 3*x, 4*x, 5*x, 6*x].*2*pi/360;$

$\%alpha_R = [0, x, 2*x, 3*x, 4*x, 5*x, 6*x, 6*x, 6*x, 6*x, 6*x, 6*x, 6*x].*2*pi/360;$

% Video straight movement

$\% alpha_L = [0, x, x, 2*x, 2*x, 2*x, 3*x, 3*x].*2*pi/360;$

$\% alpha_R = [0, 0, x, 2*x, 3*x, 4*x, 5*x, 6*x].*2*pi/360;$

% Video single curve

$\% alpha_L = [0, 0, 0, 0, 0].*2*pi/360;$

$\% alpha_R = [0, x, 2*x, 3*x, 4*x].*2*pi/360;$

$T_L = R_gear * alpha_L;$

$T_R = R_gear * alpha_R;$

$d_{TL} = diff(T_L);$

$d_{TR} = diff(T_R);$

$dl = T_L - T_R;$

$ddl = round(d_{TL} - d_{TR});$

$b_c = 2 * atan(l./(2*(D-w))); \%Constantangle$

$beta = (alpha_L - alpha_R).*360/(2*pi*x) * b_c;$

%beta = 2*atan(dl./(2*(D-w)));

R = zeros(11,2);

```
L = zeros(11,2);
R(1,:) = [(D-w),0];
L(1,:) = [0,0];
for i = 1:(length(dl)-1)
if ddl(i) ¿ 0 % Turn right
L(i+1,:) = R(i,:) + [-(D-w)*cos(beta(i+1)),(D-w)*sin(beta(i+1))];
R(i+1,:) = R(i,:); end
if ddl(i) ¡ 0 % Turn left
R(i+1,:) = L(i,:) + [(D-w)*cos(beta(i+1)),-(D-w)*sin(beta(i+1))];
L(i+1,:) = L(i,:); end
if ddl(i) == 0 % Straight movement
R(i+1,:) = R(i,:) + [l*sin(beta(i+1)),l*cos(beta(i+1))];
L(i+1,:) = L(i,:) + [l*sin(beta(i+1)),l*cos(beta(i+1))]; end
end
figure
plot(R(:,1),R(:,2),'o', 'MarkerSize', 12,'MarkerFaceColor', 'g')
hold on
plot(L(:,1),L(:,2),'o', 'MarkerSize', 12,'MarkerFaceColor', 'g')
axis([-275 250 -100 425])
axis square
%title('Positions of chain axis at forward and cuved movement')
xlabel('X position (mm)')
ylabel('Y position (mm)')
```

I

MATLAB script 3 - Processing of interaction with environment experiment

clear all clc

T = (table2array(readtable('Experiment$_6$.$xlsx$',' $Range$',' $A1:A5200$'))./60000;

S3 = table2array(readtable('Experiment$_6$.$xlsx$',' $Range$',' $J1:J5200$'));

S4 = table2array(readtable('Experiment$_6$.$xlsx$',' $Range$',' $K1:K5200$'));

S5 = table2array(readtable('Experiment$_6$.$xlsx$',' $Range$',' $N1:N5200$'));

S6 = table2array(readtable('Experiment$_6$.$xlsx$',' $Range$',' $O1:O5200$'));

% Offset

$S3_I = S3 - mean(S3(1:20))$;

$S4_I = S4 - mean(S4(1:20))$;

$S5_I = S5 - mean(S5(1:20))$;

$S6_I = S6 - mean(S6(1:20))$;

% Find peaks

[PKS3,LOCS3,W3,S3H] = findpeaks($S3_I$,' $MinPeakHeight$', 0.25,' $MinPeakDistance$', 30);

[PKS4,LOCS4,W4,S4H] = findpeaks($S4_I$,' $MinPeakHeight$', 0.25,' $MinPeakDistance$', 30);

[PKS5,LOCS5,W5,S5H] = findpeaks($S5_I$,' $MinPeakHeight$', 0.25,' $MinPeakDistance$', 30);

[PKS6,LOCS6,W6,S6H] = findpeaks($S6_I$,' $MinPeakHeight$', 0.25,' $MinPeakDistance$', 30);

subplot(4,1,1)

plot(T,$S3_I$)

hold on

plot(LOCS3./600,PKS3,'o', 'MarkerSize', 4,'MarkerFaceColor', 'r')

title('Sensor 3')

xlabel('Time (min)')

ylabel('Force (N)')

subplot(4,1,2)

plot(T,$S4_I$)

hold on

plot(LOCS4./600,PKS4,'o', 'MarkerSize', 4,'MarkerFaceColor', 'r')

title('Sensor 4')

xlabel('Time (min)')

ylabel('Force (N)')

subplot(4,1,3)

plot(T,$S5_I$)

hold on

plot(LOCS5./600,PKS5,'o', 'MarkerSize', 4,'MarkerFaceColor', 'r')

title('Sensor 5')

xlabel('Time (min)')

ylabel('Force (N)')

subplot(4,1,4)

plot(T,S6$_I$)

hold on

plot(LOCS6./600,PKS6,'o', 'MarkerSize', 4,'MarkerFaceColor', 'r')

title('Sensor 6')

xlabel('Time (min)')

ylabel('Force (N)')

J

MATLAB script 4 - Crank locations tip

```
gamma = +1*2*pi*1/21;
alpha = 2*pi/(7*2) - gamma;
alpha2 = alpha + 2*pi/(7) ;
alpha3 = alpha + 4*pi/(7) ;
alpha4 = alpha + 6*pi/(7) ;
beta0 = alpha2 + 0.5*pi;
beta1 = alpha3 + 0.5*pi;
beta2 = alpha4 + 0.5*pi;
x1 = -46.67*cos(gamma) + 0;
x2 = 40.5*sin(alpha) + x1;
x3 = 40.5*sin(alpha2) + x2;
x4 = 40.5*sin(alpha3) + x3;
x5 = 40.5*sin(alpha4) + x4;
x6 = x5;
y1 = -46.67*sin(gamma) + 0;
y2 = 40.5*cos(alpha) + y1;
y3 = 40.5*cos(alpha2) + y2;
y4 = 40.5*cos(alpha3) + y3;
y5 = 40.5*cos(alpha4) + y4;
y6 = y5 -40.5;
x = [x1,x1,x2,x3,x4,x5,x6];
y = [y1-60;y1;y2;y3;y4;y5;y6];
x00 = x1;
x11 = x1 + 0;
x22 = 18*sin(alpha)+ x2;
x33 = 18*sin(alpha2)+ x3;
x44 = 18*sin(alpha3)+ x4;
x55 = 18*sin(alpha4)+ x5;
x66 = x6;
y00 = y1 -40.5 + 18;
y11 = y1 + 18;
y22 = 18*cos(alpha) + y2;
```

```
y33 = 18*cos(alpha2) + y3;
y44 = 18*cos(alpha3) + y4;
y55 = 18*cos(alpha4) + y5;
y66 = y6 - 18;
X = [x00,x11,x22,x33,x44,x55,x66];
Y = [y00;y11;y22;y33;y44;y55;y66];
x000 = x1;
x111 = x1;
x222 = 18*sin(alpha) + x1;
x333 = 18*sin(alpha2) + x2;
x444 = 18*sin(alpha3) + x3;
x555 = 18*sin(alpha4) + x4;
x666 = x5;
x777 = x6;
y000 = y1 - 40.5 + 18;
y111 = y1;
y222 = 18*cos(alpha) + y1;
y333 = 18*cos(alpha2) + y2;
y444 = 18*cos(alpha3) + y3;
y555 = 18*cos(alpha4) + y4;
y666 = y5 - 18;
y777 = y6 - 18;
X111 = [x000,x222,x333,x444,x555,x666,x777];
Y111 = [y000;y222;y333;y444;y555;y666;y777];
xl33 = 18*sin(beta0) + x3;
yl33 = 18*cos(beta0) + y3;
xl44 = 18*sin(beta1) + x4;
yl44 = 18*cos(beta1) + y4;
xl55 = 18*sin(beta2) + x5;
yl55 = 18*cos(beta2) + y5;
xl66 = -18 + x6;
yl66 = y6;
x3333 = 18*sin(alpha2 + 0.5*pi) + x2;
x4444 = 18*sin(alpha3 + 0.5*pi) + x3;
```

```
x5555 = 18*sin(alpha4 + 0.5*pi) + x4;
x6666 = x5 - 18;
x7777 = x6 -18;
y3333 = 18*cos(alpha2 + 0.5*pi) + y2;
y4444 = 18*cos(alpha3 + 0.5*pi) + y3;
y5555 = 18*cos(alpha4 + 0.5*pi) + y4;
y6666 = y5;
y7777 = y6;
Xl = [xl33,xl44,xl55,xl66];
X1111 = [x4444,x5555,x6666,x7777];
Yl = [yl33;yl44;yl55;yl66];
Y1111 = [y4444;y5555;y6666;y7777];
cplot = @(r,x0,y0) plot(x0 + r*cos(linspace(0,2*pi)),y0 + r*sin(linspace(0,2*pi)),'-'); cplot(43.17,0,0)
hold on
cplot(3.5,0,0)
cplot(51,0,0)
cplot(3.5,x1,y1)
cplot(3.5,x2,y2)
cplot(3.5,x3,y3)
cplot(3.5,x4,y4)
cplot(3.5,x5,y5)
cplot(3.5,x6,y6)
cplot(3.5,x1,y1-40.5)
plot(x,y,'r')
plot(X,Y,'o', 'MarkerSize', 12,'MarkerFaceColor', 'g')
plot(X111,Y111,'o', 'MarkerSize', 9,'MarkerFaceColor', 'y')
plot(Xl,Yl,'o', 'MarkerSize', 12,'MarkerFaceColor', 'r')
plot(X1111,Y1111,'o', 'MarkerSize', 9,'MarkerFaceColor', 'm')
axis equal
title('Spatial overview of chain movement through tip')
xlabel('X coördinates (mm)')
ylabel('Y coördinates (mm)')
```

K

MATLAB script 5 - Load bearing plots

```
clc clear all

Load = [0 100 200 300 400 600 800 1050 1300 1550 2050 0];

F_load = Load./1000 * 9.81;

alpha = [0;10;13;18;12;25;10;11;11;13];

alpha_2 = alpha./360 * 2 * pi;

beta = [0 2 3 4 6 8 14 16 18 20 27 18;

0 5 8 10 11 13 14 17 38 44 55 47;

0 1 2 4 43 50 55 56 57 57 58 58;

0 4 7 9 27 46 48 57 59 60 61 60;

0 1 2 3 5 8 12 14 16 23 27 22;

0 5 9 12 15 19 21 26 29 36 41 14;

0 15 18 50 51 59 61 64 65 67 69 65;

0 7 9 11 14 18 25 32 36 43 47 34;

0 1 4 8 11 14 20 26 29 32 38 30;

0 2 4 9 12 18 21 23 25 29 38 27];

beta_2 = beta./360 * 2 * pi;

a_b = zeros(10, 12);

for i = 1:10

a_b(i, :) = [alpha_2(i)alpha_2(i)alpha_2(i)alpha_2(i)alpha_2(i)alpha_2(i)alpha_2(i)alpha_2(i)alpha_2(i)alpha_2(i)alpha_2(i)alpha_2(i)
beta_2(i, :);

end

F_eff = F_load. * cos(a_b);

Sx = 25*ones(100,1);

Sy = linspace(0,20,100);

figure

plot(beta(1,:),F_eff(1, :))

hold on

plot(beta(2,:),F_eff(2, :))

plot(beta(3,:),F_eff(3, :))

plot(beta(4,:),F_eff(4, :))

plot(beta(5,:),F_eff(5, :))

plot(beta(6,:),F_eff(6, :))
```

plot(beta(7,:),F$_eff(7,:))

plot(beta(8,:),F$_eff(8,:))

plot(beta(9,:),F$_eff(9,:))

plot(beta(10,:),F$_eff(10,:))

plot(Sx,Sy)

ylabel('F$_{eff}(N)'$)

xlabel('beta (degrees)')

legend('Mech. 1','Mech. 2','Mech. 3','Mech. 4','Mech. 5','Mech. 6','Mech. 7','Mech. 8','Mech. 9','Mech. 10')

Read$_off$ = [1.62.42.83.36.36.47.98.910.014.017.0];

Mean$_max_F$ = $mean(Read_off)$;

dbeta = beta(:,11) - beta(:,12);

pElastic = dbeta./beta(:,11)*100;

pSlip = mean(100 - pElastic);